Femtosecond laser microfabricated devices for biophotonic applications

Debaditya Choudhury

A thesis submitted for the degree of

Doctor of Philosophy

Heriot-Watt University

Institute of Biological Chemistry, Biophysics and Bioengineering

May 2013

Abstract

Femtosecond Laser Direct Writing has emerged as a key enabling technology for realising miniaturised biophotonic applications offering clear advantages over competing soft-lithography, ion-exchange and sol-gel based fabrication techniques. Waveguide writing and selective etching with three-dimensional design flexibility allows the development of innovative and unprecedented optofluidic architectures using this technology. The work embodied in this thesis focuses on utilising the advantages offered by direct laser writing in fabricating integrated miniaturised devices tailored for biological analysis.

The first application presented customised the selective etching phenomenon in fused silica by tailoring the femtosecond pulse properties during the writing process. A device with an embedded network of microchannels with a significant difference in aspect-ratio was fabricated, which was subsequently applied in achieving the high-throughput label-free sorting of mammalian cells based on cytoskeletal deformability. Analysis on the device output cell population revealed minimal effect of the device on cell viability.

The second application incorporated an embedded microchannel in fused silica with a monolithically integrated near-infrared optical waveguide. This optofluidic device implemented the thermally sensitive emission spectrum of semiconductor nanocrystals in undertaking remote thermometry of the localised microchannel environment illuminated by the waveguide. Aspects relating to changing the wavelength of illumination from the waveguide were analysed. The effect of incorporating carbon nanotubes as efficient heaters within the microchannel was investigated. Spatio-thermal imaging of the microchannel illuminated by the waveguide revealed the thermal effects to extend over distances appreciably longer than the waveguide cross-section.

On the material side of direct laser writing, ultra-high selective etching is demonstrated in the well-known laser crystal Nd:YAG. This work presents Nd:YAG as a material with the potential to develop next-generation optofluidic devices.

To my Father

Acknowledgements

It is a great pleasure to thank everyone who, in one way or another, made this thesis possible.

I am truly indebted to my Ph.D supervisors *Dr. Lynn Paterson* and *Prof. Ajoy K. Kar*. Their enthusiasm, approachability, inspiration and guidance, have undoubtedly made the completion of this study, the most rewarding experience in my career thus far. Their continuous support has been instrumental in helping me develop my skills and pursue my academic endeavours with enough freedom. Without their perseverance, this thesis would have remained a dream.

I gratefully acknowledge the Heriot-Watt University Life Sciences Interface Theme Scholarship that made this research possible.

I would like to thank my colleagues in the Nonlinear Optics and Biophotonics groups for always being so helpful. Thank you *Dr. Graeme Brown* and *Dr. Nick Psaila* for introducing me to the field and lucidly explaining the intricacies of DLW. I would like to thank *Dr. Robert Thomson* and *Dr. Henry Bookey* for the many insightful discussions we've had. Special thanks to *Dr. Stephen Beecher* for being ever-helpful. The trip to India will remain etched in my memory for years to come. I am also thankful to *John Macdonald*, *Rose Mary*, *Ashleigh Barron* and *William Ramsay* for all their help and support throughout the duration of this study.

Dr. Airan Rodenas deserves my gratitude for his contributions on the micro-luminescence and micro-Raman work and the many useful discussions. His hard-working routine and coffee consumption are both conta-

gious!

I would like to express my gratitude to *Prof. Kevin Prior* for training me on using the HF etching facility.

I would like to express my humble gratitude to members of the physics mechanical workshop, especially *Mark Stewart* and *Peter Heron* for their help and advice in designing and machining parts used for this thesis work.

I am grateful for the contributions of my collaborators at the Institute of Biological Chemistry, Biophysics and Bioengineering, especially *Dr. Nik Willoughby* for our insightful discussions on the cell-sorter work.

I would like to thank *Prof. Daniel Jaque* at the University Autonoma de Madrid for his contributions towards the remote thermometry work. I would especially like to thank him for creating a stimulating environment in the lab during his visit to Heriot Watt. *Dani*, it has been an immense pleasure working with you.

I am extremely thankful to my wife *Supta*, for tolerating my eccentricities and whose unwavering support and patience has made this thesis possible. I would especially like to mention my little daughter *Adwita* whose delightful diversions made writing this thesis worthwhile.

Finally, I am truly grateful to my parents *Debotosh* and *Sumita* to whom I owe my existence and my brother *Debanjan* whose steadfast belief in me has always uplifted my confidence.

Contents

List of Tables

List of Figures

Glossary

Greek Symbols

φ	Avalanche photoionisation rate
η	Dynamic viscosity
λ	Free space wavelength of light
μ	Micron ($1\mu = 10^{-6}$)
ν	Frequency of light
ω	Laser frequency
ρ	Density of fluid
σ	Molecular diameter
σ_R	Differential Raman scattering cross-section
ϱ	Mean free path
ξ	Kinematic viscosity

Subscripts

N_t	Number of seed electrons in the conduction band at time t
N_o	Initial number of seed electrons in the conduction band
E_g	Bandgap of material

ϵ_o	Permittivity of free space
ν_o	Resonant frequency
K_n	Knudsen number
m_e	Reduced mass of an electron
n_2	Nonlinear refractive index
$\widetilde{\nu_o}$	Wavenumber of incident radiation
$\widetilde{\nu_{vib}}$	Wavenumber of vibrational mode
r_{cell}	Size of a spherical cell
R_{ec}	Critical Reynolds number
w_o	Beam waist radius

Other Symbols

Bi	Bismuth
c	Speed of light in vacuum, $c = 3 \times 10^8\ m\ s^{-1}$
$\mathcal{L}$	Characteristic length scale
Cr	Chromium
e	Charge of an electron
$\overrightarrow{E}$	Electric vector of optical field
$\overrightarrow{E}_{ext}$	External electric field
Er	Erbium
Yb	Ytterbium
$\mathcal{F}$	External force per unit volume
γ	Adiabatic parameter or Keldysh parameter

h	Planck's constant
Ho	Holmium
k	Boltzmann Constant
$\mathfrak{I}$	Intensity at laser beam focus
mm	Millimetre
$\mathfrak{n}$	Number of photons
Nd	Neodymium
n_{eff}	Effective linear refractive index of material
P	Fluid Pressure
p	Pressure
Q	Quality factor of resonator cavity
$\overrightarrow{r}_{cell}$	Vector defining electroporation site in a spherical cell
T	Temperature
t	Time
Tm	Thulium
$\overrightarrow{v}$	Translation vector
$\mathcal{V}$	Representative velocity scale
$\overrightarrow{u}$	Velocity of fluid stream
Y	Yttrium

Acronyms

AC	Aternating current
AOM	Acousto-Optic Modulator

$ARROW$	Anti-Resonant Reflecting Optical Waveguides
as	Attosecond ($1as = 10^{-18}s$)
CNT	Carbon nanotube
$DBOS$	Dual Beam Optical Stretcher
DC	Direct current
dEP	Dielectrophoresis
$DMEM$	Dulbecco's Modified Eagle Medium
$DMSO$	Dimethyl sulfoxide
DNA	Deoxyribonucleic Acid
δTMP	Induced transmembrane potential
$eGFP$	Enhanced Green Fluorescent Protein
$FACS$	Fluorescence-Activated Cell Sorting
FBS	Foetal Bovine Serum
fL	Femtolitre, ($1fL = 10^{-15}L$)
fs	Femtosecond, ($1fs = 10^{-15}s$)
$FWHM$	Full Width at Half Maximum
H_2O_{di}	Deionised water
H_3PO_4	Orthophosphoric acid
$hPSC$	Human Pluripotent Stem Cell
HF	Hydrofluoric acid
$HL60$	Human promyelocytic leukemia cells
$hMSC$	Human Mesenchymal Stem Cell

IC	Integrated Circuits
IPA	Isopropyl alcohol
$LIDEP$	Light Induced Dielectrophoresis
$LiNbO_3$	Lithium niobate
LoC	Lab-on-a-Chip
LoD	Limit of Detection
$MACS$	Magnetic-Activated Cell Sorting
$MEMS$	Micro-Electro-Mechanical Systems
$mESC$	Mouse Embryonic Stem Cell
MIR	Mid-Infrared
MZI	Mach-Zehnder Interferometer
NA	Numerical aperture of objective lens
NIR	Near-Infrared
nL	Nanolitre, ($1nL = 10^{-9}L$)
PCF	Photonic Crystal Fibre
$PDMS$	Poly(dimethylsiloxane)
$PFPE$	Perfluoropolyethers
PhC	Photonic Crystal
PI	Propidium Iodide
$PMMA$	Poly(methylmethacrylate)
ps	Picosecond ($1ps = 10^{-12}s$)
QD	Quantum dot

RBC	Red blood cell
RI	Refractive Index
RI	Refractive index
RRS	Resonance Raman Spectroscopy
SEM	Scanning Electron Microscope
$SERS$	Surface Enhanced Raman Spectroscopy
SLM	Spatial Light Modulator
SNR	Signal-to-noise ratio
SP	Surface Plasmon
SPP	Surface Plasmon Polariton
SPR	Surface Plasmon Resonance
THG	Third Harmonic Generation
TMP	Transmembrane potential
TO	Thiazole Orange
TW	Terawatt ($1TW = 10^{12}W$)
$2PP$	Two-Photon polymerisation
WBC	White Blood Cell
YAG	Yttrium Aluminium Garnet
$ZnSe$	Zinc Selenide

Journal publications by the candidate:

1. D. Choudhury, W. T. Ramsay, R. Kiss, N. A. Willoughby, L. Paterson, and A. K. Kar, "A 3D mammalian cell separator biochip," Lab on a Chip 12, 948–953 (2012).

2. D. Choudhury, D. Jaque, A. Rodenas, W. T. Ramsay, L. Paterson, and A. K. Kar, "Quantum dot enabled thermal imaging of optofluidic devices," Lab on a Chip 12, 2414–2420 (2012).

3. P. Haro-GonzÃąlez, W. T. Ramsay, L. M. Maestro, B. del Rosal, K. Santacruz-Gomez, M. del Carmen Iglesias-de la Cruz, F. Sanz-RodriÌĄguez, J. Y. Choo, P. R. Sevilla, M. Bettinelli, D. Choudhury, A. K. Kar, J. G. SolÃĺ, D. Jaque, and L. Paterson, "Quantum Dot-Based Thermal Spectroscopy and Imaging of Optically Trapped Microspheres and Single Cells," Small, Early view (2013).

Conference publications by the candidate:

1. D. Choudhury, W. Ramsay, N. Psaila, G. Brown, S. Beecher, R. Kiss, N. Willoughby, S. Pells, L. Paterson, and A. Kar, "Sorting stem cells using a femtosecond laser inscribed biochip," IEEE Photonics Society, 23^{rd} Annual Meeting 216–217 (2010).

2. D. Choudhury, W. T. Ramsay, G. Brown, N. D. Psaila, S. Beecher, R. R. Thomson, R. Kiss, S. Pells, N. A. Willoughby, L. Paterson, and A. K. Kar, "A femtosecond laser inscribed biochip for stem cell therapeutic applications," Proceedings of SPIE 7929, pp 79290P (2011).

3. D. Choudhury, W. T. Ramsay, N. A. Willoughby, L. Paterson, and A. K. Kar, "Ultrafast laser inscription: science today, technology tomorrow," in Proceedings

of SPIE 8307, pp. 83070D (2011).

4. D. Choudhury, D. Jaque, A. Rodenas, W. T. Ramsay, L. Paterson, and A. K. Kar, "Quantum dot thermal imaging of on-chip laser excited microfluidics," CLEO Science and Innovations (2012), paper JTh2A.7.

5. D. Choudhury, L. M. Maestro, W. T. Ramsay, L. Paterson, D. Jaque, and A. K. Kar, "Continuous flow single cell electroporation in an ultrafast laser inscribed optofluidic device," International Conference on Fibre Optics and Photonics (2012), paper T1A.4.

6. D. Choudhury, A. Rodenas, Lynn Paterson, Daniel Jaque and Ajoy K. Kar, "3D Microfabrication in YAG Crystals by Direct Laser Writing and Chemical Etching," CLEO Pacific Rim (2013), paper WPE-14 .

7. M. Mackenzie, D. Choudhury, Lynn Paterson, Rory Duncan and Ajoy K. Kar, "Femtosecond Pumping of eGFP Transfected Human Embryonic Kidney Cells," CLEO Pacific Rim (2013), paper WPJ-2.

Chapter 1

Introduction: Optofluidic devices for biophotonic applications

The term "Optofluidics" was conceived in 2003 at the California Institute of Technology in Pasadena to represent an emerging research field that enables the manipulation of the properties of light and non-solid materials within compact and reconfigurable architectures [1]. Although there are several examples of applications that pre-date the use of this term where concepts of optics and fluidics have been applied such as liquid-core waveguides [2], liquid mirror telescopes [3] and liquid lenses [4], the synergistic integration of the two led to the development of optical waveguides and plasmonic sensors at the turn of the millennium [5]. In the decade that followed, the field of optofluidics underwent an accelerated growth phase during which major advancements were achieved in the design, fabrication methodologies and applicability of the technology. At the time of writing this thesis, optofluidics had acquired the potential to address some of the most pressing societal issues on a global scale including basic healthcare, green energy production, clean water and food safety [6]. This fact is evidenced by the burgeoning number of research articles and patents reported each year involving optofluidic devices and methods that correlate with the aforementioned issues. As revealed by a Google Scholar search with the word "optofluidic" appearing in the title or abstract of an article, in 2012 alone there in excess of 500 journal articles published in this field. The rapid expansion of the field is also reflected by the growing number of scientific workshops dedicated to optofluidics as well as the

increasing interest in optofluidics related work in major scientific conferences around the world. The commercial exploitation of the research in integrated optofluidics has been much more reserved, even though the importance of the field with respect to the commercial and economic landscape is well recognised [7]. This can be attributed to the fact that the technologies for manufacturing such devices are still emerging [8]. While a number of start-up companies with niche ideas and products have been established, the large-scale transformation of laboratory demonstrations into working commercial devices is dependent upon the standardisation of crucial factors pertaining to large-volume manufacture such as appropriate selection of materials, packaging, interconnects and interfacing [7, 8]. It is reasonable to classify optofluidics as being a derivative of microfluidics, otherwise referred to as Lab-on-a-Chip (LoC), which is a comparatively broader and more mature field with its origins in the early 1990s [8]. The ramifications of high-throughput, automated microscale analytical systems have already been likened to the impact of integrated circuits, which brought about radical changes in computation after the invention of microelectronics [9]. The advent of optofluidics has been a major step towards realising this potential.

1.1 Fluid dynamics at the microscale

The definition of the word "fluid" in the Oxford English Dictionary is given as *"a substance that has no fixed shape and yields easily to external pressure; a gas or (especially) a liquid"*. More specifically, a fluid can be defined as a state of matter that continually deforms under an applied shear stress. If V_{system} is considered to represent the volume of a fluidic system, at macroscopic scales, *i.e.* $V \gtrapprox 10^{-3}L$ the principles of fluid mechanics consider the fluid characteristics such as density, velocity, pressure, temperature around a spatially defined volume to be the aggregative response of the properties of a large number of individual molecules within the volume. As the volume is reduced to mesoscopic scales, *i.e.* $V \lessapprox 10^{-4}L$ the molecular fluctuations become a dominating factor on the density of the fluid. Therefore, density no longer remains uniform and varies with temperature, spatial coordinates and the presence of inhomogeneities in V_{system} [10]. This phenomenon has particular significance to microfluidic tools and techniques, which have been developed with an aim to carry out an array of complex analytical tasks with the capability to manipulate femtolitre (fL) to nanolitre

(nL) volumes of a sample. An important characteristic in microscale fluidic streams is the significantly higher surface area-to-volume ratio which, compared to macro-scale systems, facilitates much greater interaction of analytes in a fluid sample with the surface of microchannels that confine it. This is particularly important with respect to the development of biosensors as increased surface area-to-volume ratio leads to improved sensitivity. In order to rationalise the design, fabrication and operational capability of microfluidic devices, the characterisation of the fluid dynamics at the micro- or submicron scale, must be accomplished with as little room for empiricism as possible [11].

Fluid streams at microscales can be considered as an ensemble of molecules and treated using deterministic or statistical methods to ascertain the nature and conditions of flow [10]. A second method can be applied to microscale fluid dynamics which involves considering the fluid stream as being a continuum and infinitely divisible [10]. The applicability of either method is established by comparing the characteristic length-scale ($\mathcal{L}$) with the mean free path (ϱ), which is the average distance travelled by a molecule between collisions and is defined as shown as equation 1.1.

$$\varrho = \frac{kT}{\sqrt{2}\pi p\sigma^2} \tag{1.1}$$

where σ is the particle size, T is temperature and p is pressure. $\mathcal{L}$, as shown in equation 1.2, can be represented as the measure of how a macroscopic quantity, such as density (ρ), changes along the microscale dimension under consideration.

$$\mathcal{L} = \frac{\hat{a}\breve{A}\acute{c}\rho}{|\frac{\partial\rho}{\partial x}|} \tag{1.2}$$

where x is a infinitesimal change in length [11]. The ratio of the mean free path (ϱ) to the characteristic length ($\mathcal{L}$) is a dimensionless parameter termed as the Knudsen number (K_n).

$$K_n = \frac{\varrho}{\mathcal{L}} \tag{1.3}$$

If $K_n \ll 1$, the continuum approach can be applied [11].

A more important parameter, known as the Reynolds number (R_e), describes flow characteristics in fluid mechanics more representatively as it provides a measure of

turbulence in the flow. As expressed in equation 1.4, R_e is dimensionless and is defined as the ratio of inertial to viscous forces in the flow of a fluid stream.

$$R_e = \frac{\rho \mathcal{V} \mathcal{L}}{\eta} \tag{1.4}$$

where, ρ is the density of the fluid and η is the dynamic viscosity. $\mathcal{V}$ is the representative velocity scale and $\mathcal{L}$ is the representative length scale.

For Newtonian fluids, *i.e.* fluids where at every point along the flow stream, the viscous stresses scale linearly with the local rate of strain, the equation of continuity can be written as shown in equation 1.5 [10, 11]

$$\frac{\partial \rho}{\partial t} + \frac{\partial}{\partial x_k} \rho u_k = 0 \tag{1.5}$$

Incompressibility approximations can be applied to fluid flows in the microscale if $\frac{1}{\rho}\frac{\partial \rho}{\partial t} \lll 0$, *i.e.* the density changes of the fluid along the flow are infinitesimally small [11]. In such cases of incompressible flow approximation in Newtonian fluids, the viscous forces dominate the forces of inertial origin, *i.e.* $R_e < 1$. Under certain conditions of pressure and flow velocities, microscale fluid streams exhibit laminar flow *i.e.* streamlined flow without any components perpendicular to the direction of flow. For each system, there exists a threshold value of R_e known as the critical Reynolds number (R_{ec}) above which flow characteristics enter the turbulent regime [10].

The Navier-Stokes partial differential equations describe the microhydrodynamics of the flow of incompressible Newtonian fluids at low values of R_e, the vectorial irrotational form of which is shown in equation 1.6.

$$\frac{\partial \overrightarrow{u}}{\partial t} + \overrightarrow{u}.\nabla \overrightarrow{u} = -\frac{\nabla P}{\rho} + \xi \nabla^2 \overrightarrow{u} + \mathcal{F} \tag{1.6}$$

where, $\overrightarrow{u}$ is the fluid velocity vector and t is time. ξ is the kinematic viscosity ($\frac{\eta}{\rho}$). P is the fluid pressure and $\mathcal{F}$ is termed as the external force component per unit volume ($\frac{F_{body}}{V}$), V being the volume of fluid. The $\frac{\partial \overrightarrow{u}}{\partial t}$ term represents the time dependent inertial component of the flow. The $\overrightarrow{u}.\nabla \overrightarrow{u}$ term represents the nonlinearity in the inertial flow. The $-\frac{\nabla P}{\rho}$ term represents the pressure gradient and $\xi \nabla^2 \overrightarrow{u}$ is the term representing the viscous effects on the flow. For the case $R_e \ll 1$, the inertial effects can be neglected from equation 1.6, which then reduces to the form commonly known

as the Stokes equation as expressed in equation 1.7.

$$-\nabla P + \eta \nabla^2 \overrightarrow{u} = 0 \tag{1.7}$$

Therefore, laminar fluid flow in low R_e schemes is characterised by instantaneity, unique solutions, linearity, time-reversibility, minimised kinetic energy dissipation and reciprocity all of which contribute towards the advantages of microscale devices over conventional macroscale systems [10].

In addition to benefiting from laminar flow conditions, microscale fluidic systems are typically associated with reduced sample and/or reagent consumption and consequently minimised waste products, rapid analysis times [12], better process control [13], lower manufacturing costs [8], disposability and suitability for parallelised operation [14]. There are also some limitations associated with microfluidic systems and the way these devices function [15]. Microfluidic systems are typically designed for specific applications with well-defined functions, hence these devices are very difficult to reconfigure for widening the range of implementation. The method selected to fabricate microfluidic devices often have a limiting impact on their application, and variations in fabrication can also manifest as undefined inaccuracies in their functionality. There is also a growing need to standardise the methods of interconnecting microfluidic devices, which can be universally applied to devices fabricated using different methods [16].

1.2 Optofluidics for biosensing applications

Progress in fabrication methodologies and functional capabilities of miniaturised optofluidic systems has, over the last decade, greatly incentivised the growth of biologically relevant applications. This focus on biological applications owes to the fact that such systems routinely incorporate sample preparation methods and sample delivery routes within the analytical apparatus, creating integrated systems well adapted for biological sensing [17]. Moreover, optofluidic devices can be tailored to be inherently multifunctional. This implies that the sensing method can be configured to either apply optical methods to interrogate fluidic properties or employ the fluidic properties to manipulate the device's optical characteristics. Methods that have been applied for biosensing in optofluidic devices typically involve the measurement of absorbance [18], Raman

scattering [19], fluorescence [20], photoluminescence [21], refractive index [22] and polarisation [23].

The following sub-sections outline a few salient aspects of the detection schemes that are frequently applied in contemporary optofluidic biosensors.

1.2.1 Refractive index based biosensors

Sensing schemes based on measuring changes in refractive index rely on its dependence on the bioanalyte's concentration rather than the number molecules. Therefore, increasing the interaction length between the sensing optical field and the target bioanalyte molecules allows for heightened sensitivity and exceptionally low limits of detection (LoD) to be achieved [17, 22]. This approach is has been used widely due to its label-free mechanism of detection. A number of optofluidic sensing mechanisms have been developed to capitalise on this effect. Precision spatial engineering of metallic or dielectric materials by creating two-dimensional (2D) periodic micro- and nano-sized surface features has been applied to achieve greater interaction between bioanalytes and the probing optical field. Typical examples include plasmonic sensors and photonic crystal (PhC) based planar structures or fibres (PCF). Plasmonic sensing allows the real-time detection of small refractive index (RI) variations resulting from the coupling between optical fields and bioanalytes of interest [22]. Surface Plasmon Resonance (SPR) based sensors rely on maximised confinement of the optical field over a 2D engineered interrogation surface area at the interface of metallic and dielectric materials. The coupling between the optical field with the free electrons at the interface creates strongly confined charge density oscillations known as surface plasmons (SP), which further interact with the optical field to produce electromagnetic waves that propagate along the interface [24]. These waves, commonly referred to as surface plasmon polaritons (SPP) can interact with biological target analyte species. This offers an ultra-sensitive label-free sensing method that has been extensively applied for optofluidic biosensing [25].

Photonic crystals [26] constitute another class of highly-engineered photonic elements capable of enhancing the light-analyte interaction. These remarkable photonic elements are designed from nanostructured low-loss dielectric media with periodic variations in dielectric constant, which can be applied to achieve spectral and directional control of light propagation. PhC biosensors are increasingly being incorporated in

novel biosensor applications. Examples of PhC based biosensing applications include protein concentration detection using a PhC waveguide [27], sensing cancer cell cytotoxicity and proliferation using a 1-dimensional (1D) periodic grating surface structure [28], biomolecular detection using 1D or 2D PhC [29] and deoxyribonucleic acid (DNA) thickness measurements using PCF [30].

1.2.2 Evanescent field based biosensors

Evanescent field based approaches have also been developed for optofluidic biosensing. Guided modes in dielectric optical waveguides typically feature an exponentially decaying tail, which is referred to as the evanescent field. Interferometric or resonator cavity based techniques have been designed to enable target analyte species to perturb the evanescent field. These perturbations result in a local change in the RI along the interaction length, which in turn imparts a measurable phase shift to the propagating optical mode. This simple sensing scheme has led to its extensive use in generating high sensitivity label-free biosensors. Examples of interferometric biosensing applications include virus detection [31, 32], detecting single and multilayered molecular assemblies [33], sensing antibody binding [34] and protein expression analysis [35]. Interferometry based sensing scales with the amount of bound target analytes and thus typically requires long interaction lengths [29]. In comparison, the resonant coupling of light into an optical cavity allows for the efficient use of the long photon lifetimes to enable the generation of compact sensors without compromising sensitivity [36, 37]. The shape, size and material composition of resonators can be tailored to complement the optical requirements for sensing applications [38]. Various resonator designs have been experimentally investigated including toroids, disks, spheres, quadrupolars and posts/pillars. Resonating cavities are impressively effective in achieving interaction lengths significantly longer than their own spatial dimensions. Methods to reliably quantify the high sensitivity of the resonators have also been proposed [39]. Dielectric resonator cavities that are cylindrical, disk-shaped or spherical in geometry are known to support resonances referred to as whispering gallery modes (WGM). The propagation path of these modes are confined along the perimeter of the cavity that sustains selected wavelengths which, at the end of a round trip, return in phase. Microfabrication techniques have allowed the creation of resonators with very high quality factors (Q) , where Q is a

dimensional parameter, defined as shown in equation 1.8. Microresonator cavities with exceptionally high Q factors $\geqslant 10^7$ have been demonstrated [40, 41].

$$Q = \frac{\nu_o}{\delta\nu} = 2\pi\nu_o\tau \tag{1.8}$$

where, ν_o represents the resonant frequency, $\delta\nu$ represents the frequency linewidth and τ represents the photon lifetime. The Q factor describes the rate of energy dissipation with respect to the energy stored in the resonator and scales inversely with the optical losses [36]. Besides the Q factor, sensitivity of a resonator cavity also depends on how efficiently the launched light is extracted from an input element, such as a waveguide, into the cavity [42]. Maximising these factors have enabled the realisation of microfabricated resonators capable of biomolecular detection down to the single molecule level [43]. These microresponsive sensors are well-suited for measuring minuscule ($\sim 10^{-7}$ RIU) changes in refractive index [44] as well as for enhancing the fluorescence signals ($\sim$ 8-fold) of an analyte [45]. Outstandingly low LoD have been achieved using microresonator based biosensors [46].

Microring resonator biosensors are also based on similar working principles as cylindrical or spherical microresonator cavities. These biosensors usually consist of a ring waveguide, which serves as the resonator and a straight waveguide, which is spaced in close proximity to the ring and serves as both the input and output waveguide. Light is typically evanescently coupled into the microring from the input straight waveguide. Under resonance conditions, the intensity of the modes confined within the resonator increases following multiple round trips and are subsequently coupled back to the straight waveguide as the output signal. Ring resonators can be fabricated with Q factors $\approx 10^4$, which is much lower than that of microdisk or microsphere based resonators. Nevertheless, excellent sensitivity, specificity and LoD have been demonstrated using microring resonators using both single [47] and cascaded [48] operating configurations.

1.2.3 Raman scattering based biosensors

Measuring the photon energy changes caused by the inelastic scattering of light upon its interaction with the vibrational and rotational modes in molecular or atomic species in a sample presents an exceptionally sensitive method for biological and chemical

analytics. This type of inelastic scattering is normally referred to as Raman scattering. In comparison with elastic scattering, otherwise termed as Rayleigh scattering, Raman signals are typically lower by a few orders of magnitude [49]. This requires Raman signal acquisition processes to involve long integration times in order to produce a measurable readout with good signal-to-noise ratio (SNR). Typically, Raman signals are quantified by the differential scattering cross-section (σ_R), which is defined as shown in equation 1.9

$$\sigma_R = (\widetilde{\nu_o} - \widetilde{\nu_{vib}})^4 \tag{1.9}$$

where, $\widetilde{\nu_o}$ is the wavenumber of the incident radiation and $\widetilde{\nu_{vib}}$ is the wavenumber of the vibrational mode. Although the Raman effect is associated with excellent specificity, the low σ_R values for biomolecules limit the sensitivity of the technique in bioanalytics[50]. This limitation has been overcome with the advent of Surface Enhanced Raman Spectroscopy (SERS) based sensing schemes that involve molecules attached to nanometre sized metallic structures resulting in significant ($\approx 10^{14}$ increase in σ_R values [51, 52]. SERS based sensing in microfabricated environments has been used for the detection of DNA [19], analysis of enzyme activity [53], bacterial strain identification [54] and biomolecular detection [55].

Recently, Raman spectroscopy has been implemented in an optofluidic architecture using a pair of closely spaced embedded multimode optical fibres to excite the sample and collect the Raman signal [56]. Termed as Waveguide Confined Raman Spectroscopy (WCRS), this simple design is remarkably effective in preventing ambient light from adversely affecting the Raman signal and can be adapted to suit the requirements of other detection platforms such as SERS and Resonance Raman Spectroscopy (RRS). The WCRS based optofluidic sensor has been successfully applied in small volume Scotch whisky purity analysis [57].

1.2.4 Fluorescence based biosensors

Fluorescence based biosensors are based on analytical signals from the fluorescence emission process. Fluorescence is conceivably the most traditional of all methods applied to biosensing. Unlike its use in conventional settings, such as microscopy, the use of fluorescence in optofluidic settings routinely involves its incorporation with other

sensing schemes. In particular, fluorescence based sensing has been found to be very useful in augmenting the LoD in cases involving analytes with low RI values, which renders label-free sensing methods incapable of measuring RI changes [17]. Innovative optofluidic architectures have been designed that use optical field confinement techniques that enable the increased interaction of light with the fluorophores within the sample. Liquid-core waveguides [58, 59], PhC structures [60] and Anti-Resonant Reflecting Optical Waveguides (ARROW) [17, 20] are a few examples that highlight the merger of fluorescence sensing with novel waveguide designs. The use of fluorescence with ARROW has yielded devices capable of extraordinarily low LoD [17]. The main limiting factor of using fluorescence based devices for bioanalytics stems from the autofluorescence and the short-term stability of biological fluorophores. This approach also needs to be carefully implemented in order to avoid possible interference of the fluorophore with the bioanalyte being investigated.

1.3 Non-biosensing applications of optofluidics

Besides biosensing applications, miniaturised devices have also been developed for biologically relevant applications. Amongst the wide array of such applications in the field, label-free cell sorting constitutes an important area with significant relevance to medical applications as well as fundamental biological studies. Another key area of research in this field involves the development of contactless methods to enable the accurate determination of temperature in miniaturised devices. Both the aforementioned areas are investigated in this thesis. Aspects relating to these applications are discussed in the following sections.

1.3.1 Label-free cell separation

There is a growing consensus on the contributory role of variations in the biomechanical and biophysical properties of cells and intracellular structures in the origination and advancement of human diseases. An area of great interest is to understand the inter-relationships between biophysical, biomechanical and biochemical perturbations in the cellular microenvironment with structural variations in the cell membrane, cytoplasmic matrix and in particular, the cytoskeleton [61]. The cytoskeleton is a dynamic,

complex network of proteins that fills the cytoplasmic matrix and is responsible for cell movement, cytokinesis, and the organisation of intracellular organelles. The cytoskeleton also determines the shape of a cell and its mechanical deformability and may undergo remodelling or reorganisation in response to mechanical perturbations [62]. Difference in the cytoskeletal network between various cell types manifests as a discernible variation in cell elasticity [63]. The biomechanical behaviour of the cytoskeleton in a diseased cell is hypothesised to be different from that in the normal state. Cardiomyocytes, for example, normally respond to ion-exchange mechanisms by generating a mechanical contractile force. In a diseased state the mechanical contractility of these cells is reduced, indicating a change in the cytoskeletal properties [62]. The dual beam optical stretcher (DBOS) presents an elegant method to probe cellular deformability. The change in the refractive index at the interface between the cell and the surrounding medium leads to a change in the speed of light in the medium and thus a momentum change that is transferred to the cell which consequently experiences a force. The principle of conservation of momentum applies at the interface and the resulting net stretching force results from backscattering when the reflected light exits the cell [64]. In an experiment utilising the DBOS, radiation pressure enabled cellular deformation of human breast epithelial cells was shown to be a reliable diagnostic parameter for underlying metastatic potential [65]. The epithelial cells with high metastatic potential were found to be $\sim$ 20 % more deformable than non-cancerous cells. The fibre optic DBOS configuration was later translated into a DLW enabled optofluidic device [66], creating the possibility to apply deformability as a sorting criterion in DLW microdevices.

Cellular deformability is also significant in stem cell biology. Deformability has been shown to decrease appreciably with increasing levels of differentiation. Mouse embryonic stem cells (mESC) were found to be 10-times softer than differentiated cells [67] whereas in the case of human mesenchymal stem cells (hMSC), a post-differentiation reduction of $\sim$ 35 % in deformability was observed [68]. These variations strongly indicate that deformability could serve as the simple basis of a separation technique to potentially enable the fractionation of stem cell populations into sub-populations with homogeneous degrees of differentiation. This is particularly important with respect to stem cell therapeutic applications, where live cells are introduced into the human body. The presence of a single undifferentiated cell in the therapeutic implant can lead

to its self-renewal resulting in unwanted medical complications. Thus, there are two important areas in biomedicine which can potentially be influenced using deformability based label-free separation devices.

1.3.2 Thermal sensing in microdevices

The development of LoC devices necessitates the integration of multifunctional components within a compact, portable platform with rapid analyses times. An important functionality is the accurate measurement and control of temperature within the microdevice. The capability to precisely regulate temperature would enable the study of a variety of complex physical, chemical and biological applications within the microdevice. Polymerase chain reaction and protein crystallisation are two important examples in biology that demand strict control over local temperature. Traditionally, the temperature regulation approaches relied on the use of macroscopic Peltier stages or pre-heated fluids flowing through the microsystem which were limited by lack of integration of the heating and cooling components. Therefore the development of contactless, integrated methods of thermal sensing gained importance.

In LoC devices, the small dimensions of microchannels introduce complications in the accurate determination of their internal temperature. The reduced volumes involved with such micro-scale devices make the use of traditional 'contact' based methods of temperature measurement difficult to implement. The dimensional constraint associated with micro-scale devices led to the development of 'remote' thermometry techniques that can be realised using recently emerging optical methods. These methods are based on the incorporation of luminescent particles or fluorescence moieties within the fluid inside microchannels whose emission spectrum is dependent on temperature in terms of spectral shape, intensity or lifetime [69]. Applying methods such as confocal microscopy, it is possible to perform a detailed analysis of the spectral features and achieve intra-channel thermal sensing and imaging. The use of fluorescent moieties or luminescent nanoparticles provide spatial resolutions significantly higher than those achievable using micro-thermocouples [70]. High resolution thermal images of fluids confined within micro scale environments have also been reported using organic compounds such as rhodamine and its derivatives, based on the large temperature-induced variations of their fluorescence intensity and lifetime [71]. The fluorescent compounds

were incorporated into the fluid either in the form of a colloidal suspension [71] or by encapsulating within a micro-droplet [72]. These approaches provided a thermal resolution of 1^oC–2^oC with micron-scale spatial resolution and are capable of thermal imaging in microfluidic environments involving optical traps. Despite these excellent results, the use of organic compounds is typically associated with limitations such as photo-deterioration and low molar absorption coefficient. Temperature-sensitive fluorescent proteins have also been applied to achieve high spatio-temporal resolution imaging in microfluidic devices [73]. However, the temperature control mechanism was not integrated within the device and involved a pair external Peltier devices set at different temperatures. Fluorescent polymer nanoparticles have been applied to achieve the *in situ* temperature measurement in microfluidic devices based on the Brownian motion [74]. This method decoupled the temperature measurement from fluorescence intensity or lifetime of the fluorescent species and measured spatial temperature variations in three dimensions based on the well-characterised temperature dependence of Brownian motion. However, the method is difficult to apply in convective flow situations. Aqueous microfluidic environments have also been thermally mapped by applying a water-soluble, thermo-responsive polymer poly(N-isopropylacrylamide) labelled with a benzofurazan as a sensitive fluorescence-lifetime probe [75]. The temperature dependence of the average fluorescence lifetime was based on changes in the microenvironment of the fluorescent label as a consequence of polymer phase transition at relevant temperatures. Impressive thermal resolution of $\leq 0.1\ ^oC$ was reported using this method. However, the application of this method in delicate biological settings is prone to cytotoxicity. The work done by Baffou *et al.* [76] introduced the application of fluorescence polarisation anisotropy to quantify and map temperature increments in the vicinity of nano-sized heat sources. Thermal mapping of the landscape around plasmonic 250 nm wide and 30 nm thick gold nanowires and colloidal 50 $nm \times 12\ nm$ gold nanorods heated by near-infrared light was reported. Using a confocal microscope with a 1.25 NA focusing optic, fluorescein molecules were excited using a linearly polarised 473 nm continuous wave (cw) laser beam while heating of the nanostructures was performed coaxially using 775 nm illumination. The authors achieved a temperature accuracy of $0.1\ ^oC$ and a spatial resolution of 300 nm, which was determined from the resolution of the confocal setup. Since the Brownian dynamics of the fluorophore dictates the anisotropy, the method provided a direct and reliable measurement of

the sample local temperature which was not affected by fluctuations in laser power. In addition, the method was reported to be insensitive to photobleaching or thermal damage of the fluorophores. In comparison with this report by Baffou *et al.*, the work undertaken in chapter 4 of this thesis integrates the NIR illumination in an optofluidic setting using a monolithic waveguide and applies the thermally sensitive properties of QDs and CNTs which presents yet another method of of contact-less thermometry in microfluidic environments. The relevant properties of QDs and CNTs that enable their application as temperature sensors and heaters are discussed in section 4.1 in chapter 4. The thermal resolution achieved in the work carried out in this thesis is comparable to that reported by Baffou *et al.* [76]. The spatial resolution, which is governed by the resolution of the confocal microscope setup, is lower than that reported by Baffou *et al.* as a result of a lower NA lens being utilised. The setup is described in figure 4.2 in chapter 4.

1.4 Microfabrication techniques for optofluidics

There is no clear line of demarcation that dissociates microfluidic fabrication methods from optofluidic fabrication techniques. Although methods to fabricate fluidic and optical components independently are well established, techniques to implement their integration onto a single chip-based device are still being developed. As there is no universally applicable methodology to fabricate integrated optofluidic devices, design and functional variabilities exist between devices fabricated using known techniques. Fabrication methods are typically material dependent and can be broadly categorised as being polymer based, glass based and silicon based techniques.

Silicon based fabrication methods that were derived from the development of silicon Integrated Circuits (IC) and subsequently Micro-Electro-Mechanical Systems (MEMS) technology were applied to fluidic microsystems at an early stage. However, limitations of using silicon based devices for fluidic sensing applications quickly surfaced due to its sub-bandgap ($\lesssim 1.1\mu m$) opacity leading to incompatibility with standard optical detection systems [8]. Polymers were adopted as a suitable alternative due to the important advantages these provide over silicon such as lower costs, relative ease of fabrication, biocompatibility, elastomeric properties, optical transparency and permeability to gases. With the use of polymers, microfluidic fabrication has evolved from the

exploratory stages to a well-established fabrication methodology. Within the context of polymer fabrication, soft lithographic techniques have been particularly advantageous. Soft lithography was proposed as an alternative to the traditional photolithographic technique which was capable of transferring well-defined, high-quality geometric shapes on a pre-designed mask to the surface of a silicon wafer. Stemming from a broadly similar working principle, the term soft lithography represents a unified approach that overarches a set of non-photolithographic techniques based on printing and replica moulding to create micro- and nano-sized structures [77]. Soft lithographic techniques are much more suitable for microfluidic fabrication and have been predominantly involved the use of poly(dimethylsiloxane) (PDMS). Other polymers suitable for this method include poly(methylmethacrylate) (PMMA), hydrogels, elastomers and perfluoropolyethers (PFPE) [78]. Qin *et al.*[79] provide a comprehensive review on the various aspects on soft lithographic micro- and nanofabrication. In addition to standard fluidic microscale components, exceptionally complex microfluidic features have been successfully demonstrated using soft lithographic methods [37, 80]. There are limitations of using polymers for developing sensor applications including incompatibility with common solvents, low damage threshold to focused laser radiation and autofluorescence [81]. There are other fabrication methodologies that have been explored for creating microscale fluidic devices such as plasma activated microplating, laminated object manufacturing and shrinky-dink approaches[82], however none have quite had the impact of soft lithographic techniques and its variants. Over the past decade, an entirely new microfabrication technique has emerged that is based on the application of ultrashort NIR laser pulses in dielectric materials to fabricate optical and microfluidic components. This technique is outlined in the following paragraph.

Femtosecond laser microfabrication

The interaction of intense, focused ultrashort ($\sim 50 - 500 femtoseconds(fs)$) laser pulses with transparent dielectric materials is known to permanently modify the material's chemical properties, which manifests as two unconnected and unprecedented phenomena. First, the RI of the material is altered within the focal volume, enabling the formation of optical waveguides within the bounds of the material [83]. Second, the local chemical bond structure within the focal volume is redistributed in such a way that the laser modified regions can dissolve significantly faster than the bulk

material in a chemical etchant solution [84]. These property modifications originate from nonlinear energy transfer processes that occur within the focal volume. These observations established a new method capable of potentially addressing the integration requirements in optofluidic microfabrication, leading to the advent of Femtosecond Laser Microfabrication (FLM) also referred to as Direct Laser Writing (DLW). Unlike soft lithographic methods, the DLW technique does not require expensive clean-room facilities. It offers three-dimensional (3D) design freedom, is applicable to a numerous biocompatible substrate materials including glasses, crystals or polymers and is ideally suited for rapid prototyping.

Within the domain of optofluidics, the synergistic integration of photonic and fluidic components in DLW enabled devices offers the possibility to create alignment-Âŋfree sensors with novel functionalities with the potential to enhance detection capability. Over the last 15 years, efforts to understand and establish control over the fundamental processes governing this technique has enabled DLW to emerge as a powerful microfabrication tool driven by its distinctive multifaceted potential to create low-ÂŋâĂŘloss, 3D optical waveguides as well as chemically etched, high aspect ratio, buried microfluidic channels over a wide choice of substrate materials. DLW allows the formation of highly stable, monolithic LoC environments offering significant improvements in device fabrication times, repeatability and reliability. The work described in this thesis explores the capabilities of DLW in developing novel biochips showing results that underscore the unique advantages offered by DLW in generating solutions to future challenges in optofluidics.

1.5 Thesis outline

This thesis embodies an exploratory study on the applicability of DLW in developing integrated biosensing and manipulation devices. The work presented comprises a progressive investigation into the capabilities of DLW by incorporating increasing levels of complexity as detailed in *chapters 3* to *5*. *Chapter 3* details a deformability based cell-sorting method involving DLW network of channels, *chapter 4* presents a non-invasive temperature sensing method for microscale environment, which involves a DLW fluidics and optical waveguiding. *Chapter 5* describes the formation of fluidic

features inside a laser crystal. As the work carried out in each chapter involves diverse areas of application, brief reviews for the respective areas are provided at the beginning of each chapter.

Chapter 2 includes a detailed discussion on the direct laser writing process. The fundamental nonlinear optical processes that govern the DLW technology are discussed. The chapter describes methods to fabricate fluidic features and waveguides along with methods that have been developed to control the fabrication process.

Chapter 3 is presented in two parts. The first part presents an investigation into the DLW methods that allow the controlled selective etching of fluidic features in fused silica that differ in dimensions by three orders of magnitude without compromising aspect-ratio. The second part derives optimum parameters from the first part and presents the design and fabrication of a prototype cell-separator with high aspect-ratio structures based on the cytoskeletal deformability of mammalian cells.

Chapter 4 details an investigation into the use of semiconductor quantum dot nanothermometry to enable the non-invasive measurement of temperature within microfluidic environments in fused silica. Spatio-thermal mapping is performed showing the temperature distribution in an aqueous environment within a microfluidic channel due to the presence of a monolithically integrated near-infrared optical waveguide. The effects in temperature due to the presence of absorbing particles within the microchannel are discussed.

Chapter 5 describes the application of DLW to fabricate microfluidic features in neodymium doped yttrium aluminium garnet (Nd:YAG) crystals. Laser written structures exhibit remarkable etching selectivity with picometre scale surface roughness in the unmodified YAG. Micro-luminescence and micro-Raman studies are performed on the laser written features to explain the selectivity in chemical etching. The implications of realising optofluidic devices in laser gain media are discussed.

Chapter 6 discusses the conclusions reached from the work undertaken in the thesis and presents prospects for further work.

1.6 Discussion

The practical LoC microdevice can be envisaged as a recyclable, robust, inexpensive, small-footprint muntifunctional apparatus with high-sensitivity detection capability that can operate at the point-of-care. Naturally, much progress still needs to be made in all aspects of miniaturising technologies before any such device can be realistically achieved. The miniaturised implementation of the biosensing techniques outlined in section 1.2 is not a trivial task technologically. Although the integration of photonic elements with fluidics has circumvented the problems associated with traditional systems used in biological and chemical analytics, limitations with respect to the sample delivery and control of liquids in micro- and nanosystems need to be overcome. In addition, the optical sources and detectors that form a critical part of the sensing platform are still bulky. Thus, miniaturised optofluidic biosensors are still very much confined within the laboratory. In terms of fabrication aspects, although a wide selection of materials is available for developing specific sensor techniques there is a need to identify and standardise a set of materials that can be more widely applicable over a range of fabrication schemes. Well-characterized materials both in terms of optical properties and chemical stability are a necessity especially with respect to biosensors. These limitations will eventually be overcome. At present however, microfluidic and microphotonic components can either be concurrently fabricated using the same materials or individually fabricated followed by a post-assembly step [37]. Nonetheless, the true, single-step integration of both functionalities within a single substrate material is an intricate requirement even using contemporary methods and presents an exciting area to be explore. This thesis addresses some of the problems associated with the development of this technology.

Chapter 2

Review: Femtosecond laser microfabrication in bulk transparent dielectrics

Light matter interactions lie at the heart of our understanding of the world around us. Throughout the history of modern science, concerted efforts have been made to gain insights into how different types of materials behave when light is incident upon them. The materials can either be of natural origin or artificially engineered. A fascinating example of light matter interaction that occurs in nature is the process of photosynthesis. The emergence of lasers in the middle of the last century invigorated this learning process in an unprecedented manner, the lasing process itself being an excellent artificially engineered example of the phenomenon. In the following decades, the fields of photonics and material sciences progressed in an interdependent manner leading to the emergence of several technological innovations that we come across in day-to-day aspects of our lives such as compact and blu-ray disc players, displays, solar energy panels and telecommunications. Two compelling examples where material engineering is applied to control light with unprecedented facility at the sub-wavelength scale include photonic band-gap materials, which are considered as the optical analog of semiconductors and the super-material graphene. In biosciences,the interaction of light with fluorescent moieties in living matter forms the underlying principles of a vast majority of biosensing techniques leading to advanced diagnostic approaches. Light

matter interactions also serve as a 'test-bed' for more esoteric applications such as quantum-information-processing.

The response of a material to an incident beam of light depends on various factors that govern the transfer of energy from the impinging photons to the constituent electrons, atoms or molecules of the material. Transfer of energy is intrinsically dependent upon a range of properties of the incident light and how these relate with the material under consideration. An isotropic dielectric material allows a collimated beam light to propagate along a direction specified by its Poynting vector until the beam is attenuated completely or it encounters an interface with a different material. This is based on the assumption that the impinging photon energy is just enough to perturb the electrons, atoms or molecules of the material to cause these to oscillate. In most cases, these oscillations occur at the frequency of the incident light and re-emit energy isotropically as light of the same frequency, a phenomenon known as Rayleigh "scattering" of light. If the phase of the emitted light does not match that of the incident light, the emitted light interferes destructively with the incident light leading to "attenuation" of the original beam. In the case of almost complete attenuation, the incident light is said to be "absorbed" by the material. The above provides a qualitative description of the phenomenon of linear absorption, which can be mathematically expressed by the well-known Beer-Lambert law, as shown in equation 2.1

$$I(z) = I_o e^{-\alpha z} \tag{2.1}$$

where, I_o is the intensity of the incident light, α is the linear attenuation coefficient, z is the length the light travels into the material and $I(z)$ is the intensity of light at a distance z inside the material.

Dielectric materials also exhibit a nonlinear response to the incident light at high intensities. The DLW technique is based upon such nonlinear interactions of light with dielectric materials. This chapter begins with a discussion on the underlying nonlinear energy transfer processes that influence the DLW technique. Following this discussion, the chapter presents a review on the state-of-the-art of DLW, taking into consideration aspects relating to photonic as well as fluidic component microfabrication. The respective optimisation and characterisation procedures are also discussed. Finally, the chapter introduces the DLW microfabrication setup that has been applied

in undertaking the experimental work presented in this thesis.

2.1 Ultrashort pulses in transparent dielectrics

Within the field of DLW, optical pulses are usually termed as "ultrashort" if their pulse duration lies within the fs to picosecond (ps) time-scale, although much shorter pulses with attosecond (as) pulse duration have been achieved [85]. Pulse duration plays a determining role in the energy transfer processes that occur during the interaction of focused ultrashort pulses with a dielectric material. With particular emphasis on DLW, increasing the pulse duration from fs to ps significantly alters the dynamics of energy transfer from the optical pulses to the material, as discussed in section 2.2.3. DLW involves periodic trains of femtosecond laser pulses that are focused within the volume of dielectric materials that do not exhibit linear absorption at the wavelength of the femtosecond laser, *i.e.* these materials are transparent at the laser wavelength. The focusing of optical pulses with such short temporal profiles within transparent dielectrics generates extremely high intensities confined within the focal volume, which results in irreversible structural modification of the material. Assuming the absence of aberrations, the spatial confinement of these structural modifications is driven by nonlinear processes and depends on the intensity of light, the focusing optics, the pulse duration and pulse energy and are typically of the order of a micrometre (μm). Due to the highly localised nature of the nonlinear absorption, a transparent dielectric material substrate can be translated in 3D with respect to the laser beam focus to produce desired high-precision features without affecting the bulk material. A detailed discussion on the DLW fabrication setup is presented in section 2.5.

2.2 The dynamics of energy transfer

The short pulse duration (fs) makes it possible to attain exceedingly high peak intensities at the laser beam focus even using low pulse energies [86]. As an example, 100 nJ pulses with a duration of 100 fs when focused onto a spot of 2 μm, produces a peak intensity $\sim 10\, TW\, cm^{-2}$. This intensity is comparable with the electric field that binds the valence electrons to the ionic core in the atoms that constitute the material. Based on the timescales of the dynamical processes involved, the process of energy transfer

can be broadly categorised into three principal mechanisms [87]. The first mechanism is that of partial energy transfer from the optical pulses to the bound electrons of the material through nonlinear photoionisation processes which generate a free electron plasma. The second mechanism involves the free electron plasma relaxation dynamics which involves the transfer of the electron energy to the material lattice. The final mechanism involves structural modifications within the material lattice as a result of these processes.

2.2.1 Nonlinear photoionisation

The photoionisation process by which the energetic electrons are promoted to the conduction band depends upon the intensity and energy of the incident light and can occur through two distinct pathways – multiphoton-ionisation and/or tunnelling ionisation [88]. In the case of low intensity pulses at high laser frequencies, nonlinear photoionisation is predominantly a multiphoton mechanism whereas at high intensities and low laser frequencies, the tunnelling effect takes over [88]. Multiphoton ionisation occurs when more than one photon is required to excite the valence electron into the conduction band. If $\mathfrak{n}$ photons are required to initiate the ionisation, then the total photon energy must satisfy $\mathfrak{n}h\nu > E_g$, where h is the Planck's constant, ν is the frequency of the incident light and E_g is the material bandgap. In contrast, the strong electric field of the optical pulses at high intensities suppresses the Coulomb potential well that separates the valence band from the conduction band. Energetic electrons in the valence band can therefore, tunnel through the distorted barrier into the conduction band. The adiabatic parameter (γ) proposed by Keldysh [89] provides an elegant method that relates the two mechanisms of nonlinear photoionisation. The adiabatic parameter is expressed as shown in equation 2.2

$$\gamma = \frac{\omega}{e}\sqrt{\frac{m_e c n_{eff} \epsilon_o E_g}{\mathcal{I}}} \tag{2.2}$$

where, ω is the laser frequency, $\mathcal{I}$ is the intensity at the laser beam focus, m_e and e are the effective electronic mass and charge respectively, ϵ_o is the permittivity of free space, n_{eff} and E_g are the effective linear refractive index and bandgap of the material respectively. Keldysh proposed that the dominance of multiphoton ionisation

or tunnelling ionisation can be delineated by a transitional γ value of 1.5. For $\gamma \ll 1.5$, tunnelling effects dominate, whereas for $\gamma \gg 1.5$, multiphoton ionisation dominates. For $\gamma \sim 1.5$, nonlinear photoionisation can be considered to occur as a combination of both processes.

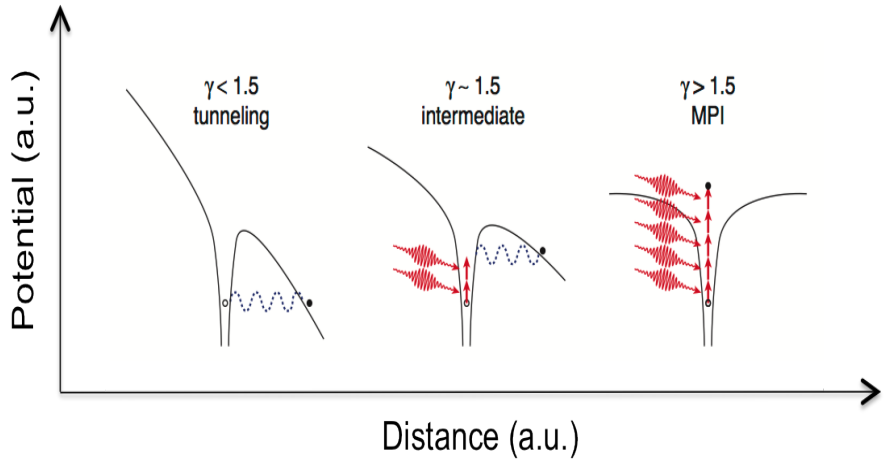

Figure 2.1: Schematic illustration of the photoionisation mechanisms and corresponding adiabatic parameter, showing processes of liberating an electron from the Coulomb potential [88].

As an example, for a contemporary DLW microfabrication system featuring mode-locked pulses with a duration of ~400 fs at 1047 nm focused using a 0.4 NA aspheric lens to a 2 μm spot size within a substrate of fused silica ($n_{eff} = 1.458$) reveals $\mathcal{I}$ to be $\sim 10^{13}\ W\ cm^{-2}$. Consequently, evaluation of the adiabatic parameter using equation 2.2, reveals $\gamma \sim 1$. Therefore, nonlinear photoionisation in such a case occurs as a combination of both multiphoton ionisation and tunnelling ionisation processes. The adiabatic parameter relating to the laser writing conditions for the work undertaken in this thesis have been evaluated in chapter 3, chapter 4 and chapter 5 respectively.

2.2.2 Avalanche photoionisation

Once an electron is promoted to the conduction band by absorbing energy from the leading edge of an ultrashort optical pulse, it is no longer bound to the ionic core it left behind and is free absorb energy linearly from the rest of the pulse [87]. During its

lifetime in the conduction band, the electron may move to higher energy states in the conduction band after undergoing several successive linear photon energy absorption steps. As a consequence, the free electron will possess sufficient energy to enable the impact ionisation of a second bound electron in the valence band. Following this impact ionisation, the two free electrons near the conduction band minimum can undergo the same linear absorption processes leading to further ionisation of several bound electrons. This free-carrier absorption process is repeated as long as a strong optical field is present, thus exponentially enhancing the energy transfer process which gives rise to avalanche photoionisation. A prerequisite for avalanche ionisation to occur is the presence of a sufficient number of seed electrons in the conduction band. The electron density in the conduction band can be expressed as shown in equation 2.3

$$N_t = N_o e^{\varphi t} \tag{2.3}$$

where, N_t is the number of electrons in the conduction band at any time t, N_o is the initial number of seed electrons present in the conduction band and φ is the avalanche ionisation rate. The seed electrons can originate from either multiphoton/tunnelling ionisation processes or from thermally excited defect states or impurities [88]. The electron plasma density increases to about $10^{29}\ m^{-3}$, at which point the natural frequency of the plasma becomes resonant with the laser frequency[87], the plasma exhibits strong absorption of the incident photons. This value is termed as the critical plasma density beyond which optical breakdown of the material occurs. In the case of fused silica, the critical electron plasma density corresponds to a threshold focal intensity $\sim 10^{13}\ W\ cm^{-2}$ [90].

2.2.3 A temporal perspective

The phenomenon of energy transfer from an ultrashort optical pulse to the dielectric material lattice incorporates a series of complex, dynamical processes. An insight into the timescales involved in these nonlinear processes and their inter-relations would lead to an understanding of why fs pulses are suitable for DLW applications. Material modification resulting from focused fs laser pulses are different from that due to laser pulses of ps duration. [87]. In the case of fs pulses, the nonlinear photoionisation occurs faster than the time taken for the energy to be transferred to the material lattice,

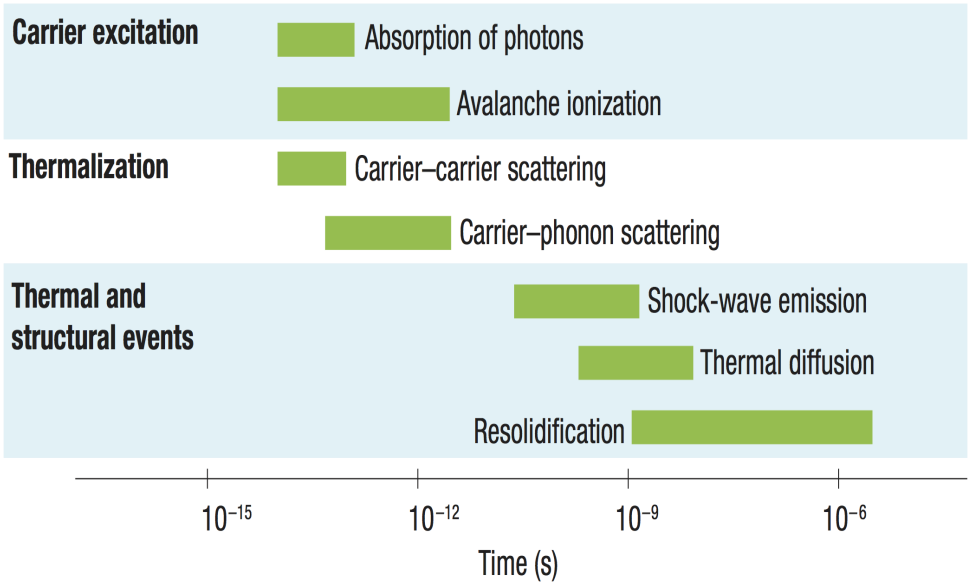

Figure 2.2: Illustration showing the temporal evolution of the physical phenomena associated with the interaction of a femtosecond laser pulse with transparent materials. The green bars represent the typical timescales for the associated energy transfer or relaxation process.[87]

otherwise known as the electron-phonon scattering time [91]. Thus, a fs pulse ends before the energised electrons can dissipate their energy into the lattice *via.* phonon mediated interactions, which occur over ps timescales. A few nanoseconds (ns) later, structural modifications originate from the focal volume *via* pressure wave generation [92, 93]. Finally, the onset of relaxation occurs in the microsecond timescale leading to the dissipation of thermal energy and re-solidification of the material [87]. In the case of fs pulses, there is no requirement for defect electrons to initiate the photoionisation process. This makes fs laser induced material modification a deterministic phenomenon [91]. This fact underscores the practical applicability of fs laser material processing.

Optical pulses with a longer pulse duration, *i.e.* ~ 10 ps or longer, exhibit different energy transfer processes in contrast to fs pulses. The electron-phonon scattering timescales match that of the pulse duration leading to more pronounced thermal effects. Thermal diffusion becomes the predominant energy transfer mechanism [94]. The material temperature in the irradiated region rises significantly leading to struc-

tural damage of the material. Unlike fs laser pulses, the longer ps pulses provide a much longer duration, and therefore a higher probability, for an exponential increase in electron density in the conduction band [88]. As a result, avalanche ionisation occurs more efficiently, seeded by impurities, defect states and thermally excited electrons. This dependence on impurities makes ps pulse processing of materials a statistical phenomenon, causing the lowering of the optical breakdown threshold of the material, the value of which cannot be determined easily.

2.3 Regimes of material modification

The effects of fs laser pulses in fused silica were first demonstrated in 1994 [95]. Two years later, Davis *et al.* reported the discovery of refractive index changes when 120 fs pulses were focused inside silica based dielectrics [83]. Several studies have since been undertaken with the aim to unravel the physics behind structural modifications induced by focused ultrashort pulses. While the principles governing the nonlinear optical pulse energy absorption, the free electron plasma formation and the transfer of energy to the material lattice are well-recognised, as discussed in section 2.2, the dynamics of subsequent material modification phenomena are not yet fully understood. There are various parameters that may affect the manner in which the material is modified. These parameters include pulse properties such as energy per pulse, duration, repetition rate, polarisation, wavelength; sample exposure characteristics such as focusing optics, translation speeds and material properties such as bandgap, thermo-optic coefficient, lattice structure and thermal conductivity to name a few. The material modifications for any dielectric material can be broadly categorised into three regimes - the homogeneous refractive index modification regime [97], the nano-grating formation regime [98, 99] and the void formation regime [100]. With particular reference to the DLW microfabrication of optofluidic devices, the refractive index modification and nanograting formation regimes are particularly significant. In fused silica, which is the most commonly applied material in DLW microfabrication, the three material modification regimes can be delineated solely based on incident pulse energy [96]. The aspects relating to the different material modifications that occur when fs laser pulses are focused in fused silica are discussed as follows.

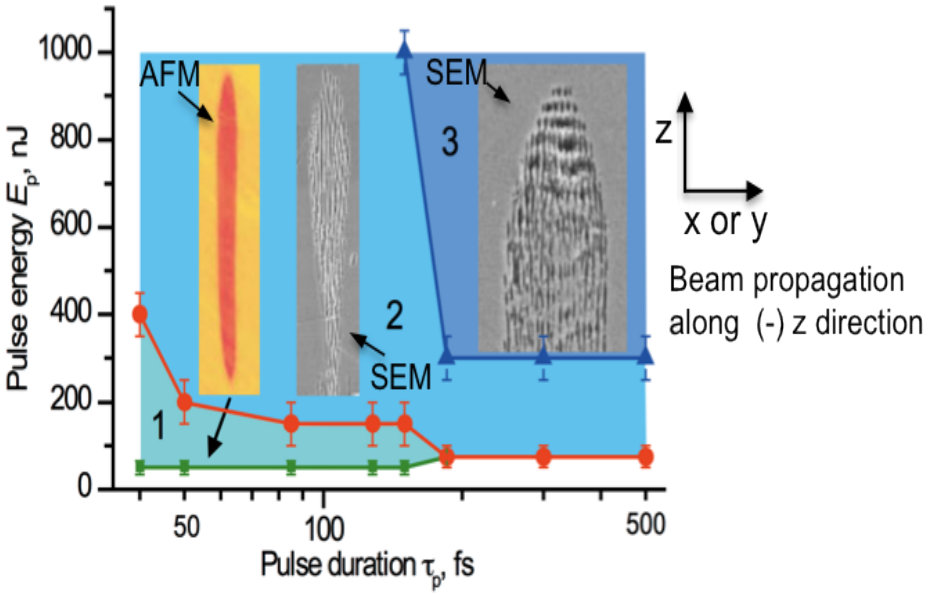

Figure 2.3: Plot showing variation of pulse energy versus pulse duration defining three regimes of material modification using a 0.65 NA focusing optic. Regime 1 produces smooth modification as shown by the AFM inset. Regime 2 constitutes nanograting formation (SEM inset) and Regime 3 results in complex disrupted regions interconnected with nanocracks in the top portion of the modified region (SEM inset). The AFM and SEM images shown reveal the cross-section of material modification in the focal volume. The writing beam direction is the same for all three regimes as shown in the figure [96].

2.3.1 Refractive index modification regime

The material modification threshold for fused silica can be defined as the minimum fs pulse energy required to induce structural modification. The fused silica modification threshold is $\sim 50\ nJ$ for pulse durations less than $\approx 150\ fs$ [101]. When the energy of the focused fs pulses is marginally higher than the material modification threshold, smooth structural modifications occur, which alter the refractive index of the material within the focal volume [83]. If the substrate is translated through the laser focus in 3D, this homogeneous structural modification allows the fabrication of low-loss optical waveguides within the volume of the material. This regime of homogeneous modification can only be achieved within well-defined, narrow parameter windows. Although much work has been undertaken in applying this phenomenon to achieve innovative

DLW micro-scale devices, answering the questions pertaining to the physical mechanisms that allow fs laser pulse induced structural modifications to manifest as a change in refractive index remains open for research. The two main hypotheses currently being considered to explain the origin of refractive index change are densification and the formation of colour centres in the fs pulse modified regions. The basic structural unit of the network of silicon-oxygen bonds in fused silica is tetrahedral. Raman and photo-luminescence spectroscopy of the refractive index modified regions in fused silica have revealed an increase in 3- and 4-membered rings in the silica network, which lowers the overall bond angle leading to an increase in density [102]. fs pulse induced colour-centres have also been suggested as a possible origin of refractive index change [103]. However, the above mentioned hypotheses are not universally applicable to all dielectric materials. The contribution of densification and colour-centre formation depends upon material properties such as composition and lattice structure. In addition, differences in appropriate waveguide fabrication conditions can introduce variabilities in refractive index modification. In materials such as multicomponent glasses refractive index change can be positive, negative or non-uniform [104], which adds material dependent complexities to existing hypotheses. Therefore, a complete understanding of how focused fs laser pulses induce refractive index modifications in transparent dielectric materials has not yet been accomplished [105]. DLW has been extensively applied in this regime to fabricate optical waveguide enabled devices in passive and active materials as well as micro-optical elements, these applications are described in section 2.8. So far the maximum refractive index change (Δn) reported is $\sim 10^{-2}$ [106] although typically Δn is $\sim 10^{-3}$ [107].

2.3.2 The nanograting formation regime

Increasing the incident pulse energies to values higher than the refractive index modification regime leads to the formation of sub-diffraction-limited, well-defined, evenly-spaced, nano-sized planes in the fs laser modified regions of the material, which are termed as self-organised nanogratings [96]. These nanostructures were first discovered in 1999 as fs laser enabled microscopic birefringent structures [108], and were later found to be strongly dependent on the polarisation of the incident fs laser pulses [101]. The orientation of these nanogratings were found to be orthogonal to the electric

field vector of the laser beam ($\overrightarrow{E}$). This phenomenon was explained as a structural manifestation originating from the interference between the incident optical field and the electric field of a free electron plasma wave [99]. The average periodicity of the nanogratings was measured to be $\approx 250\ nm$ [101] in the case of sub-250 kHz repetition rate laser pulses and theoretically modelled to scale linearly with the incident pulse wavelength [109] and inversely with n_{eff}. However, the periodicity is roughly independent of the pulse energy and duration [98]. The fact that the nanogratings maintained their average periodicity over substrate translation lengths in the millimetre scale indicated the existence of a self-organising driving mechanism governing their formation. The morphology of the nanogratings vary drastically when the polarisation is changed from linear to circular. The orthogonality of their orientation with $\overrightarrow{E}$ as well as the order is lost in the latter case [101]. The nanogratings also exhibit a dependence on pulse duration [98, 101]. The nanogratings were found to exist over a wide pulse duration window ranging from 40 to 500 fs, although disruption to the order in these structures set in at higher pulse durations and pulse energies [96]. The dependence of nanograting formation in fused silica on laser repetition rates has also been studied. While nanogratings were found to exist for a wide range of repetition rates ranging from 40 kHz to 9.4 MHz, a strong inverse dependence of the periodicity was observed with the number of incident pulses. The periodicity was observed to reach a saturation value of $\sim 150\ nm$ beyond corresponding to about 3000 laser pulses, beyond which the periodicity remained virtually independent of the repetition rate [110, 111]. Nanograting formation has recently been implemented in the DLW fabrication of polarisation-sensitive optical features in fused silica [112].

Nanogratings do not occur in all silica based materials and in general, only a few different materials possess the ability to generate such structures. There is evidence of their formation in exotic materials such as chalcogenide glasses [113]. However, the nanogratings formed in fused silica using fs laser pulses exhibit enhanced chemical etching compared to the unmodified material, a phenomenon that has significant implications in the DLW microfabrication of fluidic elements. Extensive work has been done in characterising the etching phenomenon and applying it to fabricate DLW optofluidic devices, these aspects are discussed in section 2.7.

2.3.3 The void formation regime

Increasing the incident fs pulse energy beyond the nanograting formation regime increases the peak intensities at the focal volume to elevated values, which enables the deposition of optical energy higher than the ablation threshold of fused silica. The energy transfer by the free electron plasma into the material lattice is accompanied by the formation of pressure waves that lead to the creation of voids and micro-explosions within the volume of the material. These voids are incapable of confining light or exhibiting selective chemical etching. However, their conceivable use in 3D memory storage applications has been investigated [114].

2.4 Two-photon polymerisation using DLW

Photosensitive polymers constitute those dielectric resins that undergo a change in physical and chemical properties when exposed to light. Tightly focused fs laser pulses can induce two-photon absorption leading to spatially confined polymerisation of the monomeric molecules of the photosensitive material. The nonlinear nature of the energy transfer mechanisms involved enables its application in fabricating complex 3D sub-diffraction limited structures in such materials [115]. Two-photon polymerisation (2PP) of the desired 3D structures inside the volume of the photosensitive material requires a subsequent development step involving the removal of the non-illuminated regions. The 2PP technique provides superior quality and higher structural resolution in comparison with one-photon stereolithography methods [115]. The direct writing capability is well-suited for implementation of high-resolution 3D structures embedded within LoC microdevices. The work done by Amato *et al.* [116] is a clear demonstration of this possibility. This work [116] reported the fabrication of a 3D porous filter by 2PP integrated in an already sealed commercial LOC aimed at separating nanoscale from microscale elements. Fabrication was performed using a mode-locked Ti:sapphire laser with 87 MHz repetition rate, 40 fs pulse width, 790 nm central wavelength and an average power of 400 mW. A 1.4 NA objective was used to polymerise a hybrid organic–inorganic sol–gel (SZ2080). The filter, with an average pore size of $\sim$ 1 μm was validated for plasma extraction from whole blood samples. Using the 2PP approach to microfabrication, significant work has been undertaken in trying to achieve

higher spatial resolutions of the polymerised structures. The resolution achieved so far is $\sim$ 100 nm [117]. The energetic routes that lead to polymerisation have been shown to depend upon the material properties and experimental conditions. In the case of fs laser pulses, there is evidence to indicate the generation of free radicals primarily via avalanche ionization [118]. However, increasing the pulse duration to ps revealed a strong dependence of the linear or nonlinear absorption process on the laser repetition rate [119]. 2PP fabrication has been used over a wide range of biocompatible materials with properties conducive to medical device production such as microneedles, middle ear prostheses and scaffolds for tissue engineering and cell culture although the fabrication time is a known constraint in achieving the rapid manufacture of such devices [120].

2.5 DLW operating and parameter considerations

The aforementioned sections highlight the exceptional potential of DLW in fabricating monolithically integrated photonic and fluidic components with unprecedented flexibility in novel 3D architectures. Thus, making use of the fabrication advantages of DLW in developing novel optofluidic devices presents an exciting area of investigation. There are three integral requirements for a DLW fabrication setup. The first is a laser source capable of generating ultrashort pulses with pulse energies with a sufficient range to span over the homogeneous refractive index modification and the nanograting formation regimes for the desired material. The second requirement is that of an objective lens with a sufficiently long working distance to enable the focusing of the ultrashort pulses through the volume of the substrate of the desired material. Finally, the third requirement is that of a translation stage to enable the motion of the substrate through the laser beam focus along the three translation axes at the minimum. In addition to the minimum requirements stated above, there are a number of other parameters that can be appropriately tailored to influence the DLW fabrication. The aspects pertaining to these parameters are discussed in the following sub-sections. Figure 2.4 shows the DLW setup applied for the work undertaken in this thesis.

As shown in the figure 2.4, linearly polarised fs pulses at a central wavelength of 1047 $\pm$ 10 nm are generated from the variable repetition rate Yb-doped master oscillator power amplifier system (IMRA FCPA μJewel D400) featuring a variable blazed grating

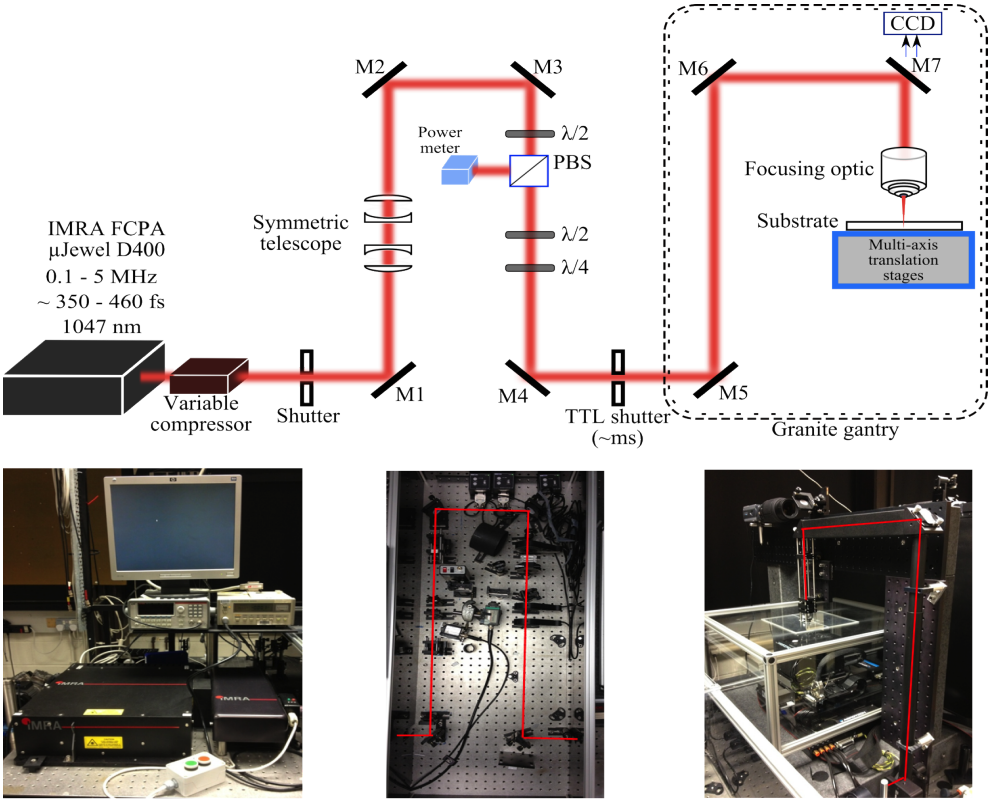

Figure 2.4: The DLW setup used for the work undertaken in this thesis. The basic optical path includes a symmetric telescope for beam collimation, power control ($\lambda/2$ plate), polarising beam splitter (PBS), a $\lambda/2$ plate and a $\lambda/4$ plate for polarisation control, a TTL shutter and a focusing optic. The granite gantry dampens any vibrations and provides stability to the setup.

based pulse compressor to control the duration of the pulses. The beam emanating from the compressor is collimated using a symmetric telescope arrangement and aligned using mirrors M1, M2 and M3 onto a half-waveplate ($\lambda/2$) and polarising beamsplitter (PBS) that are used for calibrated attenuation of the pulses. The polarisation state of the pulses is subsequently rotated using the second half-waveplate ($\lambda/2$) or changed to circular using the quarter-waveplate ($\lambda/4$) as required by the application. The pulses are then aligned to the back-aperture of the focusing optic using the mirrors M4, M5, M6, M7. The pulses are subsequently focused onto the substrate which is mounted on accurate multi-axis air-bearing stages (Aerotech, ABL 1000). The TTL shutter and the waveplates can be controlled using a computer during the writing process. The optical

path between the mirrors M1 and M7 is necessary to ensure there is sufficient space available to position an Acousto-Optic Modulator (AOM) for writing waveguide Bragg gratings, an autocorelator setup to measure the pulse duration and a beam expander whenever required without causing significant alterations in the setup. In addition, the height between mirrors M5 and M6 is required to complement the space requirements for the air-bearing stages. Figure 2.4 also shows the photographs of the DLW system.

2.5.1 Optical pulse parameters

Pulse duration

As discussed in section 2.2.3, pulse duration plays a critical role in the mechanism of energy transfer from the optical pulse to the material lattice. Selection of appropriate pulse duration is closely related with the nonlinearity of the material being irradiated as well as its physical properties. For materials with a nonlinear index (n_2) similar to that of fused silica, pulse duration $\sim$ few hundred fs is ideal to produce both homogeneous refractive index modifications or nanogratings. In these materials, extending the pulse duration to a few ps would result in a shift in the observed modification regime towards damage. In sharp contrast, materials with higher n_2 values exhibit nonlinear effects such as self-focusing and filamentation, that prevent fs pulses from focusing to a diffraction limited spot. In such materials, longer pulse durations $\sim$ 1 ps are necessary to counteract these undesired nonlinear effects [121]. Furthermore, DLW optical waveguides in borosilicate glass exhibited virtually no deviations in propagation losses or mode size when the pulse duration is varied [122], which is in sharp contrast to the behaviour observed in fused silica where the loss and modal characteristics were found to be strongly dependent on variations in pulse duration [123].

Pulse energy

A discussion based on effects of varying the energy of incident fs laser pulses in fused silica was given in section 2.3. The choice of pulse energy is also dependent on the material's physical properties. In crystalline materials, for example, fs pulse induced refractive index modification typically involves much lower pulse energies compared to fused silica. Use of higher pulse energies in these materials results in catastrophic damage. The application of fs laser pulses in Nd:YAG crystals is discussed in detail

in chapter 5.

Pulse polarisation

The polarisation of incident fs laser pulses plays a key role in determining the efficiency with which optical energy is absorbed by the material. In the refractive index modification regime, polarisation is an important parameter that determines the propagation losses that occur during the transmission of light through DLW optical waveguides [124]. In the nanograting formation regime, the pulse polarisation orientation with respect to the translation direction of the substrate determines the alignment of the nanogratings and hence the rate of their chemical etching, as discussed in section 2.7.

Pulse wavelength

The nonlinear absorption and photoionisation processes depend upon the frequency of the incident optical pulses, and therefore on the pulse wavelength (λ). In addition, the diffraction limited focus spot size is also linearly dependent on λ. Optical waveguides have been observed to exhibit marked variations in propagation losses when written using λ values 522 nm apart [125].

Pulse repetition rate

The pulse repetition rate plays a crucial role in determining the cross-section of a DLW optical waveguide [107]. The repetition rate determines whether there is enough time available for the energised material in the focal volume to cool down between successive pulses. For repetition rates below 100 kHz, the material that has absorbed energy from an incident optical pulse has enough time to cool down before the arrival of the next pulse. The sub-100 kHz range of repetition rate is termed as the single-pulse regime. In this regime, the spatial distribution of the laser modified region can be very closely approximated to the volume of the free electron plasma created at the end of each pulse energy absorption. As the material cools down before the arrival of the succeeding pulse, thermal effects outside the focal volume are negligibly small. The range of repetition rates between 100 kHz and 5 MHz is termed as the intermediate regime and beyond 5 MHz, the cumulative regime. In the intermediate and cumulative regimes, the hot material in the focal volume does not have sufficient time to dissipate. This results in accumulation of heat within the focal volume that is augmented with the

arrival of subsequent pulses. The material undergoes melting and the molten volume keeps increasing as long as the optical pulses arrive, thereby increasing the effective laser modified region. Therefore, thermal accumulation and diffusion play a dominant role in determining the spatial extent of the laser modified regions of the material [107]. Excellent optical waveguides have been achieved in different materials using the single [126, 127] and intermediate pulse regime [128].

Pulse front tilt

The pulse front tilt, which originates from angular dispersion of broadband ultrashort pulses, can be interpreted as the variation in the arrival time of an ultrashort pulse across the beam profile. Varying the direction of the pulse front tilt has been shown to induce a translation direction dependence for material modification in fused silica. This phenomenon has been termed as the quill effect [129].

2.5.2 Exposure conditions

Focusing optics

The focusing optics in a DLW fabrication setup typically consists of an objective lens. Typically, the numerical aperture (NA) of the lens can be carefully selected to achieve the desired feature size of the modified region within the material. Assuming a collimated, Gaussian beam profile is incident at the back aperture of the objective and the absence of aberrations and nonlinear effects, the spot size ($\mathsf{R_{sp}}$) of the focused fs laser pulses within a transparent dielectric material can written as $\mathsf{R_{sp}} = 2w_o$, where w_o is the beam waist radius. The dimension of the spot size along the direction of propagation of the beam can be determined by evaluating the confocal parameter (β). The diffraction-limited beam waist radius and the confocal parameter can be expressed as shown in equations 2.4 [105] and 2.5 [105] respectively.

$$w_o = \frac{M^2\lambda}{\pi(NA)^2} \tag{2.4}$$

$$\beta = \frac{M^2 n_{eff}\lambda}{\pi(NA)^2} \tag{2.5}$$

where, M^2 is the beam quality of the Gaussian beam and λ is the free space wavelength, n_{eff} is the effective refractive index of the material and NA is the numerical aperture of the focusing optic.
In the single pulse regime, the above parameters at the beam focus can be approximated to be the dimensions of the fs laser pulse modified region of the material. The presence of aberrations in the lens, however, can add various levels of complexity to the above approximation. Aspheric objective lenses or multiple-lens objectives can be used to circumvent this issue. As the pulses typically propagate through air before encountering the material surface while being focused, further aberrations are introduced due to the mismatch in refractive index at the interface of air and the material. These aberrations increase with the depth [130] and are especially significant when high NA objectives are used, wherein index matching oils can be used to minimise the aberrations.

Writing geometry
There are two writing geometries that can be applied for DLW fabrication. Translating the substrate along the direction of propagation of the laser beam is termed as the longitudinal writing geometry, while translating the substrate perpendicular to the beam propagation direction constitutes the transverse writing geometry. The writing geometry determines the cross-section of the laser written structures. Structures and waveguides written using the longitudinal geometry, exhibit a symmetric cross-section that scales with the circular symmetry of the incident Gaussian beam profile. However, the length of structures that can be achieved using this writing geometry are limited by the working distance of the focusing objective. In addition, the structures, especially optical waveguides, are adversely affected by aberrations that vary with distance as the focus position is changed. The transverse writing geometry is not limited by the working distance of the objective, although the cross-section obtained in the single pulse regime is asymmetric as the confocal parameter is longer than the beam waist. Methods to control the cross-section of laser written structures are described in section 2.6.2.

Translation speed
The speed with which the substrate is translated through the fs laser beam focus determines the level of overlap between the pulses. The overlap can be considered to be

the beam area overlap ratio between two consecutive laser pulses. The pulse overlap is also dependent upon the repetition rate regime. In the case of low and intermediate regimes, suitable translation speeds can be identified corresponding to the repetition rate to obtain an optimised pulse overlap to fabricate repeatable structures and waveguides. At the cumulative regime however, thermal accumulation and diffusion effects make it difficult to obtain optimised pulse overlap.

2.6 Waveguide characterisation and optimisation strategies

Since the first demonstration of optical waveguiding [83] and selective chemical etching [84] in fused silica, a substantial body of knowledge has already been created pertaining to the characterisation and optimisation of these unconnected but integrable phenomena. Besides fused silica, the extensive work undertaken in both these aspects extended to a variety of other materials. This section discusses the contemporary methods of characterisation and optimisation of DLW optical waveguides and selectively etched structures, some of which have been applied in the work undertaken in this thesis.

2.6.1 Material based studies in DLW optical waveguides

The performance of photonic applications developed using DLW depend upon well-optimised refractive index modifications in the substrate material. Optical waveguides that rely on refractive index modification using the low and intermediate repetition rate regime are typically termed as *Type I* waveguides [131]. Light can also be confined between two lines of damage written using higher pulse energies or longer pulse durations depending upon the material, these are commonly referred to as *Type II* waveguides [127]. Both *Type I* and *Type II* waveguides can, in principle, be written using longitudinal writing geometry, however, most demonstrations have applied the transverse writing geometry to fabricate the waveguides due to obvious advantages associated. Various characterisation methods have been applied in order to understand how these waveguides are formed from focused ultrashort pulses as discussed below.

A number of characterisation methods have been utilised to achieve a better understanding of the mechanisms leading to change in refractive index. These studies have typically involved the application of methods such as confocal microscopy and Raman spectroscopy to understand the physical changes that the material undergoes after being modified due to its interaction with fs laser pulses [132]. Fluorescence techniques have enabled the identification of an increase in defects or colour centres that may arise post-modification. In particular, fluorescence and photoluminescence studies have revealed an increase in a variety of defects in fused silica as a result of fs pulse irradiation [133]. Raman spectroscopic methods enable a detailed analysis of the structure of a dielectric material and is an ideal technique to detect and characterise changes in the material lattice post-modification. These structural changes can subsequently be identified with specific contributing factors such as lattice defects and lattice strain-fields, which have been successfully applied in characterising structural modifications in dielectric crystals [134, 135]. These spectroscopic methods can also be applied in imaging mode to create a visual representation of the spectroscopic analysis with high precision. Confocal microscope enabled spectroscopic analyses has been applied to locally explore the fs modified regions with micrometre accuracy and map the spatial extent of structural modifications that result from fs pulse irradiation from both surface as well as embedded modified regions. In addition to spectroscopic methods, the real-time microscopic imaging of the dynamical processes that occur during plasma formation and decay can provide useful insights into the spatial and temporal nature of the the energy transfer processes. Ultrafast imaging techniques have enabled the correlation between the transient plasma volume and change in refractive index [132] as well as identify possible methods of energy dissipation which contribute to reduction in spatial quality of the modified regions. This method can be applied to the real-time optimisation of DLW fabricated features.

2.6.2 Optimisation strategies for DLW optical waveguides

The cross-section of an optical waveguide determines its modal characteristics, *i.e.* the number of transverse modes that the waveguide supports, how well it confines light during transmission, and how well it couples light to external fibres. Poor light con-

finement resulting from weak refractive index contrast between the waveguide and the bulk material can lead to increased propagation losses. Asymmetries in the waveguide cross-section can limit its capability to guide unpolarised light. In addition, mismatch between the cross-section of a waveguide and the core diameter of standard optical fibres can lead to undesired coupling losses. It is therefore, important to apply methods to optimise waveguide fabrication and minimise asymmetries in the waveguide cross-section that can have adverse effects in the waveguide performance, especially when using the transverse writing geometry. In this geometry, the use of focusing objectives with $NA \approx n_{eff}$ can lower the asymmetry in the focus spot size and hence the modified region, however the cross-section becomes greatly reduced compared to standard optical fibre cores. Coupling light into these small cross-sectioned waveguides becomes more difficult. Engineering the cross-section of DLW optical waveguides has been successful in obtaining low-loss waveguides in various materials using low NA focusing optics. The methods developed can be broadly categorised into two general approaches. The first approach involves methods that allow the engineering of the laser beam before it is focused into the substrate material. These methods include the use of cylindrical telescopes, slits and adaptive optics to introduce an astigmatism in the beam. The second approach involves the multiscan technique, which is applied to engineer the morphology of the waveguide after the laser beam is focused into the substrate. The methods for both approaches are discussed below in chronological order.

The astigmatic beam shaping method

This method is applied in the transverse writing geometry and is based on the introduction of an astigmatism in the beam by positioning a cylindrical telescope between the fs laser and the focusing optics [136, 137]. This optical arrangement is shown in figure 2.5. Assuming the laser beam is propagating along the z axis, the substrate is placed on the $x-y$ plane and the translation direction is along the x axis the astigmatism, which causes different focusing conditions along the $x-$ and $y-$ axes, can be tuned to ensure tighter focusing of the spot in the plane orthogonal to the translation direction *i.e.* the $x-z$ plane and reducing the Rayleigh range of the focus in this plane. Therefore, in the $x-z$ plane, the rapid divergence of the beam reduces its depth of focus thereby causing a reduction in the dimension of the waveguide along the $z-$ axis. This minimises the asymmetry and allows the cross-section of the waveguide to be

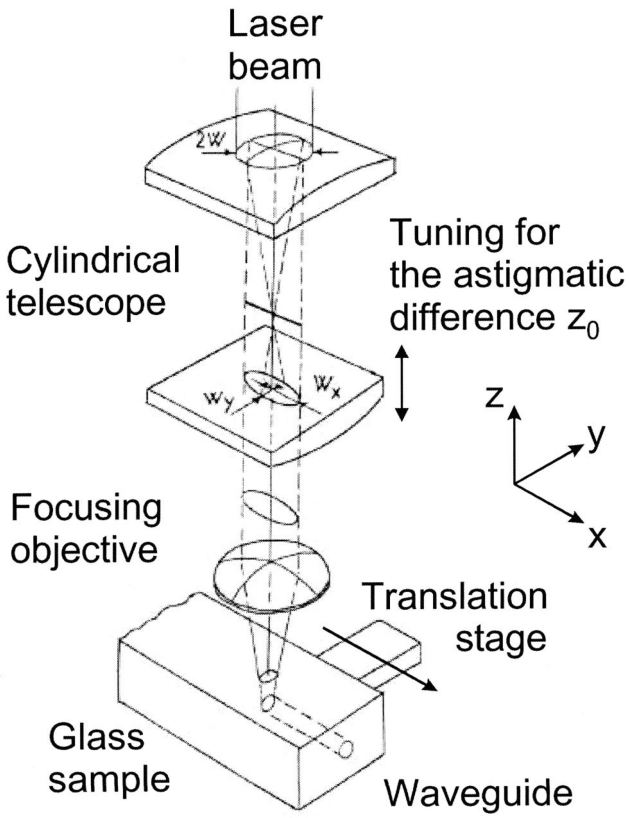

Figure 2.5: Schematic illustration for the astigmatic beam shaping technique [136]

nearly circular. The size of the focus in the $y-$axis can be independently controlled to determine the width of the waveguide in the $y-$axis. Moreover, the cylindrical telescope can be adjusted to optimise the astigmatic difference in accordance with the desired cross-section. However, this method has limited functionality in the case of curved waveguides as it allows the cross-section asymmetry correction to be applied along a single predetermined direction only.

The slit beam shaping method

This technique is an advancement of the original idea behind the astigmatic beam shaping method. It involves the positioning of a slit immediately before the focusing optic [138, 139]. Considering the same axes as mentioned in the astigmatic beam shaping technique, the beam waist along the $x-$ and $y-$ axis depends upon the NA of the focusing optic in the respective axes. Therefore, by maintaining the orientation of the

slit along the translation direction, the beam waist value along the direction orthogonal to the translation can be minimised. This method, when first demonstrated for shaping waveguides [139], presented an elegant alternative to the cylindrical telescope requirement to introduce astigmatism in the fs laser beam. A primary requirement for the slit technique to work is that the laser beam should fill the back aperture of the focusing optic completely along the axis of translation and partially in the orthogonal direction. Along the translation direction, the optical energy distribution is much more symmetrical compared to the case in the absence of the slit. This minimises the asymmetry in the cross-section. This technique is also limited in its applicability in curved waveguides in the same way as the astigmatic beam shaping method. Nonetheless, both the astigmatic beam shaping and slit based techniques lay the groundwork for using beam shaping methods to control the cross-section of fs laser modified regions within dielectric materials.

Adaptive optics enabled beam shaping

This technique applies computer controlled adaptive optical elements before the focusing optic as a means to minimise cross-section asymmetry. The first demonstration of this technique involved the use of a deformable mirror intended to replicate the use of a slit before the focusing objective [140], but with the advantage of dynamical wavefront shaping and aberration corrections typically associated with adaptive optics. The working principle of the technique is essentially the same as the slit based beam shaping method. Excellent asymmetry correction for the DLW optical waveguides was achieved which also exhibited low-loss waveguiding properties. Other adaptive optical elements such as Spatial Light Modulators (SLM) have also been applied for beam shaping by regulating the astigmatism in the fs laser beam wavefront [141].

In this case the requirement for the beam to elliptically fill the back aperture of the objective was controlled by simply varying the distance between the SLM and the objective using an arrangement of mirrors. In a recent advancement of this technique, the slit beam shaping method was combined with a SLM and a diffraction grating [142]. The experimental arrangement for this technique is shown in figure 2.6. The grating was applied across the SLM and its shape determined the slit aperture. The zeroth order of the diffracted beam was blocked and the first order was imaged onto the back focal plane of the focusing optic. The cross-section symmetries achieved using the SLM were found

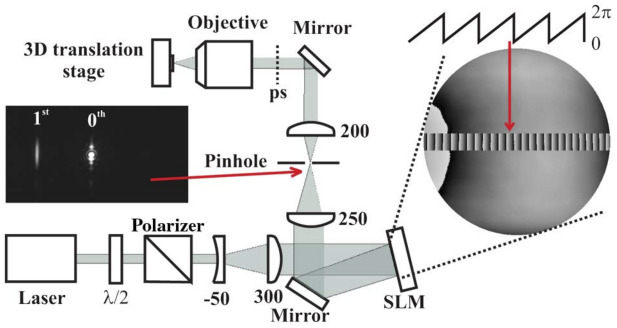

Figure 2.6: Schematic illustration for the adaptive optics enabled beam shaping technique. A regeneratively amplified titanium sapphire laser produced 100 fs pulses at 1 kHz at $\lambda = 790$ nm. The output was attenuated using a rotatable half-wave plate and a polariser and expanded onto a reflective LC phase-only SLM. The diffracted beam from the SLM was mapped onto the back focal plane of the objective using two achromatic doublet lenses. A pinhole on an adjustable mount was inserted into the Fourier plane of the SLM. The beam was adjusted to completely illuminate the back aperture of the (20×) 0.5 NA objective. The inset shows an example beam pattern from the SLM. [142]

to be comparable with those achieved using a physical slit. The waveguides exhibit near circular cross-section and were further investigated for the uniformity in refractive index change using Third Harmonic Generation (THG) microscopy. Furthermore, the waveguides were found to possess excellent guiding properties.

The adaptive optics based approach can potentially circumvent the curved waveguide limitation, by dynamically controlling the phase and amplitude across the profile of the incident laser beam in sync with the translational requirements. The work done by Salter *et al.* in ref. [142] is an important step forward in this regard as the method demonstrated can potentially be applied to adjust the writing beam intensity, the slit orientation and width as well as the effective NA of the objective lens dynamically during fabrication.

Besides the aforementioned methods, a relatively new technique was recently introduced which combines the slit beam shaping technique with temporal focusing of the pulses. Termed as spatio-temporal focusing, this method was demonstrated in the fabrication of DLW microchannels with promising implications as it allows the control of the Rayleigh range and the beam waist of the focus independent of one another. Although it is yet to be implemented in DLW optical waveguide fabrication, spatio-

temporal focusing has the potential to address some of the limitations of the cylindrical telescope and physical slit approaches in a much simpler and a more economical manner compared to the use of adaptive optics.

The multiscan method of waveguide engineering

The multiscan method involves an entirely different approach to correct waveguide

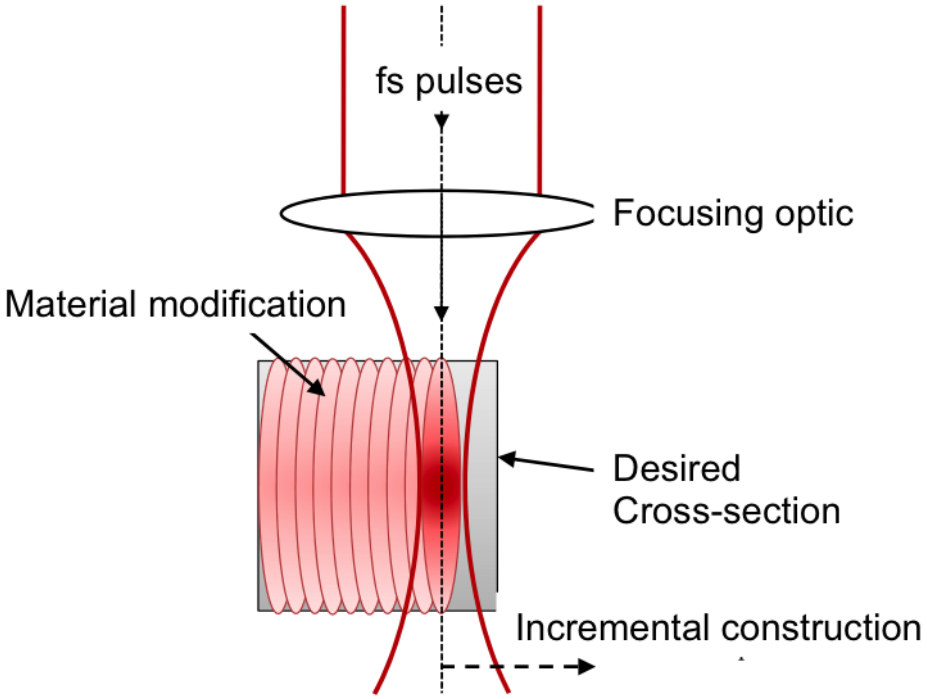

Figure 2.7: Schematic diagram showing the multiscan technique for waveguide engineering

cross-section asymmetry from the beam shaping methods discussed above. First demonstrated in 2005 [143], the method involves the translation of the substrate through the laser beam focus in the transverse writing geometry by taking advantage of the existing asymmetry in a rotationally symmetric Gaussian beam focus. The desired waveguide cross-section is achieved by an initial translation of the substrate in the desired axis to create the first asymmetric scan. The substrate is then shifted by a short 'offset' length along an axis perpendicular to the initial translation and beam propagation axes followed by another scan along the desired translation axis. The process is re-

peated with multiple offsets until the desired symmetric waveguide cross-section is achieved. The multiscan waveguide engineering method is illustrated in figure 2.7. This method allows the engineering of the waveguide cross-section with much more flexibility in comparison with the beam shaping methods, although constructing the cross-section from a single scan is a relatively longer process. In addition, the multiscan engineered waveguide cross-section is approximately the shape of a square, unlike the near-circular cross-sections achieved by using the beam shaping methods. The dimension of the waveguide along the laser beam propagation direction is determined by the confocal parameter, whereas the orthogonal dimension is determined by number of offset movements. As there is appreciable overlap between the adjacent scans, the required pulse energy to achieve refractive index modification from a single scan is lowered. Therefore, this method can be extended to materials where the material modification energy threshold is close to the material damage energy threshold. The multiscan technique provides excellent precision and flexibility and is well-suited for the fabrication of curved waveguides. In addition, the method decouples the size of the modified cross-section from the pulse parameters such as pulse energy, repetition rate, and NA of the lens [144]. These advantages underpin the extensive application of this technique in a variety of materials including passive and rare-earth doped glasses and crystals [107]. The multiscan technique is also useful to fabricate microfluidic features intended for selective chemical etching. In chapter 3 and chapter 5 of this thesis, the multiscan technique has been applied in fabricating DLW microfluidic channels, while its application in optical waveguide fabrication is presented in chapter 4.

DLW has been applied in the fabrication of optical waveguides and waveguide enabled photonic devices extensively since the advent of the technology. Waveguides have been written and characterised in a wide variety of materials using parameters in both the single pulse and the intermediate regimes. Passive glasses, such as fused silica [83], borosilicate glass, fluoride glass and chalcogenide glass [145] were the earliest materials where DLW waveguides were reported with excellent guiding properties using the multiscan technique [143]. In the refractive index modification regime, low-loss *Type I* passive waveguides have also been reported in silicate and phosphate glasses which are suitable hosts for rare earth dopants such as erbium (Er) and ytterbium (Yb) enabling active waveguide applications [146, 147]. Excellent active waveguides in bismuth based materials have also been reported which have been applied to de-

velop compact modelocked waveguide lasers [148, 149]. DLW waveguides have also been fabricated in undoped and chromium (Cr^{2+}) doped polycrystalline zinc selenide ($ZnSe$), for applications in the near-infrared (NIR) and mid-infrared (MIR) regions of the electromagnetic spectrum [121, 150]. Furthermore, *Type II* waveguides have been demonstrated in crystalline materials such as lithium niobate ($LiNbO_3$) [131] and rare-earth doped yttrium aluminium garnet (YAG) crystals [135, 151]. In addition to active waveguide applications, DLW has also been extensively applied in the development of microphotonic circuits such as Y-junctions [152], directional couplers for visible [153] and telecommunication wavelengths [154], Mach-Zehnder Interferometers (MZI) [155], fanout devices [156], photonic lanterns [157], waveguide Bragg grating sensors [144], evanescent waveguide sensors [158] and quantum optics [159].

The applications highlighted above underscore the capabilities of DLW as a maskless, flexible technique for active waveguide applications and integrated passive photonic applications in both 2D and 3D architectures. However, the refractive index change achieved in the core of DLW waveguides, which is typically $\sim 0.5\%$, is a relatively low increase when compared to the core-cladding index contrast in single-mode optical fibres, which results in comparatively higher propagation losses. There is scope for improvement of the refractive index contrast in DLW waveguides. A relatively unexplored area is the application of non-diffracting beams in DLW of optical waveguides. The application of Bessel beams instead of laser beams with a Gaussian profile have been recently reported in the fabrication of waveguide in the longitudinal writing geometry [160], which opens yet another avenue for development of the technology.

2.7 DLW enabled selective chemical etching

In the nanograting regime of material modification, which is discussed in section 2.3.2 with respect to fused silica, the unique nano-sized features enable an increase in the chemical etching selectivity of the laser irradiated regions. This phenomenon was first demonstrated in 2001 [84], where direct 3D microfabrication inside a volume of a fused silica substrate was carried out in two steps. First, the desired structures were first written inside the volume of the material using focused fs laser pulses at a wavelength of 795 nm and a pulse repetition rate of 1 kHz. The pulse duration was ≈ 120 fs (FWHM). The pulses were focused into the material using an oil immersion $\times 100$

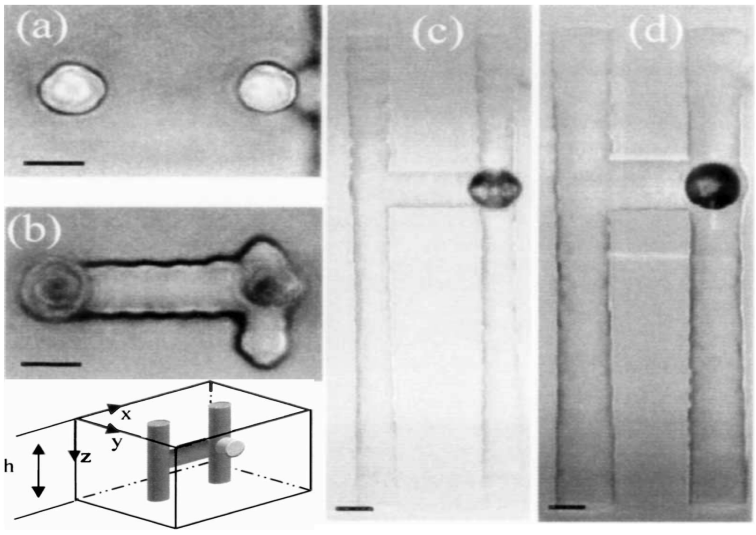

Figure 2.8: Optical transmission microscopy images showing selectively etched regions in fused silica after 2 h of etching in an aqueous solution of HF acid: (a) top view of the plane $x-y$ of the beam entrance, (b) top view of the horizontal channel at a depth of 30 μm, (c) side view ($y-z$ plane) showing the etched 3D pattern, (d) side view of the etched 3D pattern after 3 hours of etching in HF acid. The inset shows a schematic of the 3D design. The beam propagated along the z axis. The scale bar is 7 μm.[84]

objective with an NA of 1.30. Second, the substrate with the laser written 3D design shown in figure 2.8, was immersed in an aqueous solution of hydrofluoric acid (HF) at 5% dilution under ambient conditions for 3 hours. Post-etch, it was found that the laser irradiated regions dissolved significantly faster than the unmodified regions of the substrate, thus creating the possibility to form embedded microfluidic channels using DLW.

In the years that followed, a number of studies pertaining to the characterisation of the etching process were reported. A method suitable for the manufacture of microfluidic channels with arbitrary shape and dimension in fused silica substrates was reported [161] using the aforementioned two-step procedure. Important conclusions drawn from this work included the observation that etching is significantly faster in the central portion of the laser track, where a selectivity of 1:100 was evaluated with respect to the unmodified regions. Refractive index profilometry measurements revealed that the spatial extent of laser affected zone in term of etching selectivity can extend over a distance that is several times larger than the laser track depending upon energy of the

incident fs pulses. A phenomenological proposal accounting for the increase in etching selectivity was also put forward with the argument that there exists two distinct pulse energy regimes that affect the etch quality. Figure 2.9 shows the variation of etch quality with pulse energy as reported by Bellouard *et al.* in ref. [161].

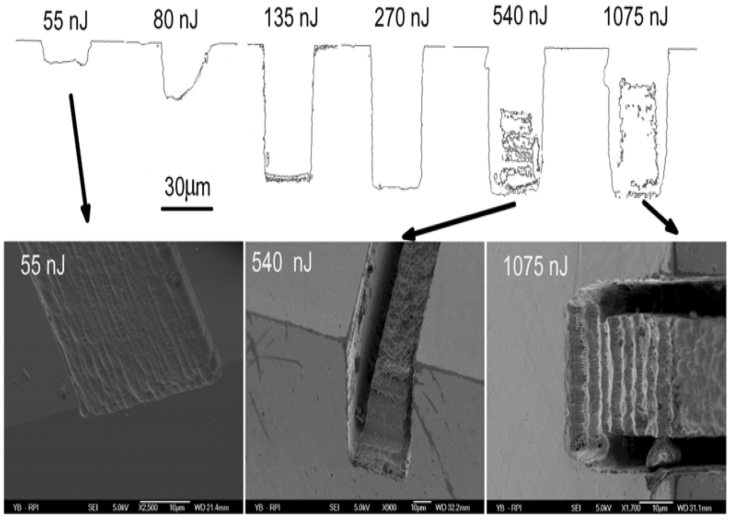

Figure 2.9: Profiles of post-etch structures showing variation of etch quality with incident pulse energy. Scanning Electron Micrograph images showing partially etched structures at three different pulse energies used: from left to right: 55 nJ (top view), 540 nJ and 1075 nJ. The number of scans to build the structures was identical for all three channels. [161]

For pulse energies $< 270\ nJ$, increased etching was observed which was attributed to the reduction of the Si–O–Si bond angle within the focal volume. Furthermore, it was proposed that the compaction in volume in the structural network induces internal stress that relaxes over range of a $\mu\ m$. In the case of pulse energies $> 270\ nJ$, material ablation becomes dominant introducing porosity into the material. The porosity aids the stress relaxation process when adjacent modified regions are written. Therefore, the structural change induced at higher pulse energies is less favourable to etching. The etch rate of fs laser modified silica structures has been shown to be approximately linearly dependent on the induced index of refraction change, for index changes of up to 1 % [162]. The chemical reaction that occurs during the etching process is given as:

$$SiO_2 + 4HF \rightarrow SiF_4 + 2H_2O \tag{2.6}$$

In a seminal work undertaken to investigate methods to control the etching of laser modified structures, the dramatic dependence of the etch rate on the laser polarisation was reported [163], where the etching selectivity exhibited a variation spanning 2 orders of magnitude depending upon the polarisation used for the laser beam. Furthermore, the existence of an energy–per–pulse threshold was determined at which etching of the laser-modified zones becomes highly polarisation selective. This experiment was performed by focusing 40 fs pulses in fused silica from a regeneratively amplified Ti:Sapphire laser system with λ=800 nm and 100 kHz repetition rate.

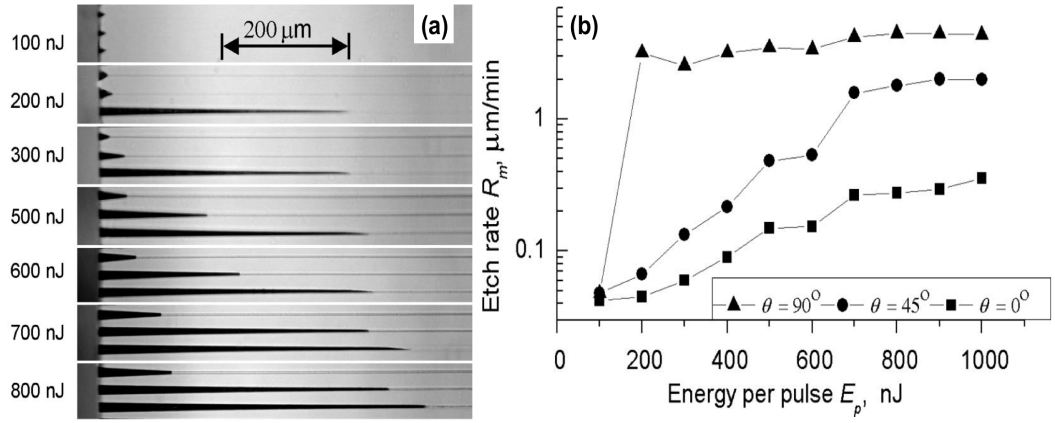

Figure 2.10: The polarisation selective etching in fused silica. (a) For each pulse energy, three polarisations have been used. The bottom scan in each pulse energy is when the electric field vector ($\overrightarrow{E}$) of the incident pulse is at 90^o with the translation vector ($\overrightarrow{v}$). The middle scan for each pulse energy is the case when $\overrightarrow{E}$ and $\overrightarrow{v}$ are at 45^o and finally the top scan for each pulse energy is the case when $\overrightarrow{E}$ and $\overrightarrow{v}$ are at 0^o (b) Plot showing variation of etch rate ($\frac{\mu m}{min}$) with incident pulse energy (nJ). The onset of etching selectivity can be observed. [163]

The laser beam was spatially filtered and focused using a 0.65 NA focusing optic at a depth of 100 μm below the top surface of the fused silica substrate. The angle between the electric field vector of the linearly polarised output laser beam ($\overrightarrow{E}$) and the writing direction $\overrightarrow{v}$ was varied using a zero-order half-wave plate. The pulse energy was controlled using a variable attenuator from 50 to 1000 nJ. It was shown that the etch rate of the modified material increased by up to 2 orders of magnitude simply by rotating the inscription beam polarisation under the specified writing conditions. Figure 2.10 shows the polarisation selective etching in fused silica observed in [163].

An explanation of the phenomenon is that the polarisation sensitivity is caused by the formation of periodic nanogratings inside the fs laser irradiated regions. The orientation of the nanogratings with respect to the acid flow direction determines the etch rate of the modified structure. The grating-like pattern of nano-sized planes was found to be oriented perpendicular to $\overrightarrow{E}$ implying that their orientation could be altered simply by rotating the polarisation of the beam. Figure 2.11 shows the orientation of the nanogratings with respect to the polarisation of the incident fs pulses.

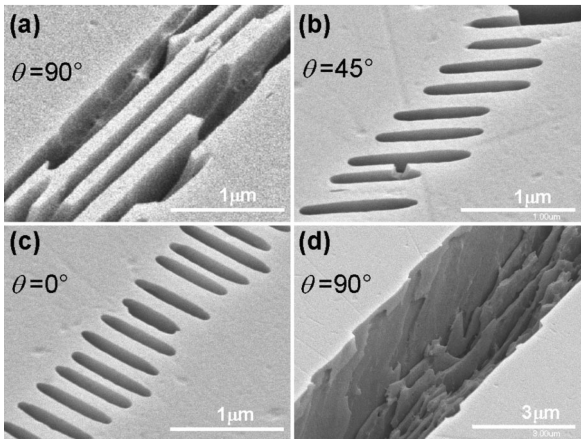

Figure 2.11: The nanograting patterns are orientated perpendicular to the polarisation of fs laser pulses at a pulse energy of 300 nJ The angle θ between $\overrightarrow{E}$ which represents the electric field vector of the incident pulses and $\overrightarrow{v}$ which represents the translation direction (a) Nanograting orientation when $\theta = 90^o$ (b) Nanograting orientation when $\theta = 45^o$ (c) Nanograting orientation when $\theta = 0^o$ (d) A fully etched structure for the case when $\theta = 90^o$. The structures were revealed after 20 min of etching in a 0.5% aqueous solution of HF.[163]

When the nanogratings are oriented perpendicular to the translation direction ($\overrightarrow{E} \perp \overrightarrow{v}$), the HF acid encounters unmodified silica in its path, which reduces the cumulative etch rate. However, when the nanograting planes are aligned along the translation direction ($\overrightarrow{E} \parallel \overrightarrow{v}$) it is much easier for the acid to ingress into the modified material. Etching in both cases can occur simultaneously but with a significant difference in rate. Gaseous HF and and hydrofluoric acid and ammonium fluoride ($HF : NH_4F$) buffer solutions have also been applied to etch DLW structures [164].

A distinctive issue with HF is over-etching, where DLW structures written closer to the facet of the substrate etch more than those deeply embedded within its volume

and consequently lose their designed aspect ratio. As an example, in the case of a single scan directly written within a substrate from one end facet to the other, HF etching exhibits a characteristic taper along the length of the etched scan. The scan, once completely etched, results in a cone shaped microchannel with a non-uniform cross-section along its length. This characteristic taper in the case of HF etching has to be accounted for during the design of an optofluidic device. However, the taper can be compensated for by designing an inversely tapered structure, which will provide a roughly uniform cross-section after being etched [165]. The compensation performed using a spiral inverse taper is shown in figure 2.12.

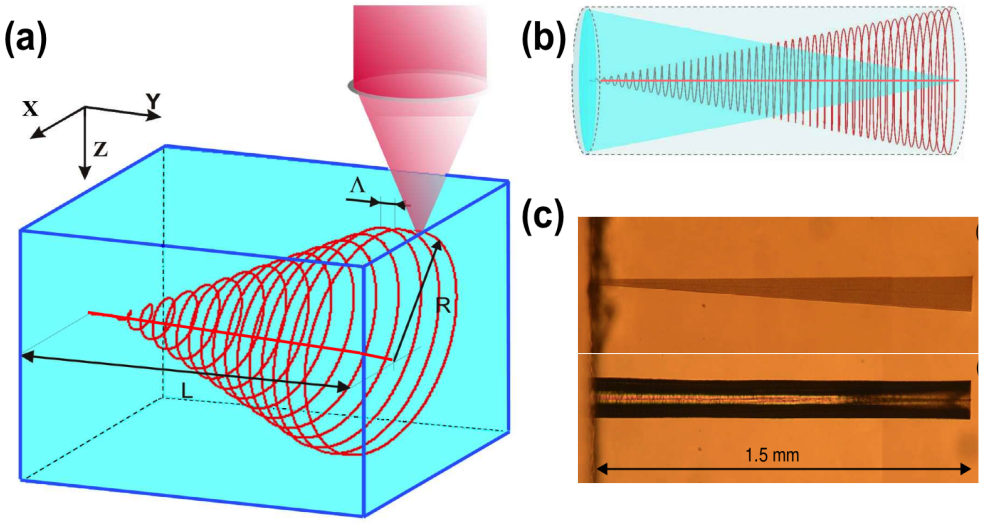

Figure 2.12: The method of taper compensation using a conical spiral with an inverse taper. (a) Schematic illustration showing the conical spiral in 3D. (b) Schematic illustration showing the tapered microchannel (blue), the compensating conical spiral (red) and the desired cylindrical microchannel (grey). (c) Optical microscope images comparing the DLW inverse taper with the final etched microchannel. HF acid ingress into the material from the left side of the microchannel.[165]

Aqueous solutions of KOH have recently been proposed as an alternative to HF for etching DLW structures. KOH has been applied at a concentration of 10 M and at an elevated temperature of 80 ^oC for the selective etching of pyrex [166] and silica based glasses [167]. The etch rate observed using KOH was much lower than the case of using HF, although the etched structures exhibited significantly higher selectivity and hence reduced taper. Microchannels as long as 10 mm with less than 60 μm

diameter were successfully fabricated after prolonged etching periods upto a maximum of 72 hours. Despite the long etch periods and elevated temperatures required the selectivity in the case of KOH etching is impressive, which indicates that after further optimisation trials, KOH can potentially be applied in DLW devices with stringent etching selectivity requirements.

2.8 DLW enabled optofluidic microsystems

To date, DLW optofluidic devices have been fabricated in two materials *viz.* fused silica and Foturan, which is a photosensitive glass. In chapter 5, this thesis presents the laser gain medium neodymium doped YAG, as yet another material where DLW optofluidic devices can potentially be developed. This section summarises some of the recent developments using fused silica as a substrate material for DLW integrated optofluidics.

The DLW technology provides the unmatched capability to fabricate photonic and fluidic components using the same method. An excellent example of this capability was demonstrated in the fabrication of an integrated dual beam optical trap [66]. The device translated the fibre based optical stretcher, first demonstrated by Guck *et al.* [64], into a monolithic, integrated environment. The device design involved two optical waveguides aligned exactly opposite to one another, each orthogonal to the microchannel located in between as shown in figure 2.13. Fabrication was performed using a single laser writing step, which ensured highly accurate alignment between the optical and fluidic components. The DLW step was performed by focusing 230 fs pulses through a 50 $\times$ (0.6 NA) focusing optic. The pulses were generated from a frequency- doubled cavity-dumped Yb:KYW laser operating at 600 kHz repetition rate. The microchannel was fabricated using 290 nJ pulses at a depth of 400 μm from the top surface of the substrate using a translational speed of 1 $mm\ s^{-1}$. Writing was performed using the second harmonic wavelength of the crystal which is 515 nm. The laser polarisation was set perpendicular to the microchannel axis. The waveguide was fabricated using a higher repetition rate of 1 MHz, a pulse energy of 100 nJ and translation speed of 0.5 $mm\ s^{-1}$ and exhibited single-mode guiding at 1 μm with a propagation loss of 0.9 dB/cm. The optical stretcher function of the device was applied to red blood cells (RBC) flowing through the microchannel which were stretched by

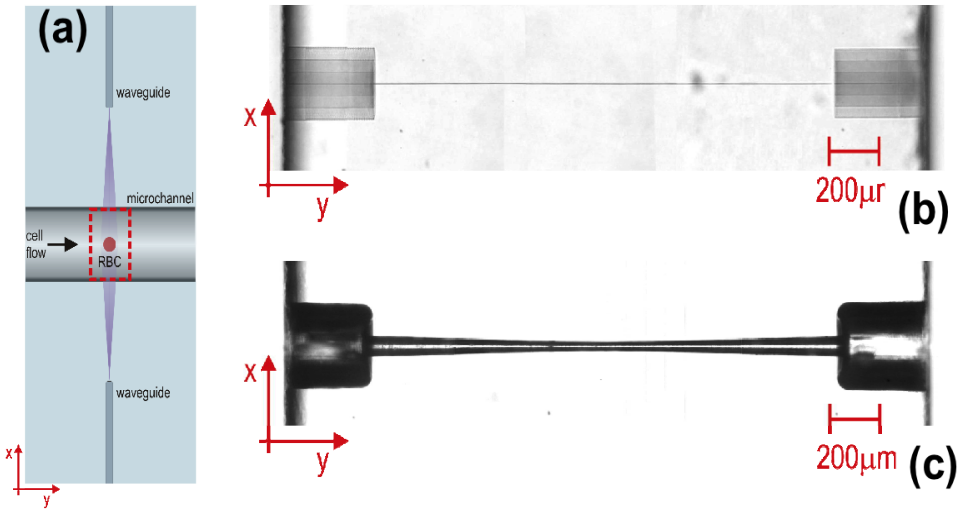

Figure 2.13: The DLW enabled dual beam optical stretcher design. (a) Schematic illustration showing the alignment of the optical waveguides with the microchannel. The dashed box represents the acquisition area of the CCD. (b) The laser written microfluidic channel showing two larger etched regions to enable the fluidic plumbing into the device. (c) The microchannels after being etched in 20 % HF for 4.5 hours. [66]

upto 25 % of their normal size. However, surface roughness caused by HF etching was recognised to be a limitation due to the formation of scattering centres in the microchannel, which may result in erroneous data when applied to optical stretching.

DLW has also been applied in flow cytometry applications. A fused silica based optofluidic device with integrated microchannels and optical waveguides was fabricated with an aim to detect single RBCs *via* two optical detection schemes [168]. The first scheme involved the recording of variations in transmission intensity of from a single RBC using a helium neon laser beam. The second scheme involved the measurement of fluorescence from labelled cells upon excitation by an Argon laser beam. The fabrication of the integrated optical waveguide and microfluidic structures consisted of an intermediate wet etching step between two laser writing steps. The desired microchannel design was first written using $\lessapprox 500\ fs$ pulses with a pulse energy of 140 nJ. The 1045 nm pulses were generated using a Yb-doped fibre-based fs laser (FCPA μJewel D-400, IMRA America, Inc.) and delivered at a repetition rate of 1 MHz. The translation speed used to fabricate the microchannel was 100 $\mu m\ s^{-1}$. Figure 2.14 shows the

experimental DLW setup and device design applied.

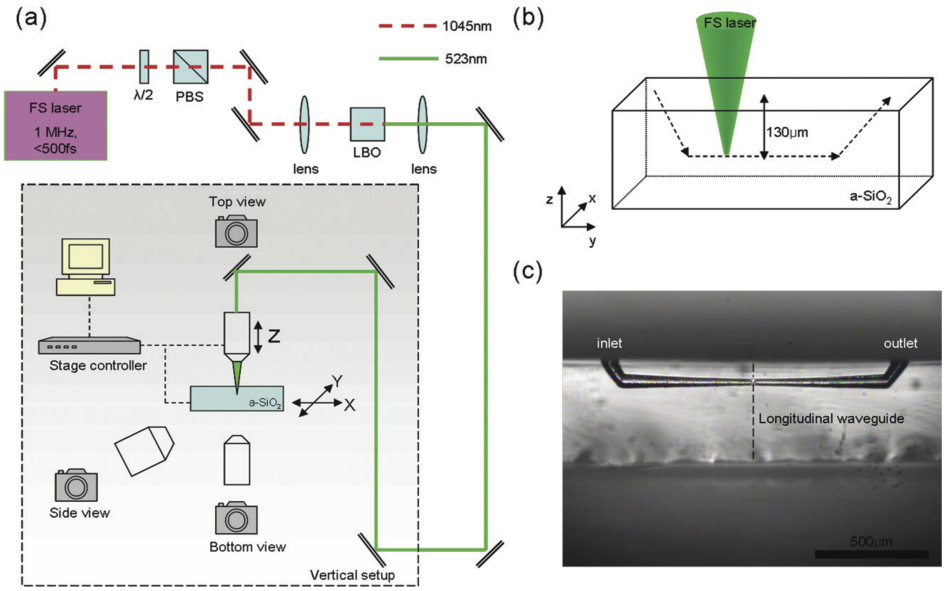

Figure 2.14: (a) Schematic illustration of the experimental setup of fs laser pulse irradiation on a fused silica sample (b) The laser scanning path for fabricating microchannels, (c) The optical transmission image of a fabricated microchannel. The dashed line represents the location where the integrated longitudinal waveguide was written. [168]

The microchannel was reported to have been etched using HF acid at $\sim$ 25 % dilution for 3 hours. In order to achieve accurate alignment, Kim *et al.* performed waveguide writing after the etching step [168]. The optical waveguides were written after the etching step in both a parallel as well as perpendicular orientation to the top surface of the fused silica substrate. The 3D microchannel design presented in this work provided an elegant method to take advantage of the intrinsic tapering phenomenon associated with HF etching. The tapering was tailored to focus the flow of cells at the waveguide interrogation region, thereby removing the requirement of using standard flow focusing methods. The device was reported to exhibit a counting rate of 23 cells per second using volumetric flow-rates of up to 0.5 $\mu L\ min^{-1}$. This DLW device offers an integrated and potentially economical alternative to address specialised requirements in cell sorting.

Waveguide enabled cell sorting is yet another elegant application of DLW optofluidic

capabilities where the monolithic integration of fluidics and optical waveguides have been achieved [169]. A fluorescence activated cell sorting device was fabricated in fused silica using the frequency doubled output from a 1040 nm regeneratively amplifier delivering $\sim$400 fs pulses. The repetition rate was set at 500 kHz. The laser beam was focused inside the fused silica substrate using a 50$\times$ 0.6 NA focusing optic. The usual two step process of laser writing and subsequent chemical etching was followed in this work. The microchannel was written using a second harmonic pulse energy of 700 nJ and a translation speed of 1 $mm\ s^{-1}$ at a depth of 400 μm below the substrate top surface. Etching was performed by immersing the laser modified fused silica substrate in a 20 % aqueous solution of HF at a slightly elevated temperature of 35 ^oC in an ultrasonic bath. The optical waveguides were written using 100 nJ pulses and a translation speed of 0.1 $mm\ s^{-1}$ and optimised for guiding at 1 μm. The device was designed to work with fluorescent as well as non-fluorescent samples. A continuous wave beam from a Yb fibre laser capable of generating 5 W optical power at 1070 nm was launched into a waveguide designated for use as a light source to exert radiation pressure on the particle to be sorted. On the other side of the chip, a 532 nm or 473 nm wavelength laser, depending upon the fluorophore excitation wavelength, was coupled to a waveguide designated to excite fluorescence when polystyrene fluorescent beads or fluorescent cells, respectively, flowed in the microchannels. Figure 2.15 shows the design of the device.

The detection of fluorescence was used as a signal to trigger the sorting waveguide which when turned on, exerted radiation pressure on the sample to enable its flow through a pre-determined microchannel arm. The device was capable of sorting a cell sample comprising human transformed fibroblasts transfected with a plasmid encoding the enhanced green fluorescent protein (eGFP).

The aforementioned applications of DLW enabled optofluidics are recently demonstrated examples of the technology where the complete integration of the optical waveguide and microfluidic is realised in a single chip. In addition to these examples, DLW optical waveguide enabled sensors such as MZI have also been fabricated in commercial microfluidic chips for label free sensing applications [170].

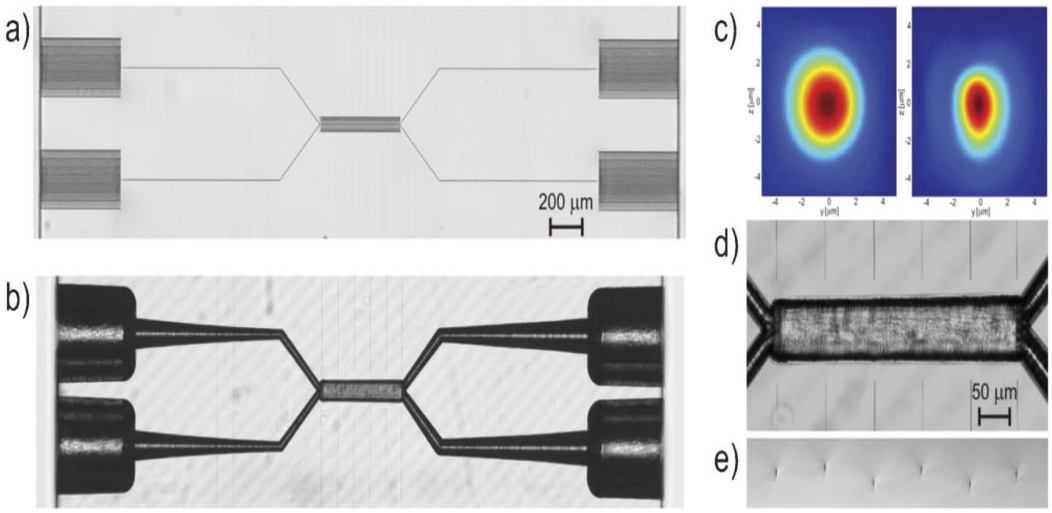

Figure 2.15: (a) Microscope image of the fs laser irradiation pattern to form the integrated optical sorter. (b) Same structure shown in (a) after 5 h of chemical etching in 20 % aqueous solution of HF; the central common branch is 0.5 mm long. (c) Intensity mode profile at 1 mm wavelength of (left) optical fibre and (right) femtosecond laser written waveguide. (d) Microscope image of the central common branch of the sorter after etching, with facing integrated optical waveguides. (e) Cross-sectional microscope image of fabricated waveguides at different depths.[169]

2.9 Conclusions

This chapter has described the underlying nonlinear processes that govern the DLW process. The regimes of material modification and their relation to the properties of the incident ultrashort pulses have been detailed. Furthermore, the parameter space concerning DLW is introduced and the manner in which these parameters affect the DLW process are discussed, both in terms of optical waveguide writing as well as microfluidic component fabrication. Some recent photonic applications enabled using DLW are presented. The selective etching capability of DLW is discussed with respect to the relevant material modification regime and methods to control the etching are detailed. Finally considerations of integrating the two processes are introduced and some recent demonstrations of integrated DLW optofluidic devices are outlined.

The concurrent fabrication capability offered by DLW underscores the position of the field as an exciting new addition to the traditionally used fabrication methods in optofluidic microsystems driven by advantages such as arbitrary 3D design freedom,

high-accuracy alignment, monolithic integration and rapid prototyping. In addition, fs laser direct writing is capable of altering the optical properties of a substrate to create a wide range of micro-optical components inside glass, including optical waveguides, Mach-Zehnder interferometers, and optical attenuators. DLW innovations will advance in synergy with advances in biological and biochemical analytics, motivated by new sensing requirements. The applicability of DLW to a wide range of applications is also underpinned by the fact that glass based substrates exhibit superior optical performance and chemical stability than polymers. In addition, the chemical etching capability can potentially be extended to other optically active materials, as presented in chapter 5 in this thesis. This creates the possibility of applying the well-characterised photonic capabilities of these materials in novel sensing schemes, thus opening new avenues in optofluidic biosensing. As a field that is still in its infancy, DLW is well positioned to generate innovations in design, fabrication and sensing schemes in optofluidic biosensing in the recent future.

Chapter 3

Deformability based label-free cell separation

Understanding cellular behaviour is fundamentally reliant on the unbiased interpretation of the cells' functional response to variations in exogenous or endogenous chemical as well as physical factors such as externally applied physical perturbations such as thermal gradients or electromagnetic fields. The response to such perturbations is typically studied using single live cells or cell populations. In both cases, an informative interpretation of cellular response is essentially statistical, as analysis is performed over a set of measurements that are typically either time-averaged for single cells or ensemble-averaged for a population of cells [171]. With respect to a population of cells, heterogeneity is an important factor to consider. A cell population is termed as heterogeneous if cell-to-cell differences exist that can manifest as functionally significant deviations from the population-averaged measurements [172]. This may lead to potentially anomalous interpretations of cellular behaviour and create a source of bias in biomedical implementations. In particular, with respect to therapeutic and diagnostic applications, sufficiently heterogeneous mammalian cell populations necessitates their efficient fractionation into populations with reduced heterogeneity [173]. Examples where reduced heterogeneity is essential include investigations into disease progression in cancer stem cells [174], the role of circulating tumour cells in metastasis [175], DNA methylation in white blood cells (WBC) [176] and the differentiation of human pluripotent stem cells (hPSC) [177]. In contrast to the above, cellular heterogeneity is

also known to contribute towards the proliferative potential of a cell population [172]. Therefore, understanding its complex role in cellular function and development is a key area of research in biology.

The objective of fractionating a heterogeneous population of cells into homogeneous sub-populations with uniform function and properties is ubiquitous. The advantages of fluid transport in miniaturised environments, as discussed in chapter 1, when applied in concurrence with known biological sensing methods creates a powerful tool to generate cell populations with reduced heterogeneity. This has motivated the widespread development of innovative cell separation and isolation strategies and their implementation as a crucial preparatory step in several applications ranging from diagnostics, drug discovery, therapeutics and, to an extent, in facilitating insights into the biological significance of heterogeneity [178]. For instance, the effective separation of T-lymphocytes from whole blood is key in diagnosing human immunodeficiency virus (HIV) cases [179], malarial diagnosis requires the separation of infected erythrocytes from uninfected ones [180] and neuronal cell separation is crucial to cell replacement therapy in neurodegenerative disorders such as Alzheimer's and Parkinson's disease [181].

This chapter presents a simple and effective approach to label-free cell separation that is based solely on dissimilarities in deformability between target cell populations. In particular, the separation mechanism presented here decouples cell deformability from cell size and shape and emphasises its application in successfully producing viable output cell populations. The chapter begins with a brief overview of cell separation methods using conventional and miniaturised systems in sections 3.1 and 3.2. Deformability as a mode of separation was discussed in chapter 1. The DLW device design and working principle is introduced in section 3.3.1. Sections 3.3.2 and 3.3.3 describe aspects relating to optimised fabrication of the device. Section 3.3.4 presents the device performance and section 3.4 discusses the future prospects of the DLW device presented in this chapter.

3.1 Traditional methods of sorting cells

Traditional methods of sorting cells can be broadly divided into three principal categories *viz.* adherence based, density based and antibody binding based methods [182].

Adherence and density based methods, although inexpensive, are time consuming batch processing methods that suffer from a lack of specificity, low cell purity and limited capability to isolate sub-populations of cells. On the contrary, continuous flow antibody binding based methods such as Fluorescence-Activated Cell Sorting (FACS) and Magnetic-Activated Cell Sorting (MACS) offer much higher throughput and specificity but are significantly more expensive. Both FACS and MACS methods make use of labelling of the cells of interest. The FACS method utilises fluorescent conjugated antibodies to label cells. The emitted fluorescence and scattered light data can reveal information regarding the cell-type, size and gene expression. Along with data acquisition, FACS systems can also be used to sort cells at impressive throughputs of $\sim 3 \times 10^4$ cells/second post identification [183]. The MACS method utilises magnetic beads with conjugated antibodies that bind to specific proteins on the target cells [184]. The flow of cells labelled with magnetic beads is sufficiently retarded in the presence of an external magnetic field and labelled cells are directed towards a collection well. MACS can be used in conjunction with FACS with comparable throughputs. The fact that both methods involve the use of conjugated antibodies to label cells is a limitation especially in cases when the labels can interfere with the functioning of the cells. FACS and MACS have both been implemented in miniaturised setting as discussed in section 3.2. Data generated from these macro-scale methods can be analysed statistically to obtain some important information about the existence of sub-populations within a heterogeneous sample. However, these methods make use of labelling steps to fractionate heterogeneous populations into sub-populations with desired homogeneity, which is likely to alter the characteristics of output cell populations.

3.2 Contemporary miniaturised label-free methods of sorting cells

In contrast to antibody labelling methods used in macroscopic sorting approaches, sorting strategies are rapidly progressing towards label-free methods that make use of intrinsic biophysical properties of cells as markers for separation. Examples of these markers include size, morphology, electrical polarisability and impedance, magnetic susceptibility, hydrodynamic properties and deformability [183]. The sorting strategies

can be broadly categorised into passive micro-component based methods and active field based methods.

Passive methods generally make use of micro-structured filters, several variants of which have been applied as a label-free sorting approach typically based on size or shape. Microstructures normally applied for separation involve weir, pillar, cross-flow and membranous sieves to achieve separation [185]. This approach is commonly applied for applications requiring the fractionation of blood into red blood cells, white blood cells, platelets, and plasma [183]. The fundamental mechanism is conceptually simple and involves periodic gaps between each microstructure to suit the cell size intended for separation. Size-based separation is limited in the case of populations with heterogeneity of cell sizes. In addition, clogging of the microstructures is also an issue. The use of sieves in particular, suffers from clogging by the cells, which can be circumvented by using cross flow designs, where the liquid flow in the microchannel is continuously extracted to the adjacent channels through micro-pores [183]. The microstructure approach can be implemented in 2D arrays [186] or in a continuous flow approach [187]. Hydrodynamic flow methods constitute another passive approach to cell sorting. This method involves the manipulation of flow either using a pinched region within a microchannel or around arrays of microstructures, such that particles or cells can be aligned in the flow stream along different loci with respect to size [188]. Particle manipulation using hydrodynamics has been applied with micro-pillar arrays enabling the continuous flow size based separation of particles using a principle known as deterministic lateral displacement, which involves manipulating the lateral displacement of particles or cells by designing the array as required [189].

Applied field based sorting strategies were developed as passive approaches purely based on size and shape proved insufficient for specific applications. Cells behave as polarisable dielectrics under the influence of an applied electric field. This forms the basis of the commonly applied dielectrophoresis (dEP) methods for cell separation. Depending on their dielectric properties, cells can experience a force along or opposite to the direction of the applied electric field leading to positive or negative dEP [190]. Electrodes can be incorporated within the micro-device in an alternating current (AC) as well as direct current (DC) configurations. Separation can be achieved either by segregating particles or cells based on the magnitude of the dEP force or by manipulating an AC frequency allowing particles or cells to experience positive dEP or

negative dEP depending upon their characteristics. Once a frequency is known where target particles or cells experience dEP opposite to the other cells or particles in the mixture, these can be forced to move in opposite directions to each other creating a separation [190]. Acoustics has also been applied as a separation strategy. Standing waves at ultrasonic frequencies enable particles or cells to experience forces towards the pressure nodes or antinodes. This force is a function of the contrast in density and compressibility of the cells or particles and the medium. Therefore, cells or particles that respond differently to the acoustic waves can be forced to accumulate in different positions and collected separately [183]. Optical forces can also be applied to separate cells. A focused beam of light can be applied to directly manipulate cells based on the size or refractive index driven interaction of cells with an optical field. The well-known principles of optical tweezers have been extended from the single optical potential well to extended patterns creating potential well landscapes [191, 192]. Cells with different morphology have been separated simply using the optical potential landscape of a Bessel beam [193]. Advanced light delivery methods such as PCF have also been implemented within microfluidic systems to enable separation of cells based on optical chromatography [194]. The advantage offered by optical techniques is dynamical tuning capability that is limited in other techniques such as dEP or microstructure based methods. The optical sorting schemes can also be integrated with standard biological microscope platforms as well as micro scale devices [192].

It is important to highlight the interplay between optical and electrical forces on biological particles. In the case of optical forces, although relevant forces can be exerted on cells to enable their motion or separation, the magnitude of such forces is $\sim 10^{-12}N$, which is very low. Thus, taking the example of dual beam optical stretchers, high optical powers of $\approx 300\ mW$ or more are required to enable the stretching of cells [64, 66]. Such high powers may result in undesirable effects in cells. Key parameters that define optical traps such as the required power, the trap stiffness and trap size need to be characterised to achieve an optimum performance without risking cell damage. The advantages offered by optical forces such as dynamic tunability can be combined with the large volume handling capability of dEP to achieve enhanced performance in sorting cells. The dEP process, however, also has its limitations. The growth media used to sustain live cells are typically highly conductive. The magnitude of electric field necessary to induce motion of cells may result in the modification of

cell phenotypes either due to the electrical field itself or by subsequent Joule heating phenomena [195]. Moreover, the dEP process may also be affected by variations in the dielectric properties of cells depending on their stage of development and the surrounding microenvironment. Therefore, there is a need to reduce the undesired effects on cells in both optical and electrical field based methods. In this regard, the recently reported method of Light Induced Dielectrophoresis (LIDEP) can prove to be a useful method that combines the optical and electrical fields. LIDEP applies a photoconductive surface such as amorphous silicon to form the electrodes instead of using metal electrodes[196]. Therefore, LIDEP allows the dynamic control over the electric field by tuning the incident light pattern. In addition, the photoconductive surface requires much lower irradiance to activate in comparison with optical traps, allowing the creation of larger area potential landscapes using similar optical powers [196]. Neale *etal*. [196] showed that the power required for trapping a ~ 2 μm particle using the LIDEP trap of 5 μm is two orders of magnitude lower than that required by a similarly sized single beam optical trap. Therefore, it is possible to create traps of similar size in the LIDEP configuration to trap cells using much less optical power compared to standard methods of optical trapping, which is an important consideration for efficient large volume cell sorting.

3.3 DLW enabled cell separator device

The following sections describe the fabrication and validation of a 3D, pressure-driven, deformability based cell separation device that is embedded in fused silica using DLW and customised selective wet etching. The device is capable of sorting a heterogeneous population of cells with varying degrees of deformability into sub-populations of cells with homogeneous deformability. The technology of microfabricated filters developed so far constitute weir-type, pillar-type and membrane filters that are primarily aimed for size-based separation and are typically associated with challenges such as heterogeneity of cell sizes within a population and clogging, which may result in uncontrollable flow-rates within a cell sorting device. These devices have so far been typically applied to separate plasma from whole blood samples [183]. Cellular heterogeneity makes it difficult for such devices to decouple cell deformability from cell size as a separation criterion. Hence, the application of these devices to separate deformable rare cells such

as circulating tumour cells from a mixed cell population risks damaging or losing the rare cells as a consequence of local perturbations in flow-rates which may arise due to clogging. However, for a population of cells with a known size distribution, it may be possible to design a cell separator device that can utilise deformability as the principal separation criterion. The DLW devices presented in this chapter have been developed with an aim to achieve deformability based separation. In particular, the devices are aimed at fractionating human pluripotent stem cells (hPSC) from differentiated cells based on the unique properties of hPSC such as high cytoskeletal deformability, low sub-cellular content and dielectric surface characteristics. This is an experiment beyond the scope of this thesis although chapter 3 proves the working principle using HL60 cells. These devices can be fabricated using cross-flow designs that are known to minimise clogging [183] with the possibility to incorporate electromagnetic fields to augment the separation efficiency. Laser writing and selective chemical etching parameters have been investigated and optimised in order to achieve embedded microchannels with preserved post-etch aspect ratios. As proof of principle, human promyelocytic leukemia cells (HL60) have been used to demonstrate that deformable cells can navigate through carefully etched sub-surface microchannels with a cross-section narrower than the average cell size. The capability of the device in delivering a viable population of cells has been analysed by collecting the cells at the device output and analysing their integrity using a commercial flow cytometer.

3.3.1 Design and working principle

A network of appropriately designed microchannels enabling pressure driven control provides a method to exploit differences in cell deformability without the use of external forces such as magnetic or electric fields that may interfere with cell function. Figure 3.1, illustrates the proof of principle design for the device consisting of a T-junction formed using two microchannels with one inlet port and two outlet ports. At the junction, these microchannels are linked together by constrictions forming a filter region. The cross-section of each constriction is narrower than the average size of a target deformable cell. The two microchannels are maintained at different intra-channel pressures, allowing a pressure gradient to form along the constrictions. If a heterogeneous population of cells with varying degrees of deformability is injected into the

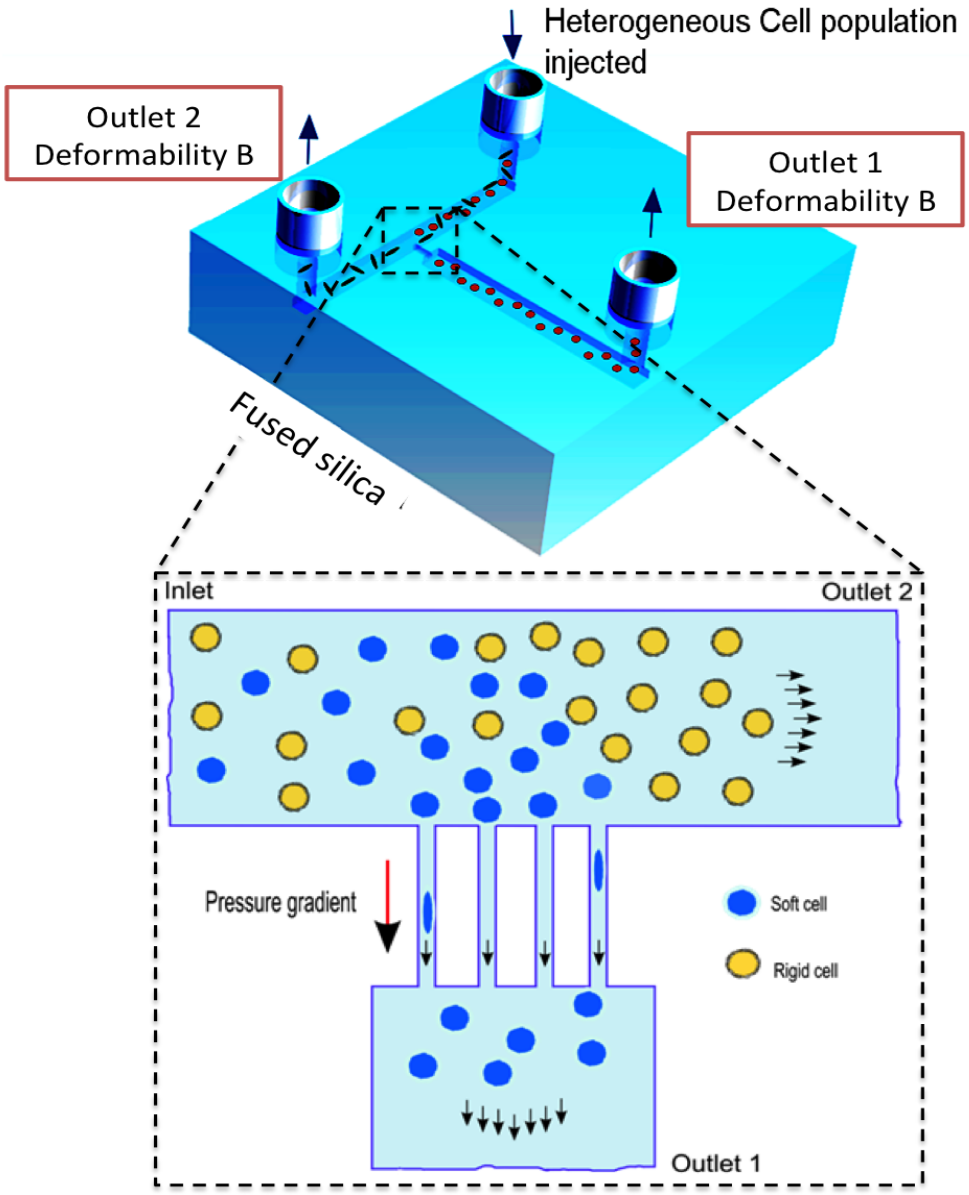

Figure 3.1: Schematic illustration showing the working principle of the initially designed DLW cell separator device. The design consists of two microchannels oriented orthogonal to one another that are linked *via* a series of constrictions, where each constriction is narrower than the average size of a target deformable cell. The two microchannels, if maintained at different intra-channel pressures, create a pressure gradient along the constrictions linking them. If a mixed population of cells with heterogeneous deformability is injected into the device as shown, only the softer cells can deform and travel through the constrictions and be collected at one output. Stiffer cells, unable to deform enough to navigate through the constrictions can be collected at a separate output.

device through the inlet as shown in figure 3.1, the softer cells within the population will be able to deform and navigate their way through these constrictions into outlet 1 of the device. The more rigid cells are envisaged to be unable to deform sufficiently enough to travel through the constrictions and can be collected at outlet 2 of the device.

3.3.2 Device fabrication

Among the several materials that were available for selection as the substrate for device fabrication, fused silica was found to be the most suitable for this work. This is due to several advantages offered by fused silica, such as high optical quality, mechanical robustness, biological and solvent compatibility, thermal stability and a wide optical transmission window. In addition, fused silica exhibits fully controllable photo-induced selective etching rates that can be tailored varying irradiation parameters such as energy, repetition rate, translation speed and even polarisation state of the writing pulses. As discussed in section 2.7, regions in fused silica modified using fs laser pulses exhibit chemical etching rates sensitive to the polarisation of the pulses. The pulse polarisation can be suitably tailored to write sub-surface structures which can subsequently be etched to obtain microchannels with significant difference in aspect ratio. While single channel optofluidic devices have been successfully demonstrated in the recent past [66, 168], the work undertaken in this chapter utilised the polarisation sensitive etching property to successfully fabricate monolithic multichannel devices, demonstrating that fluidic channels with millimetre (mm) and μm scale dimensions can be concurrently etched using the DLW technique.

The multichannel devices in this work were written using ~ 460 fs pulses delivered from a commercial Yb-doped master oscillator power amplifier laser system (IMRA America FCPA μ Jewel D400) at a repetition rate of 500 kHz and a central wavelength of 1047 nm. The pulses were focused inside the volume of a fused silica substrate (Corning 7980, UV Grade) using a 0.4 NA (x20) aspheric objective lens. The substrate was translated through the laser beam focus using high-precision multi-axis air bearing stages (Aerotech Automation 3200). The device is essentially comprised of three fluidic components that required etching *viz.* the microchannels, the inlets and the constrictions. As the work progressed, different designs of the device were fabricated, with different microchannel and inlet dimensions for each design. Each design is con-

textually described in section 3.3.4. To provide an indicative idea regarding the scales involved, microchannel cross-sections ranged between 100 μm × 100 μm to 300 μm × 1 mm and lengths between 1 mm and 8 mm. Both cylindrical and cuboidal inlet ports were used depending upon the requirements of each design. Diameters of circular cross-section inlets ranged between 330 μm and 1.5 mm while for cuboidal inlets, the cross-section used was 400 μm × 400 μm. The cross-section of the constrictions was $\sim \mu m$. Evidently, the significant structural differences between the three components demanded an improvised etching process in order to preserve their respective post-etch aspect-ratios. For this purpose, the polarisation sensitive wet etching property of fused silica at the applied laser writing parameters was optimised for each component as described in section 3.3.3.

3.3.3 Selective etching optimisation

The selective etching optimisation procedure was crucial in enabling the successful fabrication of the device in all its design variations. A parameter acquisition experiment was performed to evaluate the optimum writing pulse polarisation required to fabricate each component. In doing so, the fs pulses at a repetition rate of 500 kHz were focused 200 μm below the top surface of the fused silica substrate which was then translated linearly through the focus spot for a distance of 4 mm at speeds ranging from 100 $\mu m\ s^{-1}$ to 4 $mm\ s^{-1}$. The energy of the focused pulses was varied from 650 nJ to 200 nJ. Single scans were written for each pulse energy and translation speed, which were repeated for three different pulse polarisation states by maintaining the angle (θ_E) between the electric field vector ($\overrightarrow{E}$) and the translation vector ($\overrightarrow{v}$) at 0^o, 90^o and 45^o as shown in figure 3.2, in order to generate a substantial dataset. The fused silica substrate was then ground and polished back to reveal the facets of the laser modified regions. The substrate was subsequently etched using hydrofluoric acid at 5 % dilution in deionised water (H_2O_{di}) for 45 minutes. The etched structures at 280 nJ can be clearly seen in figure 3.2.

The etch rate was evaluated for each parameter scan by dividing the etched length with the etch time. The etch rate was subsequently plotted with respect to the incident pulse energy to determine the pulse energy threshold for the onset of polarisation sensitive chemical etching. Figure 3.3, shows the variation of etch rate with incident

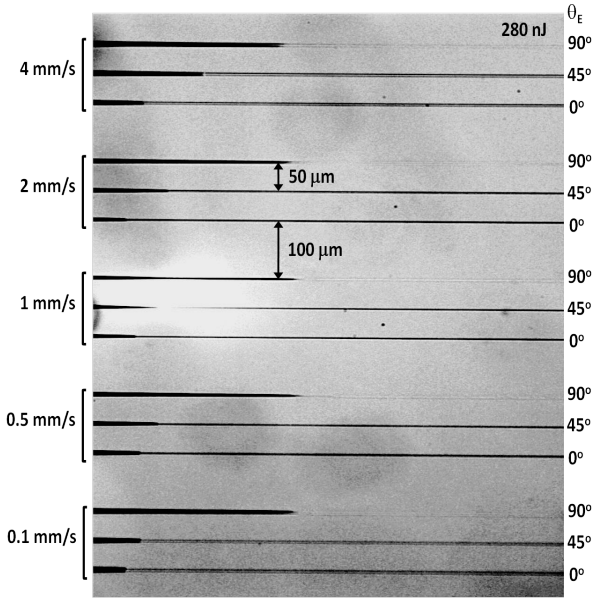

Figure 3.2: Transmission microscope image showing the polarisation sensitive etching phenomenon at a pulse energy of 280 nJ, for 460 fs pulses at a repetition rate of 500 kHz.

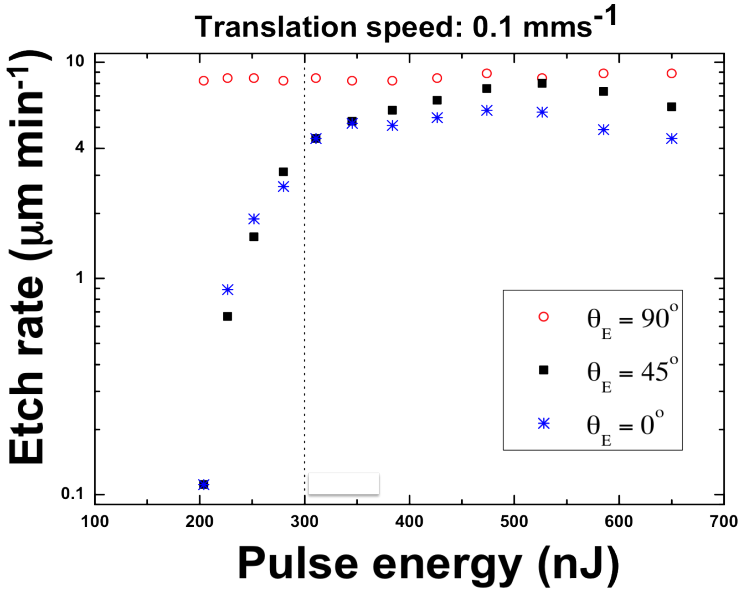

Figure 3.3: The variation of etch rate with incident pulse energy for a translation speed of 0.1 $mm\ s^{-1}$. The pulse energy threshold for the onset of polarisation sensitive etching is observed at $\sim 300nJ$.

pulse energy for a translation speed ($|\overrightarrow{v}|$) of 0.1 $mm\ s^{-1}$. As the incident pulse energy is lowered, a threshold value is observed at $\sim$ 300 nJ, beyond which the etch rate for the case when $\theta_E = 45^o$ and $\theta_E = 0^o$ drops significantly in comparison to that for $\theta_E = 90^o$ until the lowest tested pulse energy of 200 nJ is reached. As discussed in section 2.7, this is attributed to the formation of nano grating structures in the fs laser modified regions within the volume of the fused silica substrate. The pulse energy threshold is further observed to have insignificant effect on the etch rate of laser written structures when $\theta_E = 90^o$. This is a significant result as it creates the opportunity to tailor the etch rates of laser written structures especially for device components with a large differences in aspect-ratio. The pulse energy threshold was observed to be at $\approx$ 300 nJ for $|\overrightarrow{v}|$ of 0.5 $mm\ s^{-1}$ and $\approx$ 380 nJ for 1 $mm\ s^{-1} \leq |\overrightarrow{v}| \leq$ 4 $mm\ s^{-1}$. At pulse energies $\gtrapprox$ 500 nJ, the etch rates were observed to be of the same order of magnitude for the three polarisation states. Thus, by applying appropriate laser writing parameters, the etch rates for mm scale and μm scale structures can be optimised to preserve their post-etch aspect-ratio.

Two versions of the device were fabricated. As shown in figure 3.4, the first version (*ver.1*) of the device consisted of two orthogonally aligned microchannels linked together by a single constriction. In this version, a 3D frame with dimensions of 5 mm $\times$ 5 mm $\times$ 2 mm was laser written in a 2 mm thick fused silica wafer. A contour modification approach was opted for writing the microchannels. Instead of modifying the entire volume, the laser focus spot was scanned such that only the contour of the microchannels was modified. The bottom and top surfaces of the microchannels were written using the multiscan method, which is also used in writing optical waveguides as discussed in section 2.6.2. The width between each scan was maintained at 0.4 μm. The 3D contour for each microchannel was written by scanning planar rectangular paths along the length and width, starting at the bottom surface and incrementally shifted opposite to the beam propagation direction until the top surface of the microchannel was reached. This is illustrated in figure 3.4.

In addition, as shown in figure 3.5 the microchannels were written such that the modified regions extended beyond the frame of the substrate by a short length, typically 100 μm, in order to ensure an exit route for unmodified silica during the etching process.

This contour modification approach significantly reduced the laser writing time per device. The cross-section of both the microchannels was designed to be 100 μm $\times$ 100

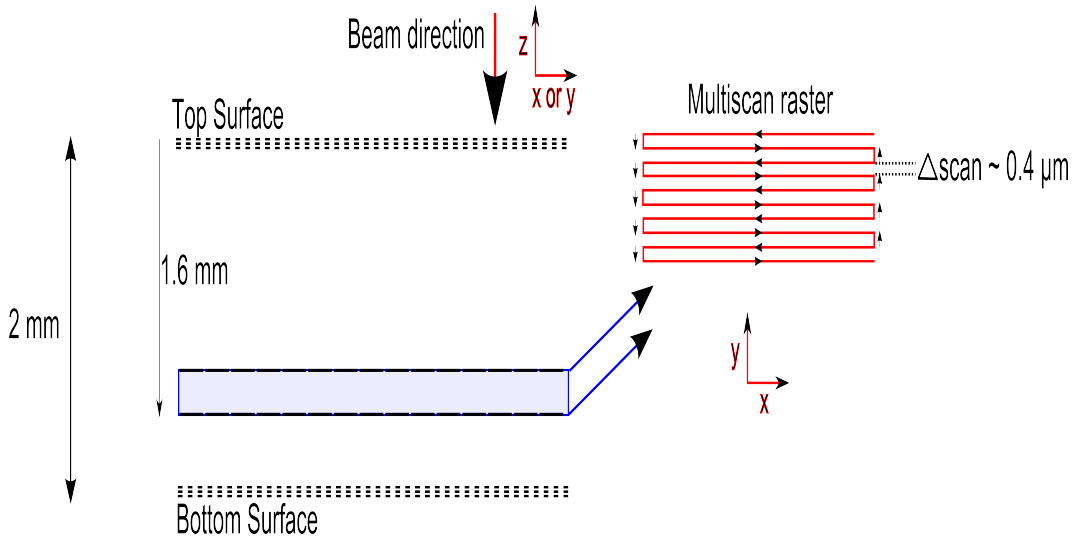

Figure 3.4: Schematic illustration showing the contour modification approach for laser written microchannels. The bottom and top surfaces of the microchannels were written using the multiscan method. The 3D contour for each microchannel was written by scanning planar rectangular paths along the length and width, starting at the bottom surface and incrementally shifted opposite to the beam propagation direction until the top surface of the microchannel was reached. Scan-width was maintained at 0.4 μm for the multiscan raster as well as the 3D contour (not shown in figure). Figure is not to scale.

μm. The microchannel featuring the inlet was 5 mm in length while the orthogonal microchannel was 2.7 mm in length, both microchannels were written at a depth of 1.6 mm from the top surface. Cylindrical fluidic inlet ports were fabricated in a concentric design. The inlets featured a shelf region of depth 300 μm in order to ensure leak-free sealing with glue once the tubes were inserted. The inlets were also designed to be 1.6 mm deep and featured an outer diameter of 1 mm and an inner diameter of 0.8 mm to accommodate tubing. The cross-section of the inlets were written by scanning the laser beam focus in a spiral pattern as shown in figure 3.6. The constriction was fabricated using a single laser scan positioned midway in the cross-section of the microchannels, as shown in figure 3.5. Fluidic interfaces were sealing typically using optical adhesives (Norland, NOA 61)

The microchannels were written using 650 nJ pulses at a translation speed of 2 mm s^{-1} maintaining θ_E at 90^o. The inlets and the device frame were also written using 650 nJ pulses but using higher translation speeds of 4 mm s^{-1} maintaining θ_E at 90^o.

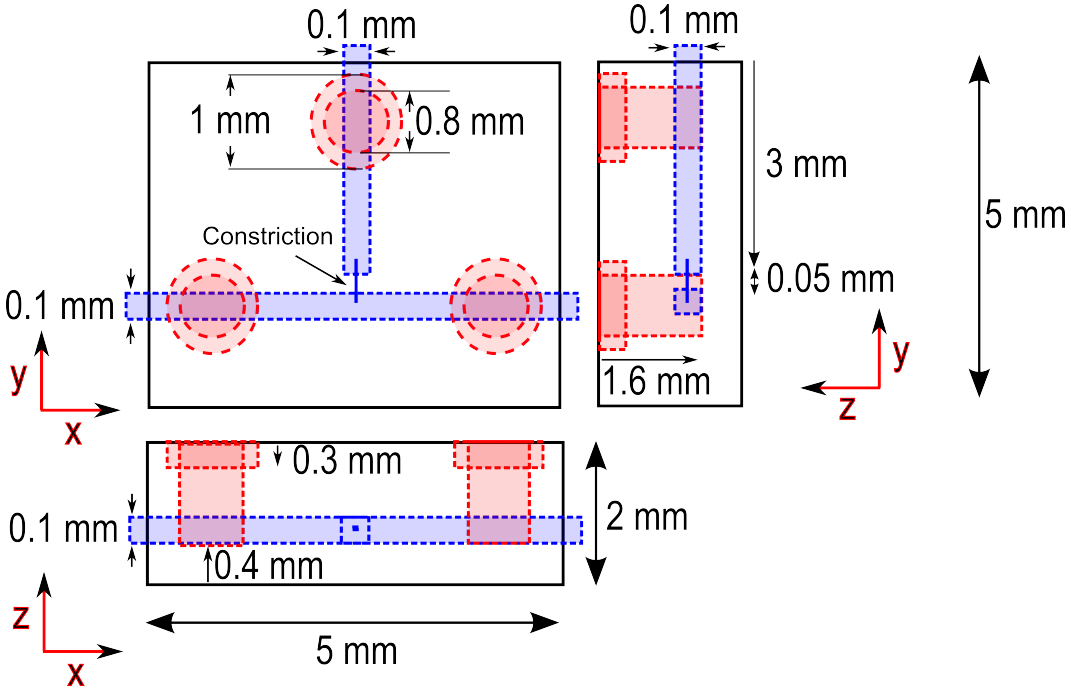

Figure 3.5: Schematic representation of microchannels and inlets for *ver.1* of the device. The microchannels were written such that the modified regions extended beyond the frame of the substrate by a short length in order to provide an exit route for un-etched silica. Figure is not to scale.

However, the etch rates for the frame and inlets were found to be similar when θ_E at 45^o and circular polarisation states were used. The constriction was written using 270 nJ pulses at a translation speed of 0.1 $mm\ s^{-1}$. Assuming the absence of aberrations, the adiabatic parameter (γ) using these conditions can be evaluated using equation 2.2 to be $\gamma \sim 0.2$, indicating that material modification occurs as a combination of both multiphoton and tunnelling effects. In order to minimise unwanted mechanical forces on the cell by forcing them to remain deformed for an extended period of time, the maximum length of the constrictions is set to 200 μm. As imaging was to be performed from the bottom surface of the device, the network of channels were written at a depth of 400 μm from that surface. The laser written device (*ver.1*) was subsequently etched using HF in an ultrasonic bath at 5 % aqueous dilution for 3.5 hours. Chip-to-world interfacing was achieved by directly accommodating tubes inside the cylindrical inlet ports without the need of external adapters. Plumbing was achieved using platinum cured silicone tubing (VWR) with an outer diameter ranging from 640 μm to 750 μm

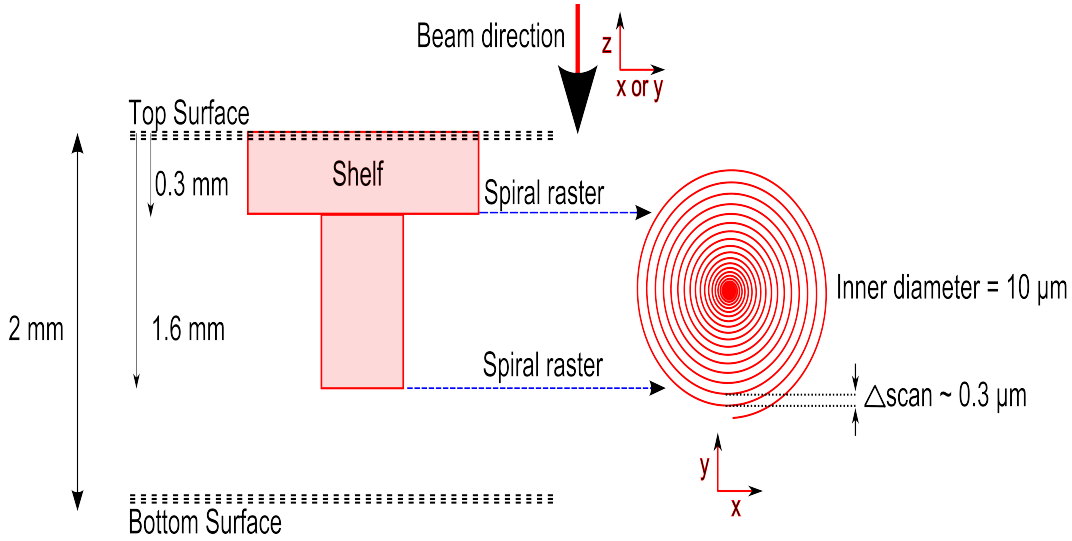

Figure 3.6: Schematic representation of microchannels and inlets for *ver.1* of the device. A shelf region was fabricated to secure the fluidic interfacing with glue and minimise the risk of leaks. The scan-width was maintained at 0.3 μm for the spiral raster as well as the 3D contour of the cylindrical inlet (not shown in figure). Figure is not to scale.

and inner diameter of 300 μm.

The second version of the device (*ver.2*) incorporated two channels aligned to one-another in the axial direction as shown in figure 3.7. The cross-section of the channels was designed to be 300 μm × 1 mm with a length of 3.1 mm for both channels. As illustrated in figure 3.7, the channels were linked using a 2D array of 18 constrictions. The laser rastering methods and spacings used to write the *ver.2* of the device were the same as those applied to write (*ver.1*). The 2D array of constrictions were symmetrically aligned with a spacing of $\sim$ 40 μm across the cross-section of the larger pair of channels. The inlet outer diameter was increased to 1.5 mm. The channels were written using 650 nJ pulses at a translation speed of 2 $mm\ s^{-1}$ while the inlets were written using the same pulse energy at a faster speed of 4 $mm\ s^{-1}$. The constrictions were written using 270 nJ pulses at 2 $mm\ s^{-1}$.

The laser written *ver.2* of the device was subsequently etched in an ultrasonic bath using HF at 5 % aqueous dilution for 11 hours. The long etch time at 5 % dilution can be attributed to the fact that access to the laser modified structures gets increasingly difficult as the etch profile ingresses deeper into the substrate. This issue was addressed by increasing the concentration to 13.3 % (aq.), which subsequently reduced the etch

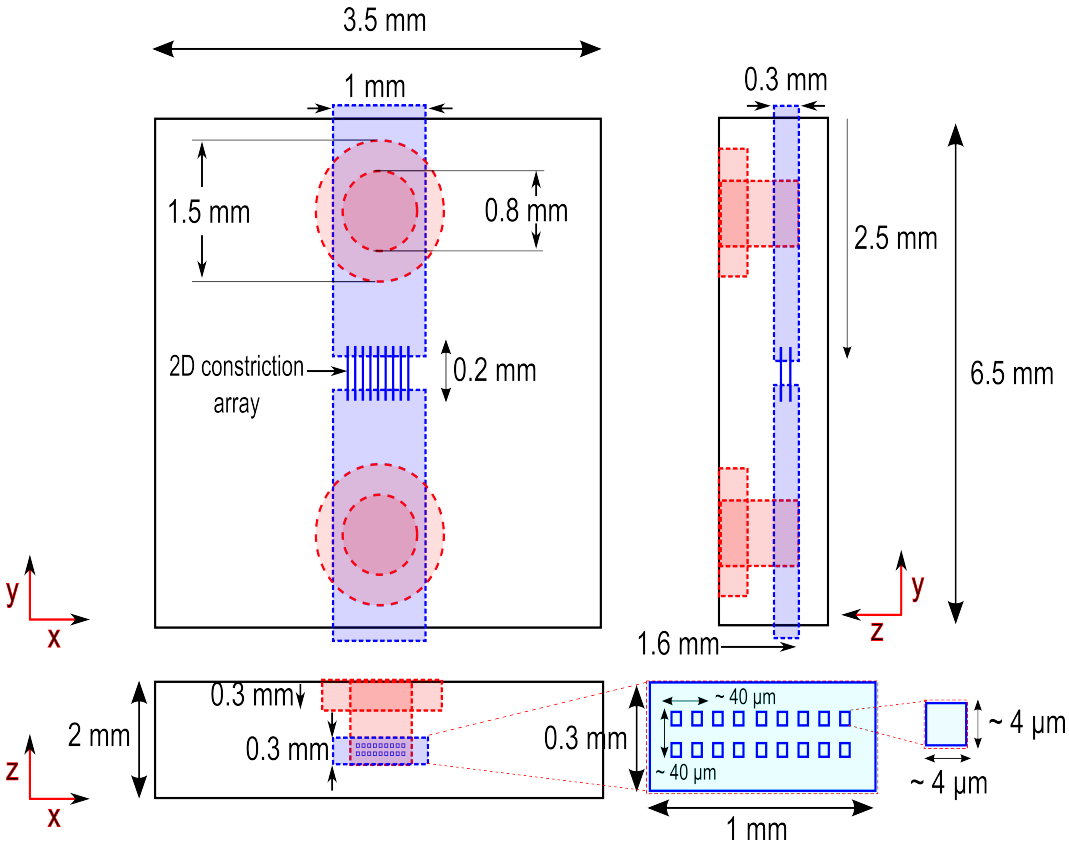

Figure 3.7: Schematic representation of channels and inlets for *ver.2* of the device. The raster methods applied were the same as those applied to write *ver.2*. Likewise to *ver.2*, the channels were written such that the modified regions extended beyond the frame of the substrate by a short length in order to provide an exit route for un-etched silica. The 2D array of constrictions were symmetrically aligned with a spacing of $\sim$ 40 μm across the cross-section of the larger pair of channels. Figure is not to scale.

time to 4.5 hours without compromising the aspect ratio of the laser written structures. It was observed that optimum selection of the length of the microchannels is critical to ensure that the etchant ingression is symmetric and the etch profile arrives at the constriction region from all routes at approximately the same time in order to avoid over etching the structures. Post-etch, the devices were rinsed in an ultrasonic cleaner using H_2O_{di} followed by acetone and isopropyl alcohol (IPA) for 30 minutes to remove any residual traces of HF inside the microchannels.

3.3.4 Performance validation

Performance was assessed by first ensuring that the DLW and selective etching method was capable of producing an optimally sized constriction for cells to squeeze through in an unaltered state. This evaluation was carried out using the single constriction *ver.1* of the device. A pair of comparative optical microscope images of the single-constriction *ver.1* before and after etching is shown in figure 3.8. HL60 cells were selected to test the device performance since they need minimal maintenance *in vitro* and proliferate as single-cell suspension cultures without the tendency to clump or adhere to plastic or glass materials. HL60 cells are also known to possess a non-uniform deformability within a population [197]. Flow rates for sample injection into the microchannels were controlled using a microfluidic syringe infusion pump (WPI, SP100i). Sample collection reservoirs were placed at the outlet ports of the device, which was then placed on an inverted microscope platform (Olympus IX series). The microchannels were initially flushed using phosphate-buffered saline (PBS) in order to remove any residual traces of water. The device showed lag free response to applied changes in flow rate ranging from 1.67 $\mu L\ min^{-1}$ to 1 $mL\ min^{-1}$, indicating that the fluidic interfacing was leak-free and able to withstand high fluid intra-channel pressures.

The HL60 cells cultured in Dulbecco's Modified Eagle Medium (DMEM, Life Technologies) supplemented with 20 % foetal bovine serum (FBS), 2mM glutamine, 100 units of Penicillin and 100 mg of streptomycin per mL were injected into the *ver.1* device through the inlet port at a constant flow rate of 0.5 $mL\ min^{-1}$. Prior to this, a sample of the cells from the same suspension was used to measure the cell size under a microscope, using 3 μm diameter microspheres as a control. The size of the HL60 cells was measured once reproducible growth behaviour was observed after passaging. The average size was obtained to be 11.7 $\mu m \pm 1.1\ \mu m$ with a standard deviation of 1.09 for a sampling number of 25 cells. The output microchannel that features outlet 1, as shown in figure 3.1, was maintained at a lower pressure using an open ended syringe. The constriction was found to be of optimum cross section to enable deformation of the cells during transit. This was carefully measured using a second sacrificial etched device that was ground back and polished in order to reveal the cross-section of the constriction. It was found that the constriction was slightly asymmetric along the laser beam propagation axis as shown in figure 3.9. The longer axis was measured to be

8 μm and the shorter axis 4 μm. Figure 3.9 also shows snapshot images where the HL60 cells can be seen entering the constriction and exiting in the output microchannel travelling towards outlet 1.

The results from device *ver.1* indicate the possibility of separating a heterogeneous population of cells with varying degrees of deformability into sub-populations of cells with homogeneous deformability using a monolithic device fabricated DLW. However, the efficacy of the device for practical purposes would only be justified if the populations of cells at the output reservoirs are not damaged by the process of navigating through narrow constrictions. In order to analyse if this is the case and also to obtain a high throughput, the design was consequently multiplexed into *ver.2*, which incorporated a straight channel configuration with 2D array of 18 constrictions as shown in figure 3.7. Optical microscope images showing the multi-constriction *ver.2* of the device before and after etching are shown in figure 3.8. The HL60 cells, grown using the same process as that used for evaluating *ver.1*, were injected into *ver.2* of the device. A cell viability assessment was performed on the output population of *ver.2* of the device using a commercial fluorescence activated cell cytometer (BD FACSCalibur^{TM}). Figure 3.10 shows the photographs of the multi-constriction device before and after etching.

Prior to introducing cells into the device, they were stained with the BD^{TM} cell-viability-kit. The kit consists of the fluorescent dyes Thiazole Orange (TO) and Propidium Iodide (PI), which are applied to carry out live-dead analysis on cells by probing the integrity of cell membranes. Live cells have intact membranes and are impermeable to dyes such as PI, which can only enter into cells with compromised membranes. In contrast, TO is a permeant dye and enters all cells, live as well as dead, in variable amounts. In evaluating the performance of device *ver.2*, a relatively high flow rate of 167 μL min^{-1} was applied at the syringe pump to deliver the stained HL60 cell sample through the device. A comparative FACS analysis was then carried out on the output population using a control sample of stained HL60 cells from the same batch of cultured cells which were not sent through the device.

Figure 3.11 shows a histogram comparison of the forward scatter results from the FACS analysis, representing cell volume, obtained from the device output and the control experiments. Figure 3.12 shows the respective dot plots showing forward scatter versus side scatter, which represents cell granularity.

A size calibration measurement was undertaken in order to compare the relation of

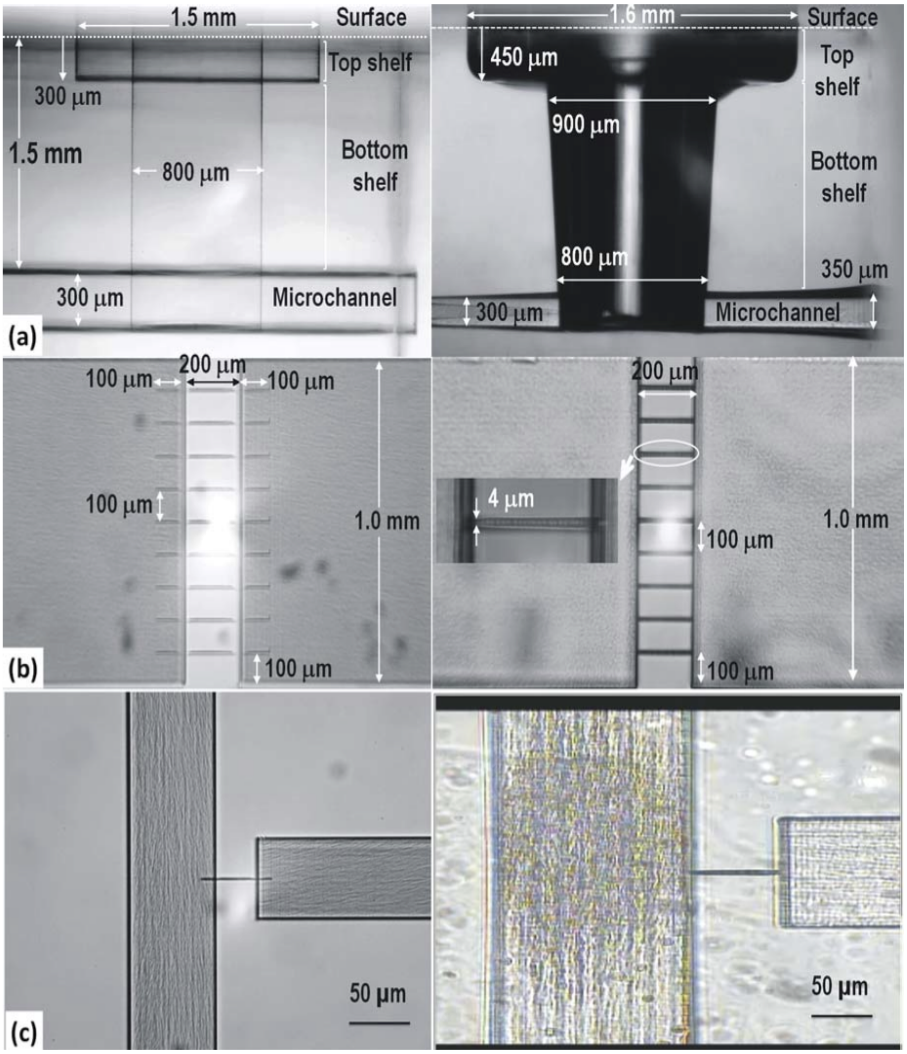

Figure 3.8: Optical transmission microscope images showing *ver.1* and *ver.2* of the device before and after etching. (a) The inlet system viewed side-on. (b) Top view of the 2D constriction array device (*ver.2*). (c) Top view of the single-constriction T-junction device (*ver.1*)

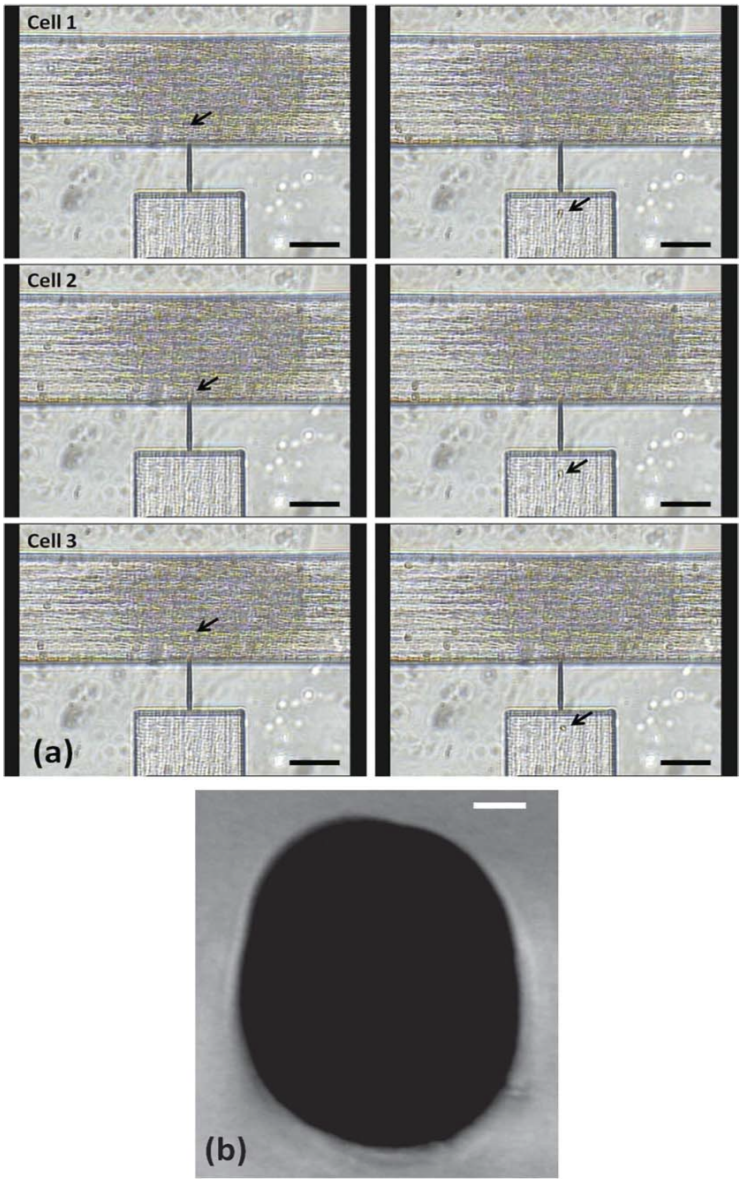

Figure 3.9: Optical transmission microscope images of the single constriction T-junction device (*ver.1*). (a) The HL60 cells can be clearly seen after they travel through the constriction. Scale bar - 50 μm (b) Cross-sectional view of a constriction showing the asymmetry. Scale bar represents 1 μm.

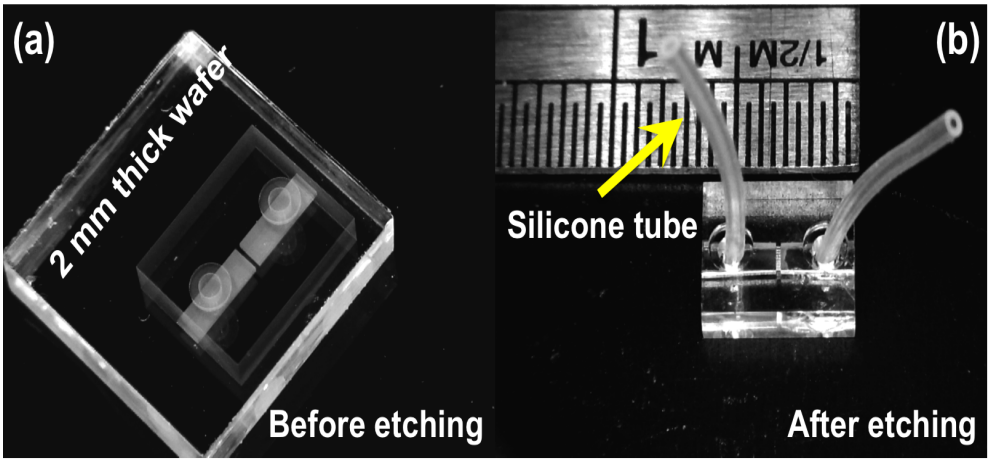

Figure 3.10: Photographs of multi-constriction device (a) before and (b) after etching.

the viable cell size distribution with the constriction size. Polystyrene microspheres of known size (7.6 μm and 10 μm) were injected into the FACS and their forward scatter position noted, as shown in figure 3.11 and figure 3.12. The relative position of the constriction size is also indicated in the figures.

The number of total gated events (30,000) in the device output was kept equal to that of the control for all experiments. The healthy cells in the FACS histogram shown in figure 3.11 and dot plots shown in figure 3.12 correspond to the events in the fluorescence plots that exhibit high TO content but low PI content indicating viable cells. The control data shown in figure 3.12 reveals these cells as a dense population with forward scatter values between ≈550 and ≈800 as marked by the red gated region. Figure 3.13 plots the corresponding gated regions in the fluorescence data showing variation of TO content with PI content. These cells, comprising of 78.6 % of the total gated events in the control have a high probability of being healthy due to the high TO content exhibited, low PI content, large volume and low levels of granularity. Therefore this population forms the region of interest. With respect to size, this population also agrees with the measured cell size of 11.7 μm ± 1.1 μm. In comparison, the data obtained from the stained HL60 cells after being sent through the device revealed 64.3 % of the total gated events to be within the region of interest. Furthermore, compared to the control, a slight increase in events is observed in the device output data at levels of forward scatter $\lessapprox$ 200.

The sub-200 events also showed low levels of both TO and PI in the fluorescence

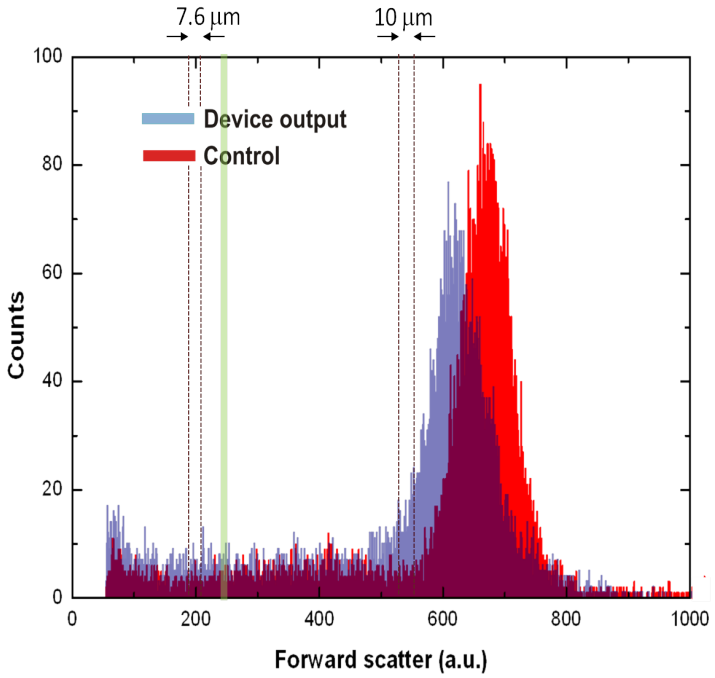

Figure 3.11: Forward scatter histogram plots obtained from the FACS live/dead analysis, showing the position of live cells. Data from the sample that passed through the device is plotted in blue. The control data is plotted in red. The overlaid plots reveal that the healthy population in the control lies between forward scatter values of ≈550 and ≈800 and makes up 78.6 % of the total number of events detected. In the device output, this population lies between forward scatter values of ≈480 and ≈780 and constitutes 64.3 % of the total events. A relative drop in maximum counts is observed in the device output. A shift towards lower forward scatter is also observed in the distribution of the device output indicating a reduction in average size of the viable cells. A corresponding increase in the device output is observed in sub-200 values representing debris from fragmented cells. The vertical dashed bands represent the size of 7.6 μm and 10 μm microspheres that have been used for size calibration. The green vertical band represents the maximum microchannel size of 8 μm.

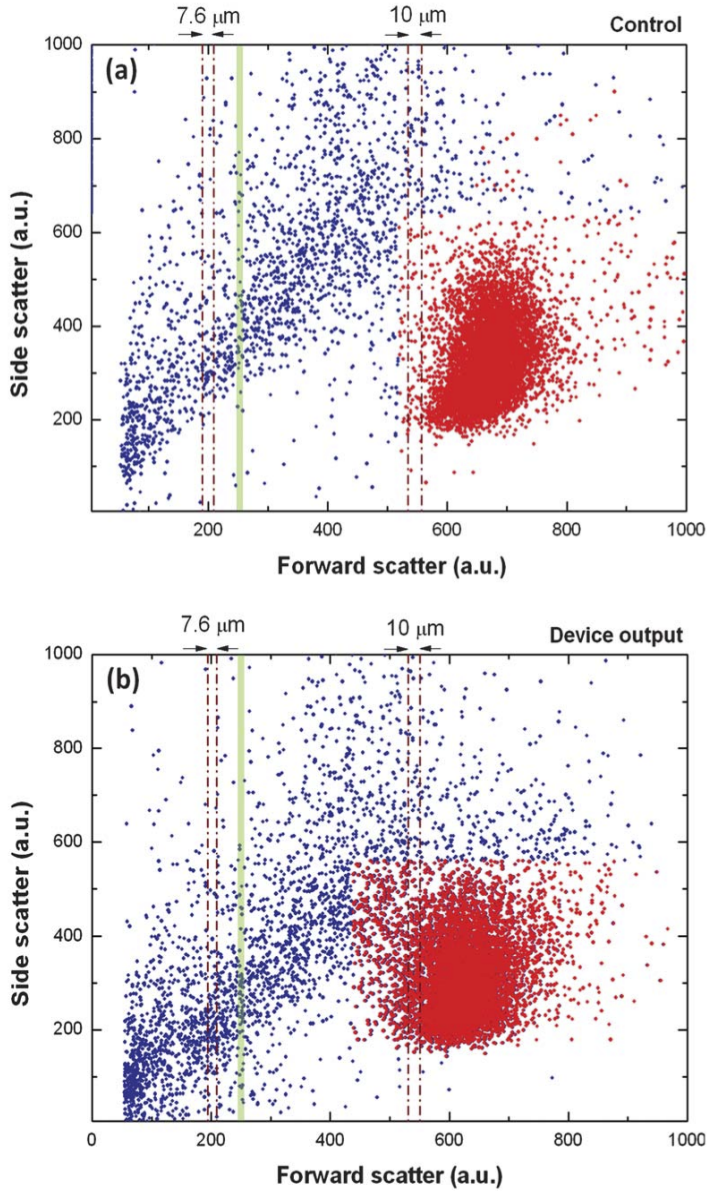

Figure 3.12: Dot plots showing variation of side scatter (SSC) against forward scatter (FSC) after the FACS live/dead analysis. Red dots represent cells stained with TO (all cellular material) while blue dots represent cells that took up PI (dead and injured cells). (a) Dot plot of SSC against FSC of the control. (b) Dot plot of SSC against FSC of the device output. The vertical dashed bands represent the size of 7.6 μm and 10 μm microspheres that were run through the FACS for size calibration. The green band represents the microchannel size of 8 μm.

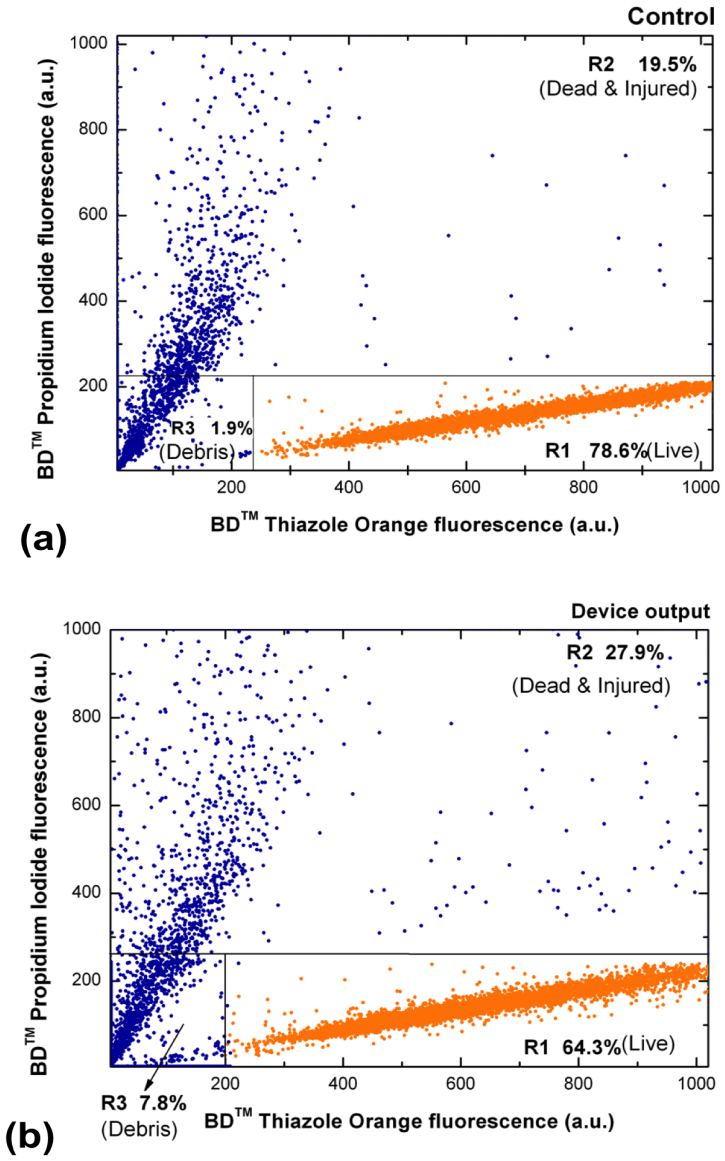

Figure 3.13: Plots showing FACS live/dead analysis data for (a) the control and (b) the device output. The variation of TO fluorescence with that of PI is shown in both experiments.

plots shown in figure 3.13. This indicates an increase in the number of entities much smaller than the average size of healthy cells and can be attributed to fragments from large volume cells damaged during their travel through a constriction, in addition to some small viable cells. Thus, in the dot plots, all objects exhibiting a forward scatter with a value $\lessapprox$ 200 can be considered as debris. This region is gated (R3) in the fluorescence plot as shown in in figure 3.13 and showed an increase from 1.9 % in the control to 7.8 % in the device output. As shown in figure 3.11, this is complemented by a lowering of the maximum counts of healthy cells in the device output when compared to the control indicating a reduction in the number of healthy cells. Correspondingly, in figure 3.11 a shift towards lower forward scatter is also observed in the distribution of the device output, indicating that the average size of viable cells is smaller when compared to the control. In addition, a number of cells in the control that were larger than the average size, as shown in the dot plots in figure 3.12, were found to be absent in the device output. This observation indicates a potential size selectivity application of the 2D constriction array. The minimum PI threshold in gated region R2 in figure 3.13 was selected at a value slightly higher than the maximum PI fluorescence in the gated region R1. The region R2 consists of dead and injured cells and makes up 19.5 % in the control, which increases to 27.9 % in the device output. Events in R2 showing high TO as well as high PI content are attributed to large cells whose membrane has been compromised. It is clear from figure 3.12 that a large proportion of cells had to deform to travel through the constrictions.

The movement of a single cell through a constriction is depicted in figure 3.14. The cell with an un-deformed diameter of $\approx 12\ \mu m$ can be seen to deform considerably as it travelled through a constriction with $4\ \mu m \times 8\ \mu m$ cross-section and a length of $200\ \mu m$. Considering $\sim$ 30,000 cells travelled through the 18 constriction 2D array in 11 min, an estimated $\approx$ 150 cells travelled through a single constriction per minute. Live-dead analysis revealed $\gtrapprox$ 81 % of the cells collected at the device output remained viable. The results indicate that a small population of cells does suffer damage and disruption of cellular integrity after travelling through the constrictions, as expected. However, majority of cells within the healthy population remain viable after travelling through the device and can potentially be grown in culture.

This result presents a simple, label-free separation mechanism based exclusively on cell deformability with promising implications for cellular diagnostic, therapeutic

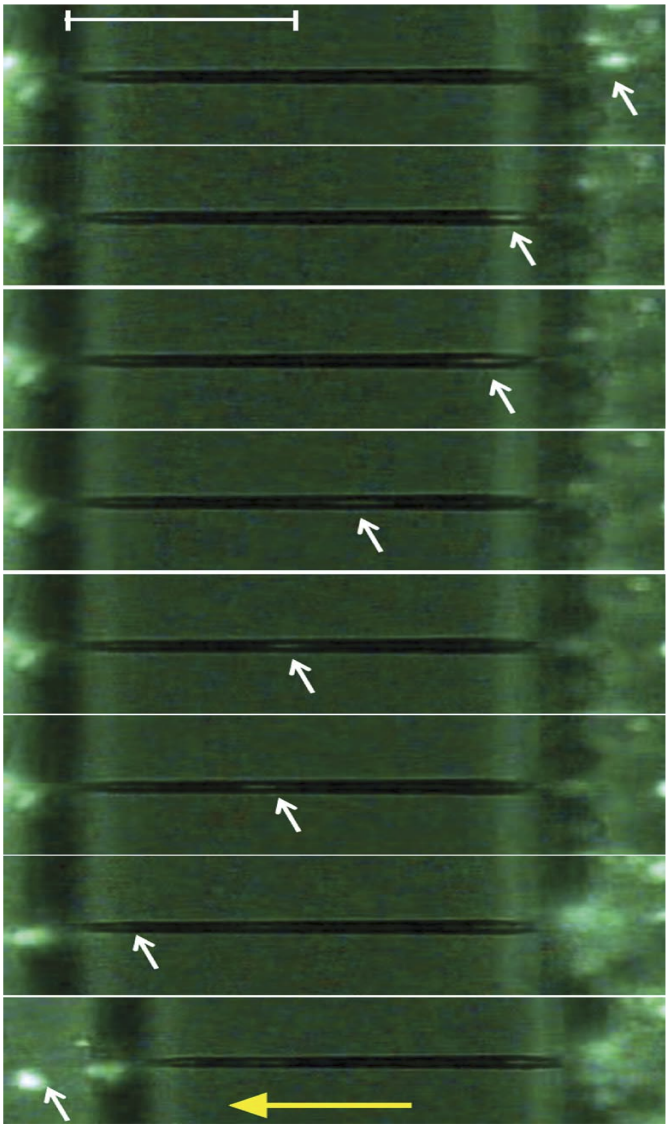

Figure 3.14: Fluorescence microscope snapshot images showing the deformation of a single cell as it travels through the constriction in the multi-constriction device. The HL60 cells were stained using calcein, which is a fluorescent dye with excitation and emission wavelengths of 495 and 515 nm, respectively. The scale bar represents 100 μm. The white arrows show the position of the cells within the constriction. The yellow arrow indicates flow direction.

and drug-development applications. In particular, there is preliminary evidence that hPSC, which are known to be remarkably deformable, progressively become stiffer with the degree of differentiation [198]. The mode of separation investigated during the work undertaken in this chapter indicates its potential applicability in fractionating a population of differentiated cells based on their degree of deformability. Residual hPSC cells amidst the population of differentiated cells can potentially be enriched using a deformability based separation method, a potential that has important ramifications in stem cell therapeutic applications.

3.4 Conclusions and Future outlook

This chapter has presented a DLW microfabrication enabled deformability based cell separator device. The single-constriction and 2D multi-constriction versions of the device revealed promising performance characteristics and robustness. The device has been shown to exhibit high-throughput and more importantly, excellent viability of the output cell populations. With respect to DLW microfabrication, the device presents a cogent example of how selective etching can be customised to suit complex design requirements, which underscores the flexibility, accuracy and repeatability of the DLW technology. Further optimisation of the design and fabrication can lead to an increase in efficiency of separation and, in particular, make the device more suitable for application in separating residual hPSC from differentiated progeny. In *ver.2* of the device there is the possibility of accumulation of debris from fragmented cells near the constrictions that may lead to the formation of unwanted clogs and associated deteriorative effects in cell-flow. This can be alleviated by altering the design to include two parallel microchannels cross-linked using the constrictions. This design, which constitutes *ver.3* of the DLW device, is being termed as the 'X-Sorter' due to its distinctive geometrical shape and is shown in figure 3.15. Unlike earlier versions of the device, the 'X-Sorter' features lateral inlets for fluidic connection and has been laser written using the same parameters as *ver.2* and exhibits a footprint of 2.5 $mm \times 1.5\ mm$. The total fabrication time per device, inclusive of laser writing and selective etching, has been reduced to 3.5 hours. The design incorporates a parallel flow or contraflow scheme between a heterogeneous cell population along one microchannel and growth media in the other. The pressure gradient along the constrictions can be controlled by adjusting the flow

rates in the two channels independently. Initial tests using this design using HL60 cells, have been promising with an observed increase in the output cell population to ≈ 91 %, compared to that obtained using *ver.2* of the device.

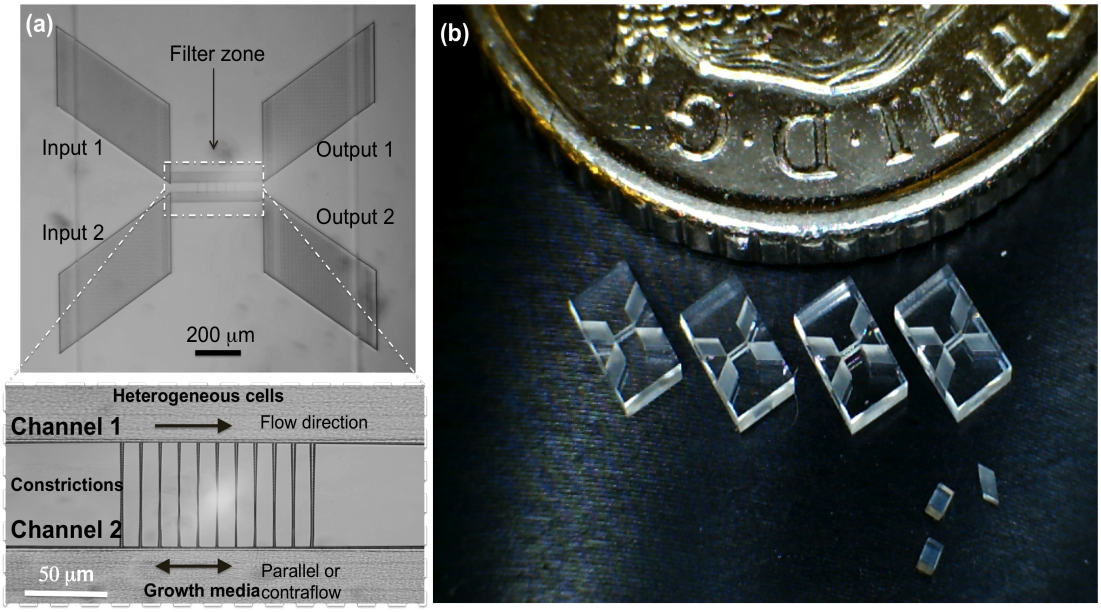

Figure 3.15: The X-Sorter (*ver.3*) of the device. This version features lateral inlets for fluidic connection and has been laser written using the same parameters as *ver.2*. It exhibits a footprint of 2.5 $mm \times 1.5\ mm$

The development of miniaturised cell separation devices is a vast and competitive field. Cell separation technologies over the past several years have focused on improving cell processing speed and maintaining cells as sterile as possible for medical applications. The DLW device presented in this chapter faces stiff challenges towards making an impact in the field. The most important of these challenges include the engineering of the cell sorter under sterile conditions and maintaining cross-contamination within acceptable limits. It is very difficult for a single miniaturised method for sorting cells to meet all the requirements for every cell type. The DLW device is aimed specifically at decoupling cell size from cell deformability as a separation criterion. In addition, performance indicators such as separation efficiency, enrichment ratio and separation resolution also need to be quantified for this device. Therefore, the DLW device shows strong potential for future development, taking into consideration both the fabrication as well as application aspects. Selective etching parameters can be tuned to achieve a

highly uniform cross-section along the length of the constrictions. The design in *ver.3* of the device can be optimised in conjunction with the capabilities of DLW. There is also the potential to increase efficiency of separation by injecting the output from one device into the input of a second and forming a cascaded arrangement including as many devices as required to achieve the desired efficiency. The rapid prototyping capability of DLW is very useful in this scenario to ensure repeatability of fabrication. The design in *ver.3* can also be improved to incorporate cytometric capability. The characteristic tapering observed in DLW fabricated microchannels can be exploited to achieve flow-focusing without using hydrodynamic sheath flows. DLW optical waveguides can then be fabricated at predetermined regions of the device to count the number of cells flowing into and out from the device. Furthermore, the deformability of cells before and after travelling through the constrictions can be quantified using Atomic Force Microscopy (AFM) techniques or dual beam optical stretchers to enable a thorough analysis of the procedure. These optimisations will make future versions of the device well-suited for use in fractionating hPSC and differentiated progeny into separate sub-populations based on deformability.

Apart from sorting cells based on deformability, the device can also be optimised to investigate critical aspects in cancer cell biology, such as the role of nuclear deformation during the capillary transmigration of cancer cells [199]. Materials other than fused silica are potentially more suitable to fabricate constrictions narrower than $\sim 4\ \mu m$, which is discussed in chapter 5 of this thesis.

Relevant publications

1. D. Choudhury, W. T. Ramsay, R. Kiss, N. A. Willoughby, L. Paterson, and A. K. Kar, "A 3D mammalian cell separator biochip" Lab on a Chip **12**, 948-953 (2012).
2. D. Choudhury, W. T. Ramsay, G. Brown, N. D. Psaila, S. Beecher, R. R. Thomson, R. Kiss, S. Pells, N. A. Willoughby, L. Paterson, and A. K. Kar, "A femtosecond laser inscribed biochip for stem cell therapeutic applications," Proceedings of SPIE 7929, 79290P (2011).
3. D. Choudhury, W. Ramsay, N. Psaila, G. Brown, S. Beecher, R. Kiss, N. Willoughby, S. Pells, L. Paterson, and A. Kar, "Sorting stem cells using a femtosecond laser inscribed biochip," IEEE Photonics Society, 2010 23rd Annual Meeting 216âĂŞ217 (2011).

4. D. Choudhury, W. T. Ramsay, N. A. Willoughby, L. Paterson, and A. K. Kar, "Ultrafast laser inscription: science today, technology tomorrow," in B. P. Pal, ed. (SPIE, 2011), Vol. 8307, pp. 83070DâĂŞ83070DâĂŞ11.

Contributions

D. Choudhury designed and fabricated all versions of the cell separator device. R.Kiss assisted D. Choudhury in initial designs. D. Choudhury setup the fluidic systems for the separation experiments. W.T. Ramsay prepared the cell samples required for the experiments. W.T. Ramsay and N.A. Willoughby assisted D. Choudhury in implementing the FACS experiment. D.Choudhury analysed the data.

Chapter 4

Thermal imaging in optofluidic devices

The capability to administer high-precision transient control over microenvironmental factors that influence physiological processes within live cells is becoming an increasingly important aspect in contemporary biological LoC technologies. Temperature is one such factor that facilitates the 'chemistry of life' by enabling thousands of biochemical mechanisms to occur inside a living cell. The regulation of temperature is critical as small thermal fluctuations can alter the intra-cellular dynamics that can lead to a reduction in the cells' metabolic activity, making them unviable [200]. Observations relating to cell biology such as cell proliferation rate, adhesion and gene expression are dependent upon microenvironmental temperature and behaviour observed at different temperatures are typically regarded as incomparable. A few examples amid the spectrum of *in-vitro* biosensing applications within LoC environments that require accurate temperature control include DNA amplification using polymerase chain reactions [201], temperature induced protein mutation [73], thermally controlled neural activity [202] and thermal dependence of the enzyme activity [203]. In addition, the effects of increase in localised temperature are also significant with early stage cancer therapy. Minute elevations in temperature, or mild hyperthermia, has been shown to cause comparatively more disruptive perturbations in the metabolic functionality of tumour cells than in normal cells. Increasing the temperature by $\gtrapprox 5^oC$ leads to severe hyperthermia causing loss of cellular integrity in tumour cells[204]. These observations have led to the active

investigation of localised hyperthermia as a non-invasive alternative to chemotherapy. A number of methods have been developed aimed at the targeted delivery of heat in the tumour site including the use of microwave radiation, radio-frequency pulses and ultrasound waves. However, the *in-vivo* applicability of these methods was found to be limited due to their poor selectivity of tumour cells from surrounding healthy cells resulting in non-specific damage [204]. The spatial resolution issue of targeted cell hyperthermia can potentially be alleviated with the use of NIR lasers in conjunction with nano-materials such as gold nanorods and carbon nanotubes (CNT) that exhibit high absorption cross-section at the relevant NIR wavelengths [204, 205].

Yet another exciting area of research where temperature is a key factor involves the study of thermophilic microbes that are known to thrive in extreme environments such as geothermal vents. Thermophiles survive at temperatures well above 37 ^oC which is the physiological temperature for normal cells and organisms. These microbes cannot be grown using standard growth media and have, so far, eluded laboratory cultivation although attempts at co-culturing these amongst other bacterial colonies have shown promising results [206]. The extraction and characterisation of naturally occurring biologically active antimicrobial compounds from extreme environment microbes is of utmost importance in the development of new antibiotics [207]. With advances in LoC technology it may be possible to recreate the extreme temperatures, pH, stresses and other growth factors in the laboratory and increase throughput and laboratory access to these remarkable species.

The aforementioned examples cite some of the high-priority areas where the application of LoC technology can be exploited with high returns. It is evident that the application of temperature and its accurate control and characterisation within LoC systems is vital to ensure their application in the scenarios mentioned above. This chapter presents a DLW microfabricated optofluidic device with a monolithically integrated NIR waveguide, where the chromatic dependence of laser-induced thermal effects within a microchannel is analysed using quantum dot (QD) thermal imaging. Section 4.1 discusses the role of nano-materials as temperature sensors and heat generators within a microchannel. The application of these nano-materials in the spatio-thermal imaging within an optofluidic device is presented in section 4.2. Sections 4.2.1 and 4.2.2 discuss the fabrication of the device and the confocal fluorescence imaging setup used in this experiment. The device performance with respect to wavelength is dis-

cussed in section 4.3.1 while the effect of CNT as heat generators is discussed in section 4.3.2. Finally, concluding remarks and future prospects of the work undertaken in this chapter are presented in section 4.4.

4.1 The role of nano-materials as thermal sensors and heaters

Semiconductor nano crystals, otherwise known as quantum dots, exhibit characteristic absorption and emission properties that can be adequately tuned by varying the QD size [208]. These remarkable materials are traditionally manufactured from metal chalcogenides and range in size from $\approx$ 2 - 10 nm and can be tailored for narrow symmetric emission bands typically between $\approx$ 525 - 800 nm upon suitable excitation in the visible region of the electromagnetic spectrum. QD typically exhibit a large two-photon absorption cross-section that enables their efficient fluorescence emission when excited using NIR excitation wavelengths. Semiconductor QD with dot size of only a few nanometers have been demonstrated to be excellent candidates for bio-imaging applications with several advantages including deep tissue penetration of their emitted signals, reduced auto-fluorescence, better signal to noise ratio and superior spatial resolution that are required in bio-imaging [209, 210]. The study of QD properties with relevance to bio-imaging has been reported using a number of semiconductor materials including cadmium sulphide (CdS), cadmium selenide (CdSe), indium phosphide (InP) and cadmium tellurite (CdTe), with respective emission spectra spanning the visible and NIR wavelengths of the electromagnetic spectrum [211]. QD are also known to exhibit a high thermal sensitivity of their fluorescence bands. This property has led to their recent use in nano-thermometry applications with high thermal resolution. CdTe QD in particular have been demonstrated to exhibit impressively high thermal sensitivity of their fluorescence bands. The brightest CdTe QD emission has been reported from dots with $\approx$ 3.8 nm diameter in which the thermally induced spectral shift is $\approx$ 0.35 $nm/^oC$ leading to excellent temperature resolutions well below 0.5 ^oC [212]. In comparison with previously used organic compounds, CdTe QD show superior photo-stability over longer timescales, larger molar absorption coefficients, better thermal stability and improved fluorescence quantum yield in the NIR [213] thereby

alleviating some of the limitations associated with organic dye based thermometry. The cytotoxicity of QD can be reduced using appropriate surface functionalisation for application in intra-cellular temperature measurements, which has far-reaching potential as high-sensitivity biological thermal probes [214]. Single walled carbon nanotubes constitute another rapidly emerging class of biologically significant nanoscale materials. These unique nanoscale structures are known to possess high structural strength, high aspect-ratio and are outstanding thermal and electrical conductors [215]. Single walled CNT are known to absorb strongly in the 'tissue-transparent' NIR window ($\approx$ 700 - 1000 nm) of the electromagnetic spectrum within which, biological systems are known to be highly transparent [216]. This makes CNT a promising tool for targeted cell hyperthermia when combined with suitable tumour markers [205]. A number of advancements have been reported where the exceptional optical, thermal and electrical properties of QD as well as CNT have been applied for therapeutic, imaging and diagnostic biomedical applications [21, 217]. This chapter applies both the nanoscale materials in conjunction with each other to present a non-invasive method of thermometry in optofluidic devices.

4.2 Spatio-thermal imaging in a DLW enabled optofluidic device

Optofluidic devices involve the application of light to manipulate live cells in addition to molecular analytes. Therefore, an appreciation of thermal aspects associated with such devices is becoming exceedingly important both in respect of avoiding detrimental effects on the viability of normal cells as well as causing targeted damage to tumorous cells. Knowledge of thermal effects is also relevant in the case of biomimetic devices aimed at replicating *in-vivo* conditions in the laboratory. In addition, a rigorous understanding of the temperature distribution created in microfluidic channels would offer insights into the existence of additional forces that may arise due to the presence of non-negligible thermal gradients such as those leading to photothermal trapping [218]. The work carried out in this chapter addresses these key aspects in optofluidic devices. The application of semiconductor QD as probes for temperature sensing and single walled CNTs as nano-heaters is demonstrated in order to understand the temperature

distribution in microchannels within optofluidic microenvironments. Specifically, CdTe QDs are used to accurately determine the magnitude, spatial distribution and spectral dependence of temperature increments within a microchannel in an integrated optofluidic chip that is locally illuminated by a buried NIR waveguide. The light-induced local heating of an aqueous fluid within the microchannel was determined from the analysis of the spectral position of the CdTe QD fluorescence band. The validity of CdTe QDs as nano-thermometers was evaluated by measuring their thermal loading effect within the aqueous microchannel environment using multiple laser wavelengths. Results obtained were compared to those predicted by simple theoretical models for laser-induced heating in optical traps [219]. Subsequently, the work done was extended to the analysis of how light-induced thermal loading of microchannels is affected by the presence of absorbing particles (CNTs) within the fluid. Analysing the experimental data within the frame of simple theoretical models enabled the estimation of the contribution of the absorption coefficient of CNTs that can be attributed to heat generation. Furthermore, scanning confocal fluorescence imaging was applied to obtain a 2D spatio-thermal map of the microchannel during its illumination by a single NIR waveguide in the presence of CNTs.

4.2.1 Device fabrication

The monolithic device with a microchannel and a single optical waveguide was fabricated using the process of DLW followed by selective chemical etching. Laser writing of the device was performed using 460 fs pulses at 1047 nm delivered from the IMRA laser system described in section 2.5 at a repetition rate of 500 kHz. The pulses were focused using a 0.4 NA ($\times$ 20) aspheric lens within the volume of a 2 mm thick fused silica substrate (Corning 7980, UVFS). Assuming the absence of aberrations, the adiabatic parameter (γ) using these conditions can be evaluated using equation 2.2 to be $\gamma \sim 0.2$, indicating that material modification occurs as a combination of both multiphoton and tunnelling effects. As illustrated in figure 4.1(a), the device consists of an optical waveguide aligned orthogonal to a 5 mm long embedded microchannel featuring a cross-section of 100 μm $\times$ 100 μm. Fluidic interfacing was achieved using cylindrical inlet and outlet ports, each with an outer diameter of 1 mm. The laser writing scheme applied in fabricating the microchannel and inlets was the same as that described in

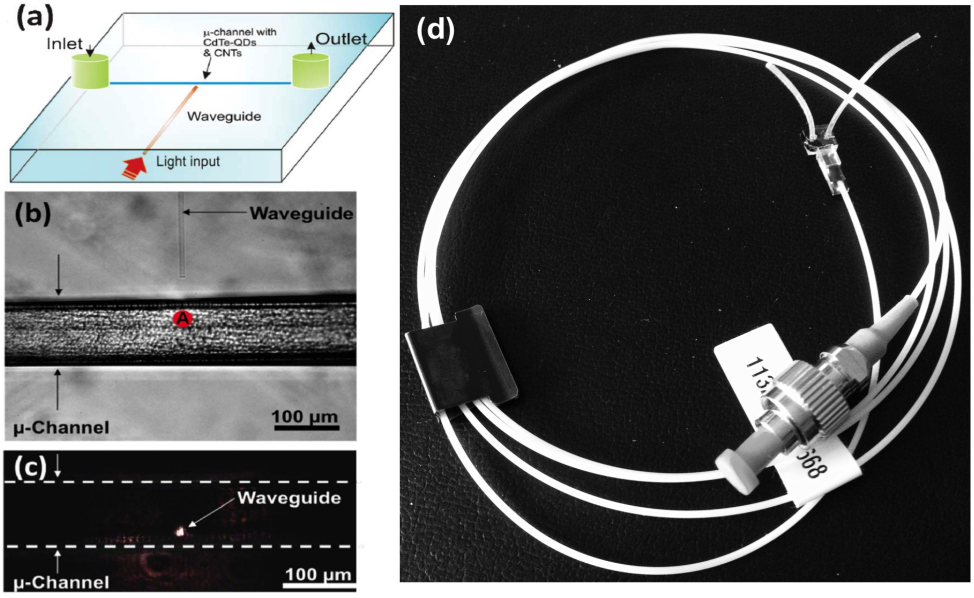

Figure 4.1: (a) Schematic representation of the DLW remote thermometry device showing the microchannel and optical waveguide arrangement. (b) Top view optical transmission image of the device. The 100 μm wide channel as well as the buried waveguide are clearly indicated. The marked point (A) corresponds to the intra-channel location where maximum laser-induced heating was observed and where 'single-pointÕ thermal measurements were performed. (c) Side view of the microchannel when a 633 nm laser was coupled into the buried waveguide. Focal plane while taking the image was set at the channel wall nearest to the waveguide. (d) Photograph of the device

section 3.3.2. The optical waveguide was written using the multiscan technique with each laser scan laterally offset by 0.4 μm, constructing a geometrical cross-section of 8 μm × 8 μm. The components intended for selective etching were written using 650 nJ linearly polarised pulses and a translation speed of 4 $mm\ s^{-1}$, while the waveguide was written using 290 nJ circularly polarised pulses at a translation speed of 2 $mm\ s^{-1}$. The DLW device was subsequently etched for 5 hours using hydrofluoric acid at 5 % dilution in H_2O_{di}. Post etch, the waveguide was polished back to reveal the facet, which was then bonded to a single-channel fibre array (Opteron Co.) using UV curing optical adhesive (Norland NOA-61) to form a robust, re-usable device. Figure 4.1(b) shows the optical transmission image of the etched microchannel and optical waveguide that form the device. Figure 4.1(c) shows the side-view of the microchannel with the buried waveguide when light from a 633 nm laser was coupled to it while aligning the

fibre-array. Figure 4.1(d) shows a photograph of the device.

4.2.2 Confocal fluorescence thermal imaging

The optofluidic device was setup for thermal imaging by filling the microchannel with an aqueous solution of monodisperse CdTe QDs at a concentration of 0.3 % by mass. Once filled, the microchannel was sealed at both ends to ensure that there was no flow in the solution containing the QD. The commercially obtained CdTe QDs (Plasmachem Inc., PL-QDN-650), were 3.8 nm in diameter. The QDs were surface functionalised using thiocarboxylic acid such that the sulphur atoms were covalently bonded to Cd and the carboxylic acid groups remained suspended around the surface of the QD. The characteristic temperature-induced spectral shift of CdTe QD is highly sensitive so that thermal reading can be achieved from the accurate determination of the shift fluorescence peak position which at room temperature of 25 ^oC is centred at 650 nm. As the QD size is known to determine both thermal sensitivity as well as brightness, the 3.8 nm size for the QD used in this work was chosen as it provides a good balance between the two characteristics [209]. The temperature-induced spectral sensitivity of the QD used in the experiment was 0.35 $nm/^oC$. In order to achieve thermal sensing and imaging a custom-built confocal fluorescence microscope was applied. The schematic illustration of the setup is provided in figure 4.2.

The optofluidic device was placed on a XY motorised stage (PIHera^{TM}, P-622.1CD) with a 10 nm resolution. An Argon ion cw laser was used to provide a beam that centred at 488 nm, which was focused into the microchannel using a 50× long working distance microscope objective with a NA of 0.55. The CdTe QD emission generated from the 488 nm focal point was collected using the same microscope objective and, after passing through appropriate filters and confocal apertures, was spectroscopically analysed using a high-resolution spectrometer (Ocean Optics, HR2000). Bright-field imaging was performed using a 20× objective as shown in figure 4.2. The axial and lateral resolutions of the confocal fluorescence system have been estimated to be 3.6 μm and 0.6 μm, respectively. These spatial resolution parameters depend upon the NA of the focusing objective, the effective refractive index of the medium (n_{eff}) and wavelength of excitation ($\lambda_{excitation}$) and emission ($\lambda_{emission}$) and were evaluated using

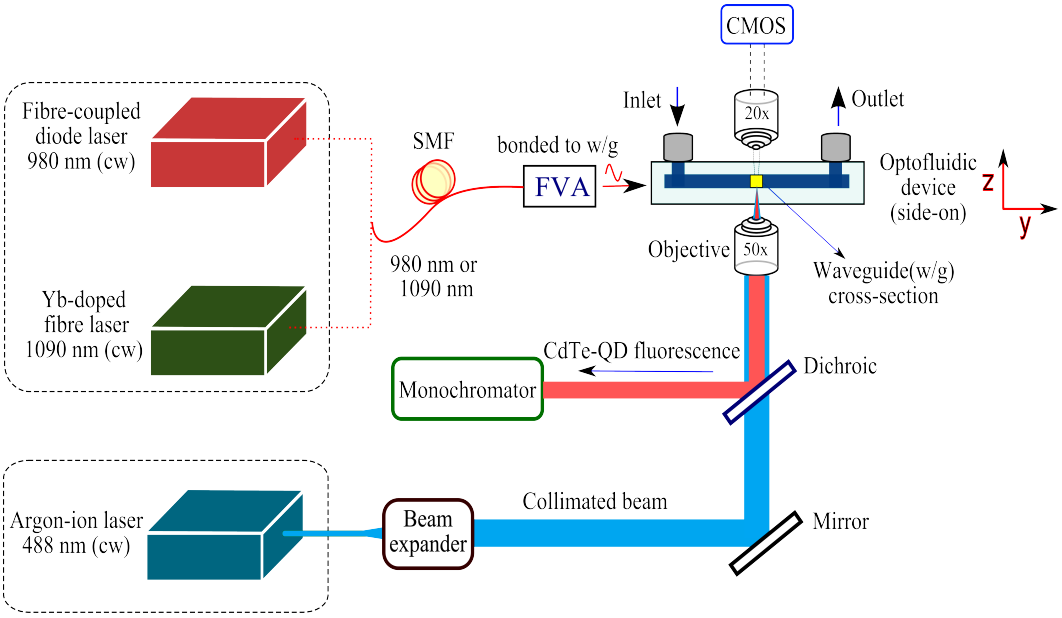

Figure 4.2: Schematic illustration of the experimental setup showing the confocal microscope arrangement used for fluorescence thermal sensing and imaging in the optofluidic device.

the following expressions [220] since the pinhole aperture is larger than the Airy Unit.

$$(Resolution)_{axial} = \frac{0.88\lambda_{excitation}}{n_{eff} - \sqrt{n_{eff}^2 - NA^2}} \tag{4.1}$$

$$(Resolution)_{lateral} = \frac{0.51\lambda_{emission}}{NA} \tag{4.2}$$

Figure 4.3 shows a typical CdTe QD emission spectrum obtained in the confocal microscope when the 488 nm beam was focused inside the microchannel. In this figure, the location of the emission peak as well as the relation between its spectral position and the QD temperature increment (ΔT) with respect to room temperature (25^oC) are indicated.

Using the confocal setup, the local enhancement of temperature as a consequence of incorporating absorbing nano-centres in the aqueous solution was evaluated. For this purpose, single-walled CNTs provided by Sigma Aldrich Ltd. with a concentration

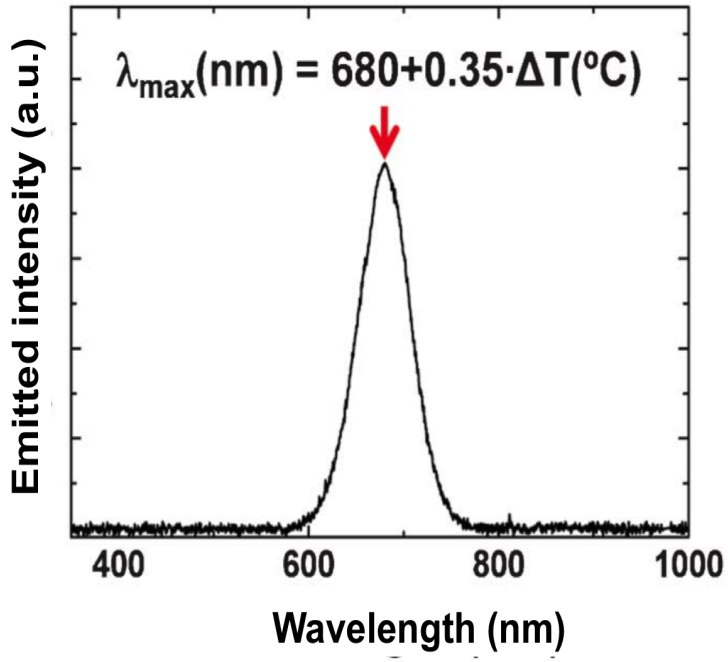

Figure 4.3: Typical intra-channel CdTe-QD emission spectrum obtained using the confocal experimental set-up. The location of the peak wavelength and its relation with temperature change (with respect to 25^oC) is indicated.

of 0.1 % by mass were injected into the aqueous solution containing CdTe QD sensors. Thermal imaging experiments were undertaken in which the laser-induced thermal gradients were generated by launching NIR light into the buried waveguide. The NIR wavelengths used were 980 nm and 1090 nm cw laser radiation provided by a diode laser or a Yb-doped fibre laser, respectively as shown in figure 4.2. In both cases, the maximum power launched into the optofluidic device was close to 600 mW. Pump power was, in both cases, controlled through the laser drive current.

The thermal measurements were always performed under steady-state conditions. In other words, in the determination of the optical power dependence of laser induced thermal loading, each measurement was performed after 1 minute between consecutive measurements to ensure steady state conditions were reached. The integration time for spectrum acquisition was maintained at 1 s in all cases, which was sufficiently long to acquire an emission with high SNR. Lower integration times led to a reduction in SNR and consequently an increase in uncertainty in the peak emission wavelength

determination, thus reducing sensitivity. Integration times above 1 second did not provide appreciable improvement in the quality of the emission spectrum.

4.3 Device performance

Prior to each experiment, the thermal response of the CdTe QD from a single batch was assessed against its calibrated value by measuring its spectral shift while being heated in an aqueous solution in a 0.1^oC oven. The thermal coefficient was found to be 0.35 $nm/^oC$ in all cases. The experimentally observed uncertainty in the thermal coefficient when using different batches of the CdTe QD was found to be $\lessapprox 0.1$ $nm/^oC$. The uniformity of the thermal coefficient was vital in carrying out the experiments and assess the performance of the device with respect to pump wavelength as well as the presence of absorbing nanoparticles. The observations are discussed in sections 4.3.1 and 4.3.2 respectively.

4.3.1 Influence of pump wavelength

One of the cornerstone biological applications of optofluidic devices is the achievement of optical trapping of live cells. However, as water exhibits non-vanishing absorption coefficients in the NIR, optical trapping in an aqueous environment is accompanied by laser-induced local heating [221]. Assuming a cylindrical geometry for heat generation and dissipation, it is possible to theoretically predict the laser-induced temperature increment, ΔT at the focus in a liquid, which can be written as shown in equation 4.3 [219].

$$\Delta T = \frac{P_{in}\alpha_{abs}}{2\pi K} ln \frac{D}{w_o} \tag{4.3}$$

In this equation, P_{in} is the laser power in the location of the liquid, α_{abs} is the absorption coefficient of the liquid at the laser wavelength, K is the thermal conductivity of the liquid, D is the shortest dimension of the micro-chamber containing the liquid along the light path, and w_o is the laser beam waist. The absorption coefficient can be further represented as shown in equation 4.4.

$$\alpha_{ext} = \alpha_{scat} + \alpha_{abs} \tag{4.4}$$

where α_{scat} is the scattering coefficient. In the case of distilled water, where scattering of light is negligibly small, it is reasonable to assume $\alpha_{ext} \approx \alpha_{abs}$. The absorption coefficient of distilled water is shown in figure 4.4.

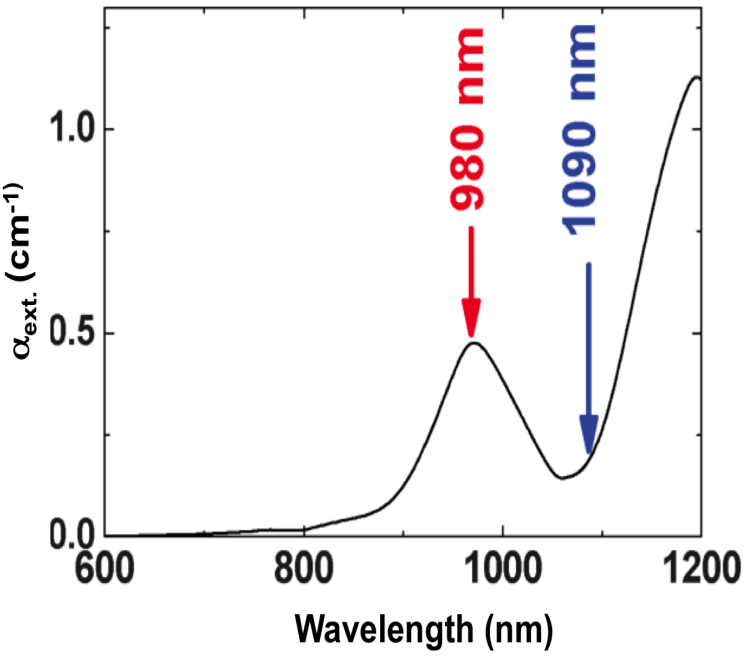

Figure 4.4: Room temperature absorption spectrum of distilled water in the 600–1200 nm range. Arrows indicate the absorption coefficients for the two laser wavelengths used in this work (980 and 1090 nm).

From figure 4.4, it is evident that the use of wavelengths above 800 nm for trapping will be accompanied by local heating and this has been widely reported in the literature. This marked difference in absorption can be utilised to explore the ability of QD based thermometry for the determination of laser-induced local heating effects in optofluidics.

In the experimental setup illustrated in figure 4.2, the launched laser light travels through a number of optical elements before reaching the microchannel including a length of optical fibre, the single-channel fibre array and finally the buried DLW waveguide. This makes it important to obtain a quantitative measure of the light reaching the microchannel as, due to coupling mismatch between the single-channel fibre array and the waveguide, the net laser power reaching the microchannel (P_{in}) could differ from the initial laser power launched into the system (P_{launch}). In order to determine the

actual ratio between P_{in} and P_{launch}, the laser-induced heating rate was first measured with respect to P_{launch} at 1090 nm. A heating rate of $(\frac{\Delta T}{\Delta P_{launch}})_{1090nm} = 3.1^oC\ W^{-1}$ was observed. This observed value can be compared to the 1090 nm laser-induced heating rate with respect to P_{in} as predicted by equation 4.3 and experimentally corroborated results from the literature which is $\approx 12^oC\ W^{-1}$. Comparing the magnitudes of both, it is possible to extract the required ratio $(\frac{P_{in}}{P_{launch}})_{1090nm}$ to be ≈ 0.25. Knowledge of this ratio enabled the analysis of heating rates with respect to the laser power reaching the microchannel instead of the launched power.

With an aim to evaluate the QD based thermometry data as well as the check the validity of the laser power calibration procedure, the laser-induced local heating produced when the microchannel is optically excited at 980 nm was investigated. As shown in figure 4.4, at 980 nm the water absorption coefficient exhibits a local peak at $\approx 0.5\ cm^{-1}$, which is more than twice the absorption coefficient exhibited at 1090 nm. Thus, it is evident that a larger local heating is expected under 980 nm excitation. The microchannel temperature was measured for 980 nm illumination at the closest point to the waveguide as indicated by point A in figure 4.1. The variation of temperature with P_{in} is shown in figure 4.5.

Clearly the microchannel temperature increases linearly with the incident laser power. This is in agreement with equation 4.3. From the experimental data plotted in figure 4.5, the heating rate of $\frac{\Delta T}{\Delta P_{in}}$ at 980 nm can be evaluated to be $\approx 55^oC\ W^{-1}$. This experimentally calculated value can be compared to the theoretical estimation by employing equation 4.3, which yields $\frac{\Delta T}{\Delta P_{in}}$ at 980 nm to be $\approx 45^oC\ W^{-1}$. The experimentally observed data are consistent with theoretical predictions. The $\frac{\Delta T}{\Delta P_{in}}$ at 980 nm obtained here can also be compared, within a first order approximation, to that previously reported by Mao *et al.* in an optical tweezers system [219] where a $\frac{\Delta T}{\Delta P_{in}}$ at 980 nm value of 56 $^oC\ W^{-1}$ was reported. This is in excellent agreement with the experimental results reported here. The results described in this section clearly confirm CdTe QD thermometry as a valid approach for fluorescence thermal imaging of optofluidic devices. This underpins its application in the thermal imaging of laser-excited optofluidics containing absorbing centres, as demonstrated in section 4.3.2.

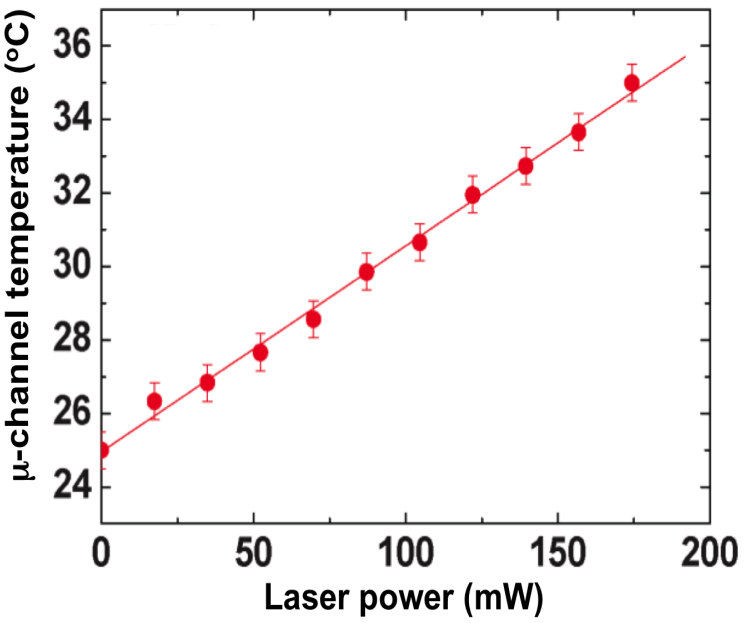

Figure 4.5: Local temperature as measured at point A within the microchannel as a function of 980 *nm* laser power reaching the microchannel. The error bars indicate the maximum error observed in temperature when the experiment was repeated 5 times.

4.3.2 The thermal loading effect of absorbing nanoparticles

As discussed in the introductory paragraph of this chapter, although laser-induced heating is usually regarded as an undesirable effect, there are applications where laser-induced heating is desirable and should be exploited such as targeted cell hyperthermia. Within the *in vitro* context of characterising the light-induced hyperthermia, it is important to achieve the controlled heating of a trapped cell to enable a systematic study of the thermal dependence of cell properties such as elasticity, growth and division rates and membrane stability.

In an optofluidic setting, controlled cellular hyperthermia can be achieved by incorporating heat-absorbing nanoparticles in the fluid containing the cells. While single walled CNTs are known to induce strong heating when optically illuminated in the NIR, the magnitude and spatial distribution of the laser- induced temperature variations induced by CNTs in an optofluidic device has not been studied. The device addresses this particular need in the field. In this regard, an aqueous solution of both

CdTe QD and CNT at 0.3 % and 0.1 % concentrations by mass respectively, was injected into the optofluidic device. The absorption spectrum of the CdTe QD and CNT solution is shown in figure 4.6.

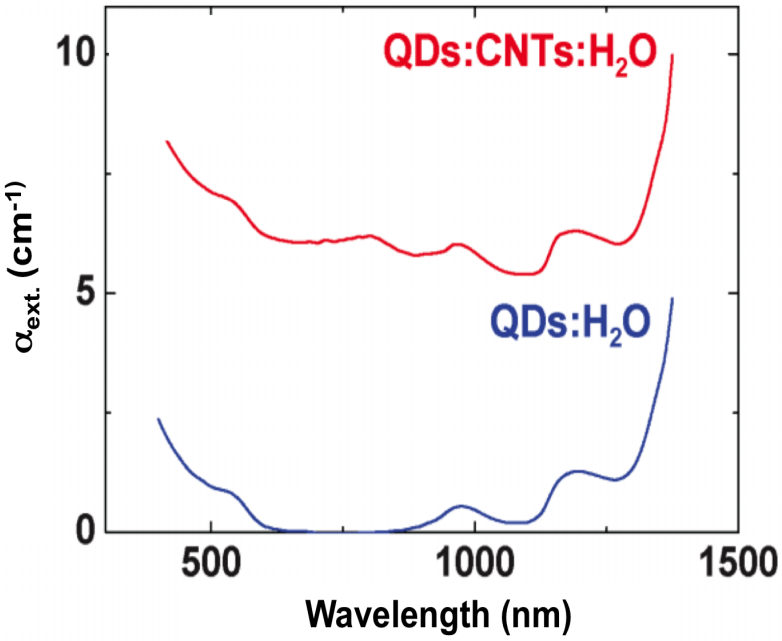

Figure 4.6: Absorption spectrum of an aqueous solution containing CdTe-QD in the presence and absence of CNTs in distilled water at room temperature.

The absorption spectrum of an aqueous solution of CdTe QDs is also included in figure 4.6. The presence of CNTs can be observed to exhibit a significant increase in the optical absorption of the solution throughout the visible to NIR region. This is in agreement with CNT absorption behaviour previously reported that indicated a broad absorption band extending from the visible to the NIR [222]. With particular reference to 1090 nm, the presence of CNTs significantly increases the absorption coefficient from 0.21 cm^{-1} to 5.3 cm^{-1}. This 20-fold increment can be attributed not only to the absorption of CNTs in this spectral window but also to the scattering of light induced by CNTs. Therefore, at 1090 nm, the laser-induced thermal loading of the fluid within the microchannel is expected to be significantly enhanced due to the presence of CNTs. Experimental observations corroborate this estimate. Figure 4.7 shows the microchannel temperature measured at the closest point to the waveguide indicated

by point A in figure 4.1, in the presence and absence of CNTs. It is important to note that in both cases a linear relation was observed, in agreement with equation 4.3. The heating rate was found to be as high as $(\frac{\Delta T}{\Delta P_{in}})_{1090nm,CNT} = 160\ ^oC/W^{-1}$ in

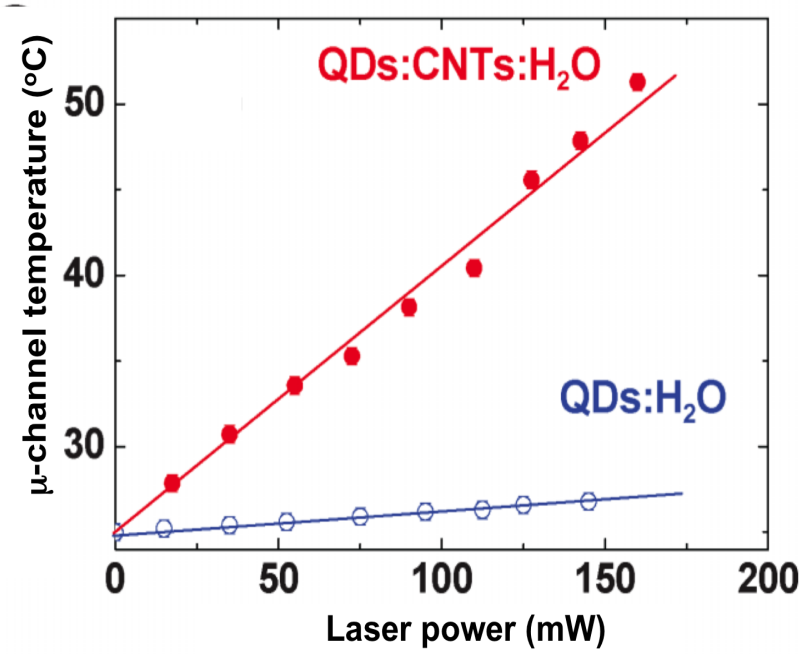

Figure 4.7: The local temperature at point A (see figure 4.1) as a function of 1090 nm laser power delivered to the microchannel in the presence of CNTs in H_2O_{di}. Data obtained for the same solution in the absence of CNTs is also included as a comparison.The maximum observed error in this dataset both in temperature and laser power is represented by the diameter of the data points. The experiment was repeated 5 times.

the presence of CNT. This is a 10-fold increase from the heating rate found in pure water in the absence of CNT for the same illumination wavelength. By combining the experimentally obtained heating rate with equation 4.3, it is possible to estimate the absorption coefficient of CNT at 1090 nm. Calculations revealed α_{abs} at 1090 nm in the presence of CNT to be $\approx 2.4\ cm^{-1}$. However, the absorption coefficient at this wavelength *i.e.* α_{ext} at 1090 nm in the presence of CNT is $\approx 5.3\ cm^{-1}$ as can be observed from figure 4.6. This comparison reveals a pronounced scattering contribution amounting to $\gtrapprox 50$ % of the absorption coefficient of CNT at 1090 nm. This is in agreement with appreciable relative scattering contributions to the extinction

coefficient that have been observed for other heating nanoparticles such as gold nanorods [223]. Therefore, it is evident that even at a low absorption wavelength of 1090 nm, using moderate laser powers of $\approx$ 150 mW, the presence of CNT can induce intra-channel temperatures to rise well above the threshold required for targeted cell hyperthermia ($\geq 45^oC$).

The possible presence of thermal hysteresis was also investigated with respect to the fluid containing CNT. The difference between the heating and cooling curve was found to be minimal as can be observed in figure 4.8.

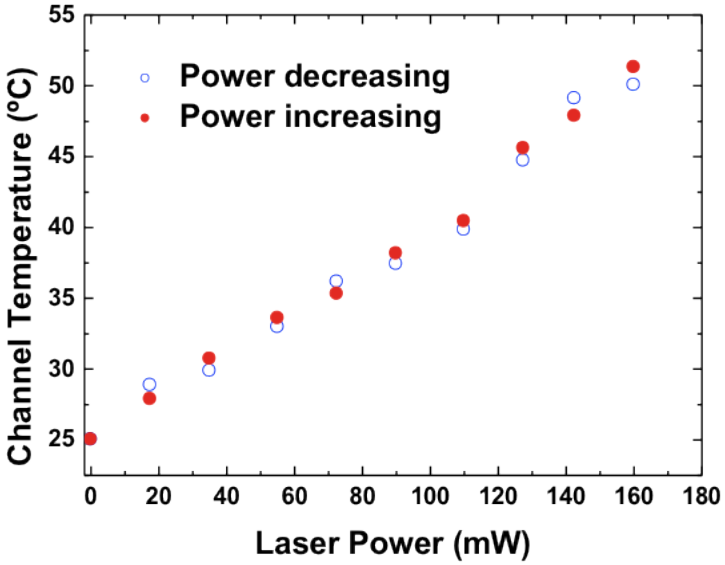

Figure 4.8: Local temperature at point A (see figure 4.1). as a function of 1090 nm laser delivered power when the microchannel was filled with an aqueous solution containing CNTs. Data obtained for the cases while the laser power was increasing and decreasing are included. The maximum observed error in this dataset both in temperature and laser power is represented by the diameter of the data points. The experiment was repeated 5 times. At 120 ^oC, the discontinuity can be attributed to shifts in $\lambda_{emission}$ of the CdTe QDs with temperature due to small changes in the QD size due to dilatation. The QDs are not bare but surrounded by a polymer to make them dispersible. Therefore, the small changes could arise from structural changes in the polymer that affect the final size of the QDs.

In order to maximise the practical applicability of this technique, quantifiable data

pertaining to the maximum possible thermal heating within an optofluidic device must be associated with its distribution. This necessitates the acquisition of several thermal images of the microchannel in the presence of the laser radiation. The creation of such thermal images is achievable using the aforementioned QD based thermometry technique. In order to generate an image, the microchannel was scanned by translating the device mounted on the 10 nm resolution XY piezo-stage (PIHera^{TM} P-622.1CD) with respect to the 488 nm focus spot. At each point, the spectral position of CdTe QD emission peak was determined. The entire set of peak emission data was assimilated such that a fluorescence image of the microchannel was obtained in terms of emission shift. The fluorescence peak emission shift was subsequently translated into temperature units using the temperature coefficient of the CdTe QD fluorescence band, which was 0.35 $nm/^oC$. Figure 4.9 shows the spatio-thermal map of the microchannel filled with the CdTe QD and CNT solution showing the temperature variations, when 38 mW of 1090 nm radiation was launched into the microchannel.

Figure 4.9(a) reveals how the temperature of the fluid reaches a maximum value where the intra-channel photon density peaks along the propagation path of the laser radiation delivered by the waveguide. It is also possible to determine the heat affected zone from the thermal image. Figure 4.9(b) shows the microchannel temperature profile obtained along the dashed line indicated in the thermal image of figure 4.9(a). From the profile, it can be observed that although the 1090 nm laser beam is expected to be localised within the microchannel, the temperature variation extends over tens of microns, due to the presence of heat diffusion processes. In addition to the determination of the heat-affected zone, the temperature profile also reflects the thermal and spatial resolution achieved using this on-chip thermometry method. It is important to note that temperature oscillations attributed to noise i.e. thermal uncertainty is well below 0.2 ^oC, constituting an outstanding thermal sensitivity.

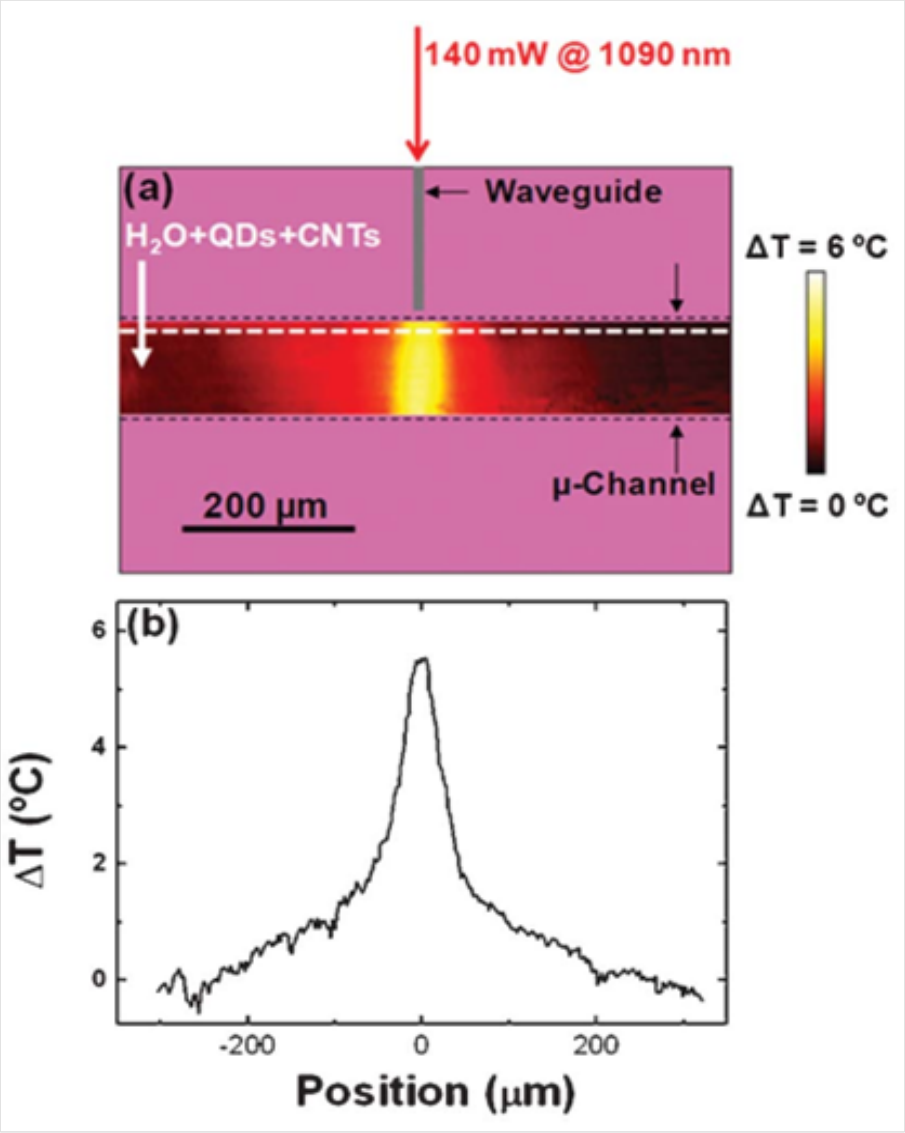

Figure 4.9: (a) Thermal image of a microchannel filled with an aqueous solution of CdTe QD and CNT when optically excited at 1090 *nm*. The laser power reaching the microchannel was 38 mW. (b) Thermal profile obtained along the horizontal scan-path indicated by the dashed line in part (a).

4.4 Conclusions and Future outlook

The potential for widespread implementation of DLW micro-devices in LoC applications is underpinned by its monolithic integration capability. The work undertaken in this chapter applied the exceptional spectral properties of nano-scale materials towards developing an integrated optofluidic remote thermometry device. The aspects pertaining to the chromatic dependence of CNT and CdTe QD within an aqueous microenvironment were investigated and the knowledge gained was applied to generate spatio-thermal maps of microchannels with high resolution. There is scope to improve the spatial resolution of the thermal images by optimising the device design to enable the use of higher NA focusing objectives in the confocal setup. Furthermore, the errors in temperature measurements can be reduced by applying non-polymer based coatings on the QDs. Based on previous work undertaken using fluorescent organic dyes, an authoritative comparison between dyes and QDs is reported in the work of Ute Resch Genger *et al.* [213]. In this work, the authors conclude that it is not possible to determine if the toxicity of QDs is lower than that of dyes. Therefore, from a cytotoxicity perspective, an improvement cannot be claimed if organic dyes are substituted by QDs. However, there are reports of surface functionalising the QDs that may result in reduced toxicity [211]. Moreover, a recent report on the application of photoluminescent functionalised carbon dots as temperature probes offers a promising alternative to metal ion based quantum dots [224].

There are several exciting possibilities to extend the functionality of the thermometry device developed in this chapter. The design and fabrication can be broadened to incorporate multiple NIR waveguides optimised for guiding single or distinct wavelengths of light to investigate the effects in the microfluidic channel. The data obtained from light-induced thermal effects in aqueous environments can be expanded to examine the analogous effects in standard cell culture media. The spatio-thermal maps of microchannels can also be generated for situations involving fluid flow. The methods of temperature elevation applied in this work can be complemented with relevant heat exchanger mechanisms such as convective or conductive fluid transfer and endothermic chemical reactions with an aim to achieve accurate temperature regulation that can be applied to *in vitro* cell culture applications. This will allow the application of the nanothermometry technique in biosensing applications where the accurate control of the

microenvironmental temperature can be achieved. Furthermore, DLW optofluidic devices with waveguide enabled trapping capability can also be used in conjunction with real-time temperature monitoring to characterise the thermal response in single-cells, with the possibility to compare normal cells with tumour cells, which can potentially provide new data for diagnostic applications.

Relevant publications

1. D. Choudhury, D. Jaque, A. Rodenas, W. T. Ramsay, L. Paterson, and A. K. Kar, "Quantum dot enabled thermal imaging of optofluidic devices," Lab on a Chip 12, 2414–2420 (2012).
2. D. Choudhury, D. Jaque, A. Rodenas, W. T. Ramsay, L. Paterson, and A. K. Kar, "Quantum dot thermal imaging of on-chip laser excited microfluidics," CLEO: Science and Innovations, paper JTh2A.7 (2012).

Contributions

D. Choudhury designed and fabricated the remote thermometry device. W.T. Ramsay built the confocal microscopy setup. D. Choudhury and D. Jaque carried out the thermometry experiments using CdTe QDs and CNTs. A. Rodenas and D. Jaque carried out the spatio-thermal mapping experiment. D. Choudhury and D. Jaque analysed the data.

Chapter 5

Selective etching in yttrium aluminium garnet single crystals

The future growth of optofluidics depends upon exploring new materials with unique properties as suitable alternatives to existing substrate materials. New materials must be prudently selected based on, among other pre-requisites, well-characterised optical properties, chemical stability and availability before being suitably investigated for optimised microfabrication. An aspect of growing interest in optofluidics research pertains to the development of novel methods of controllably applying light to a micro-scale environment. In current biological or chemical analytical LoC devices, light is typically delivered into the device from bulky laser sources either using free-space optics or fibre-coupling methods. Applications that demand different wavelengths of light need additional sources that in turn increase the space and cost requirements. Light sources that can be integrated within the system are therefore, an essential requirement for the progress of optofluidics. Efforts to meet this requirement have so far been channelled towards the incorporation of efficient fluorescent species, such as Rhodamine 6G or its variants, in organic solutions that are confined within microfluidic channels suitably designed in various resonator configurations [37]. These methods are well-suited for the generation of visible wavelengths [225, 226], typically ranging between $\approx$ 560 - 600 nm. Recently, ultraviolet whispering gallery mode lasing has been demonstrated at 386.75 nm using a commercial near-UV laser dye in dimethyl sulfoxide (DMSO) within a coupled optofluidic ring resonator [227]. The 'on-chip' generation of dual wavelengths

of light has also been demonstrated using microfluidic dye lasers in collinear [225] as well as parallel geometries [228]. However, the wavelength tunability of microfluidic dye lasers is restricted by the emission wavelengths of the fluorescent dyes. Moreover, the toxicity aspects of the dyes cannot be trivialised especially with regard to cross-contamination in biological analysis involving delicate cells. The application of such lasers is yet to be achieved in the NIR region of the electromagnetic spectrum which constitutes an important wavelength window for biological and chemical analytics. Therefore the need for suitable alternative techniques for the 'on-chip' generation of multiple wavelengths of light remains open for research.

The work undertaken in this chapter addresses the aforementioned requirement by introducing solid-state optical gain media as an alternative class of materials that can potentially enable the 'on-chip' generation of light. Specifically, the chapter presents neodymium doped yttrium aluminium garnet (Nd:YAG) crystals as a substrate material where the DLW microfabrication of photonic as well as fluidic components can be accomplished. YAG is an acronym for the oxide $Y_3Al_5O_{12}$, which is a synthetic crystal known, for ≈50 years, to exhibit properties particularly favourable for high-power laser applications. Trivalent neodymium (Nd^{3+}) is a rare-earth ion which is used as a dopant by replacing similar sized yttrium (Y^{3+}) ions in the YAG lattice. The incorporation of rare-earth ions in stable host materials with robust physical properties allows the creation of excellent optical gain media for active lightwave applications. Section 5.1 provides a relevant summary of rare-earth doped solid-state optical gain media. Section 5.2 provides a brief overview of the important spectral and physical properties of the YAG material. The DLW micro-structuring process in Nd:YAG is presented in section 5.3, with sections 5.3.1 and 5.3.2 focusing on the laser writing and selective etching processes respectively. Section 5.4 discusses the origin of etching selectivity in DLW micro-structures in Nd:YAG. The two methods applied to establish the origin of etching selectivity *viz.* micro-luminescence and micro-Raman spectroscopy are discussed in sections 5.4.1 and 5.4.2 respectively. Finally, the concluding remarks and future prospects of the work presented in this chapter are discussed in section 5.5.

5.1 Rare-earth ions in dielectric hosts

The importance of transparent dielectric materials incorporating transition metal or rare-earth ions that exhibit optical gain is well-known in the field of photonics since the advent of solid state lasers. These remarkable materials typically consist of a 'host' medium doped with active rare-earth ions such as neodymium (Nd^{3+}), erbium (Er^{3+}), ytterbium (Yb^{3+}), bismuth (Bi^{+}), thulium (Tm^{3+}), holmium (Ho^{3+}). The energy levels of rare-earth ions typically comprise of the $4f$ or $5f$ inner-states (see figure 5.2) that are shielded from the lattice of the host material by the optically passive outer electrons constituting the nearest noble gas electronic configuration, resulting in narrow and intense absorption and emission lines [229]. This shielding effect minimises the effect of the host material lattice in determining the emission wavelengths, cross-sections and bandwidths [229]. A wide range of crystalline and glass materials can serve as host media including oxides, vanadates, fluorides, borates, silicates, phosphates and chalcogenides. Suitably pumped rare-earth ions are capable of emitting at a number of wavelengths spanning the visible and NIR regions, irrespective of the host dielectric media.

Table 5.1 summarises the emission wavelengths of important rare-earth ions along with relevant host materials [229, 230].

Table 5.1: Emission wavelengths of important rare-earth ions

Rare-earth ion	Host material	Emission wavelengths (nm)
Neodymium (Nd^{3+})	YAG, YVO_4, $YLiF_4$, silica	1049, 1064, 900-950, 1320-1350
Ytterbium (Yb^{3+})	YAG, KGW, KYW silica	1000-1100
Erbium (Er^{3+})	YAG, silica	1550, 2700, 550
Thulium (Tm^{3+})	YAG, silica, fluorides	1700-2100, 1450-1530, 480, 800
Holmium (Ho^{3+})	YAG, $YLiF_4$, silica	2100, 2800-2900
Praseodymium (Pr^{3+})	silica, fluorides	1300, 635, 600, 520, 490
Bismuth (Bi^{+})	silica, borates	1300

YAG - Yttrium Aluminium Garnet ($Y_3Al_5O_{12}$)
KGW - Potassium Gadolinium Tungstate ($KGd(WO_4)_2$
KYW - Potassium Yttrium Tungstate ($KY(WO_4)_2$

The technique of DLW has been thoroughly applied in rare-earth doped materials towards the development of active waveguide based devices. Knowledge from initial demonstration of internal gain in active waveguides [231] was developed into waveguide

amplifiers [232, 233] and eventually active waveguide based compact continuous wave and modelocked lasers in various materials [146, 148, 149, 234–236]. Although rare-earth doped materials have been extensively studied with respect to active photonic applications, the potential to incorporate these materials within LoC environments has not yet been explored. In this context, the DLW technology is uniquely placed, due to its applicability to a diverse array of materials. With regard to this chapter, section 5.2 highlights the properties of Nd:YAG as a potential 'optically active' material for LoC applications. Figure 5.1 provides a conceptual diagram of an integrated optofluidic device in YAG. The figure illustrates a potential method of incorporating a DLW optical waveguide in a rare-earth ion doped YAG host. The waveguide can be aligned orthogonal to a selectively etched microchannel which when flanked by two 3D photonic crystal structures can form a cavity that can be tuned to a specific wavelength of interest. As described later in the chapter, the selectivity in the wet etching of YAG crystals has been observed to be much higher than that known for fused silica. Furthermore, during the course of this work, the possibility to etch millimetre long channels with uniform sub-micron cross-section was revealed. This capability in YAG has not been observed in any other material and can potentially enable its use in performing comparative nuclear deformation studies between healthy and diseased cells [199].

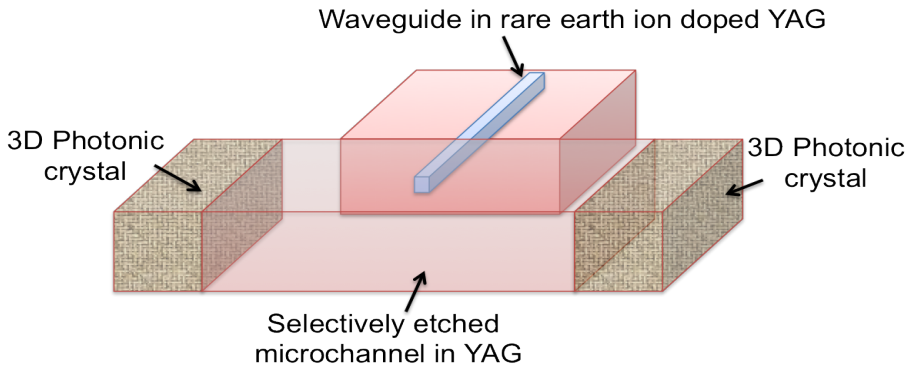

Figure 5.1: Conceptual illustration of an integrated optofluidic device in YAG. The device can potentially be monolithically integrated in a single YAG substrate using DLW.

5.2 Relevance of Nd:YAG for LoC applications

Within the broad spectrum of materials that exhibit optical gain properties, Nd:YAG is well-characterised in terms of its spectral and physical properties with a proven capability in translating intrinsic light-matter interactions into practical applications. The trivalent Nd^{3+} ions, with a typical doping level of ≈1 atomic %, exhibits a 4-level energy transition scheme as depicted in figure 5.2.

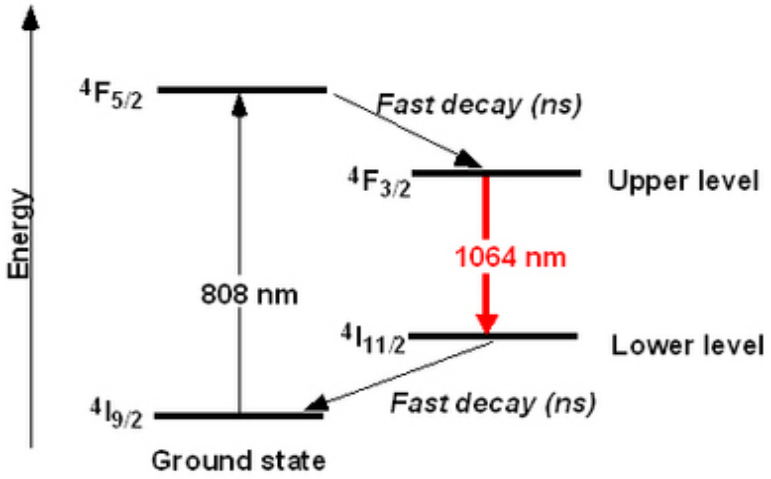

Figure 5.2: Simplified energy level diagram for Nd:YAG [237]

In addition to the principal absorption at 808 *nm* schematically illustrated in figure 5.2, Nd^{3+} exhibits additional absorption bands that occur at 520 *nm*, 580 *nm* and 730 *nm* [229]. Absorption at 808 *nm* typically exhibits a rapid non-radiative decay from the $^4F_{\frac{5}{2}}$ to the intermediate $^4F_{\frac{3}{2}}$ Stark energy level. Stimulated emission occurs *via* a strong radiative transition to the $^4I_{\frac{11}{2}}$. Subsequently, the rapid non-radiative decay to the lower energy state at $^4I_{\frac{9}{2}}$ occurs. Absorption at more energetic wavelengths is associated with higher energy levels that progressively undergo non-radiative decay to the $^4F_{\frac{3}{2}}$ state, creating the 4-level system [229]. DLW has been successfully applied to achieve optical waveguiding optimised for 1064 *nm* in Nd:YAG crystalline substrates using double-line and depressed cladding fabrication methodologies [238, 239]. The waveguide regions revealed refractive index steps $\sim 10^{-4}$ and exhibited low propagation

losses $\leqslant 0.4\ dB\ cm^{-1}$, which is essential for device based applications. In addition, DLW waveguides have also been fabricated in Nd:YAG ceramics using the double-line approach [135]. In this case, a permanent refractive index decrease $\sim 10^{-2}$ was observed at the cores of the laser modified regions. Defect states were found to exist around the cores which could be minimised by annealing the substrate at temperatures $\approx 600\ ^oC$. In addition, the presence of stress-induced increase in refractive index $\sim 10^{-3}$ was also observed in-between the double lines, which was analysed to be the principal guiding contribution [135].

These observations underscore the relevance of Nd:YAG in applications where low-loss waveguiding is important. However, the waveguiding capability of Nd:YAG only partially fulfils the integration criterion in LoC devices. The fabrication of high-quality microfluidic channels in the same Nd:YAG substrate is also essential to realise monolithically integrated devices. Section 5.3 in this chapter addresses the latter requirement by demonstrating selective chemical etching in DLW structures in Nd:YAG. This demonstration highlights the potential for integrating photonic and fluidic components in a single substrate that is capable of exhibiting optical gain.

5.3 DLW enabled 3D microstructuring in Nd:YAG crystals

The DLW technique along with subsequent selective etching methods have so far been predominantly applied in glasses. In comparison, it has been difficult to develop analogous applications of the technique in crystalline dielectrics. There are experimental reports involving the wet etching in fs laser processed $\sim \mu m$ sized features in crystals such as quartz [240], sapphire [241] and lithium niobate [242]. However, these demonstrations of selective etching in DLW microstructures have not yet been translated to the fabrication of microfluidic devices or 3D functional microstructures inside crystals. In comparison with glasses, the long range order in crystals is highly responsive to the parameters associated with DLW such as pulse polarisation, pulse energy, translation speed and repetition rate. It is possible to identify a narrow parameter 'window' within which the DLW process can be applied to crystalline substrates, beyond which the crystal is susceptible to damage and cracking from the tightly focused fs laser

pulses.

5.3.1 DLW in YAG crystals

A commercially obtained Nd:YAG crystal (Altechna) with a flatness of $\leqslant \lambda/10$ at 632 nm was used for this work. The crystal had a Nd^{3+} ion doping concentration 1.1 atomic %. A 10 $mm \times 10\,mm \times 1\,mm$ wafer was diced into 1 $mm \times 10\,mm \times 1\,mm$ substrates for experimentation. DLW was performed in the transverse writing geometry using the variable repetition-rate Yb-doped master oscillator power amplifier laser system (IMRA μJewel D400) described in chapter 2. Using equation 2.2, the adiabatic parameter (γ) was evaluated to be $\gamma \sim 0.3$ indicating that the energy transfer mechanisms are a combination of multiphoton and tunnelling effects. The experimental setup is the same as that described in section 2.5. The variable compressor was set to deliver 460 fs pulses. Initial DLW parameter acquisition experiments were performed at a pulse repetition-rate of 100 kHz. This repetition rate was selected based on earlier reports on the fabrication of localised 3D refractive-index increased zones in YAG crystals [243]. The fs pulses were focused within the Nd:YAG substrate using a 0.4 NA aspheric lens. Circular polarisation was applied throughout the laser writing process in order to decouple the pulse polarisation from the orientation of the crystallographic axis. Planar structures were written at a depth of 100 μm from the top surface of the crystal using the multiscan technique, which is described in section 2.6.2. The translation speeds applied in the 100 kHz experiment ranged between 8 $mm\ s^{-1}$ and 1 $mm\ s^{-1}$ while the pulse energy was maintained at values $\leqslant$ 300 nJ. The design was programmed with 30 scans, with each scan laterally offset by 1 μm constructing a 30 μm planar structure. Severe damage and cracking within the crystal was however found as a result of scanning large areas with a high density of modified zones. This fundamental limitation had also been previously observed in Nd:YAG when high-density 3D photonic structures were written at a repetition rate of 1 kHz [244]. Increasing the repetition rate to 500 kHz alleviated this limitation. This can be attributed to heat accumulation associated with higher repetition rates, which relaxes the stress fields generated between modified and unmodified zones [105]. In the 500 kHz regime, the 30 μm planar structures written at a depth of 100 μm from the top surface revealed lower damage and cracking at pulse energy values $\lessapprox$ 200 nJ at translation speeds above 4 $mm\ s^{-1}$. A parameter

window was successfully obtained for damage free DLW between pulse energy values of 170 nJ and 160 nJ at a translation speed of 8 $mm\ s^{-1}$. Figure 5.3 shows an optical transmission cross-sectional view of a 30 μm planar structure before wet etching.

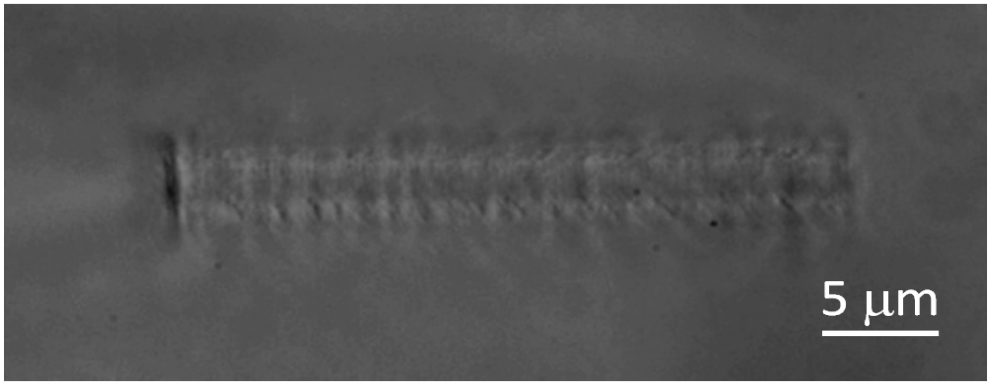

Figure 5.3: Cross-sectional view of DLW planar microstructure in Nd:YAG

These parameters subsequently enabled 3D contour designs to be implemented in writing rectangular cross-section microstructures deep inside the Nd:YAG substrate. In the contour design approach, the laser focus was programmed to write the perimeter of a cuboidal microchannel with a cross-section of 100 μm × 100 μm and a length of 1 mm. The cuboidal structure was opted for as it is a simple design to implement and the etching performance can be directly compared with similar structures in fused silica. The top and bottom layers of the microchannel were written using the multi-scan technique with a scan-offset of 1 μm. The perimeter around the volume of the microchannel was written using planar rectangular scans starting at the bottom surface and incrementally constructed an offset opposite to the beam propagation direction of 1 μm, until the top surface was reached. The top surface of the microchannel was designed at a depth of 145 μm from the top surface of the Nd:YAG substrate. Figure 5.4 shows an optical transmission image of the cross-section of the cuboidal microchannel before etching. Using the contour modification approach, laser writing times of under 10-minutes per microchannel was achieved.

5.3.2 Selective etching in YAG crystals

The DLW microstructures were ground and polished to reveal the facets and subsequently wet etched using an aqueous solution of orthophosphoric acid (H_3PO_4) with

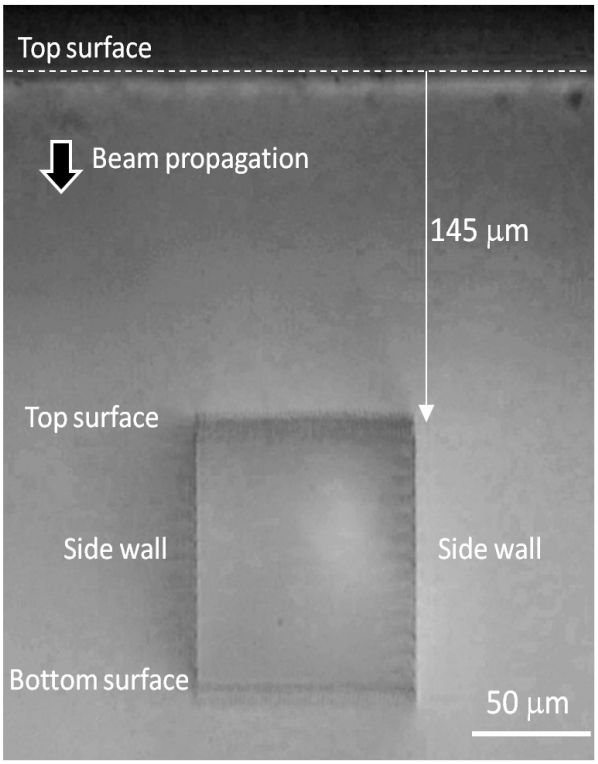

Figure 5.4: Cross-sectional view of DLW cuboidal microchannel in Nd:YAG

a maximum concentration of 50 % (w/w) at an elevated temperature of 90 ^oC, which is well below 158 ^oC, the boiling point of the acid. During etching, gentle agitation of the etchant solution was performed using a magnetic stirrer. The laser modified regions in the cuboidal microchannels were completely removed after 30 hours, leaving behind hollow geometrical regions inside the Nd:YAG substrates. Figure 5.5 is an optical transmission image showing a partially etched planar DLW structure. The etch profile shows remarkable uniformity across the cross section of the structure.

Figure 5.6 shows a scanning electron microscope (SEM) image of an etched cuboidal microchannel. Excellent optical quality surface roughness was observed in the unmodified crystal even after prolonged etchant exposure.

Prior to imaging and further analysis of the selectively etched microstructures, the substrate was cleaned using H_2O_{di} and acetone.

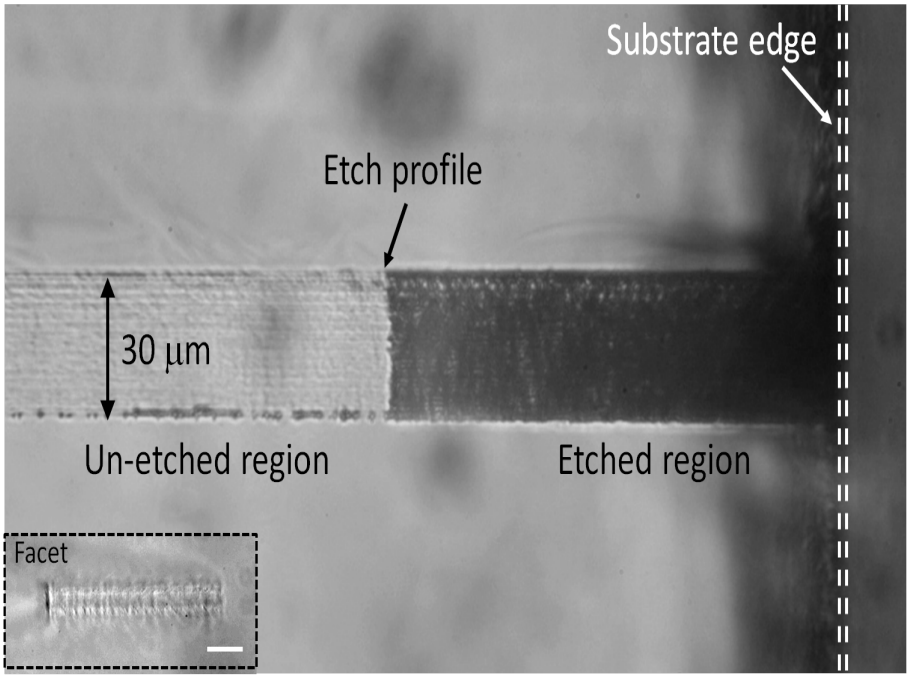

Figure 5.5: Top view of a partially etched DLW planar structure in Nd:YAG. Inset: The facet of the 30 μm planar structure before etching. The scale bar represents 5 μm.

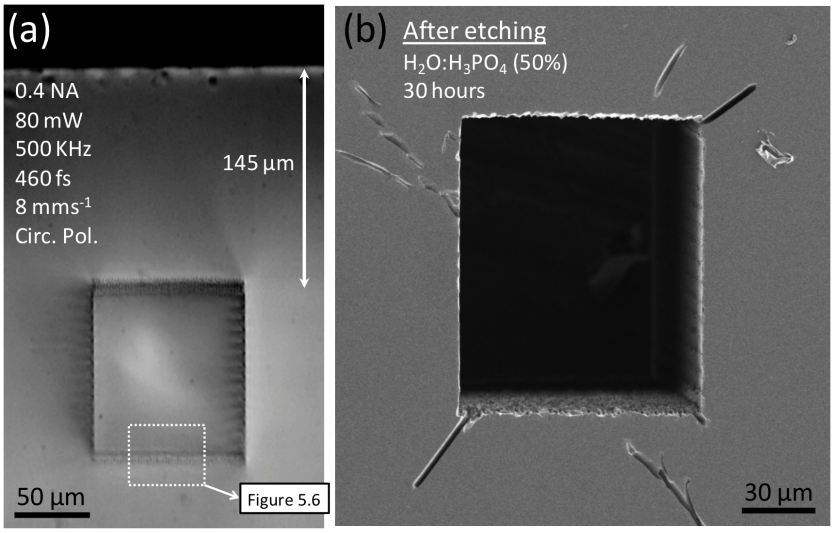

Figure 5.6: Cuboidal microchannel in Nd:YAG single crystal. (a) DLW contour modified microstructure. The writing parameters are shown. Inset also shows the area selected for performing an analysis into the origin of etching selectivity. This region is examined in Figure 5.7. (b) SEM image of the cuboidal microchannel after being etched in H_3PO_4 for 30 hours.

5.4 The origin of etching selectivity

Post-etch, the microchannels showed a remarkable selectivity that is clearly more enhanced compared to similar structures written in fused silica and etched using dilute HF. The surface roughness of the bulk, unmodified regions of the crystal showed negligible increase after etching, as is evident from the SEM image shown in figure 5.6. In order to investigate the origins of this etching selectivity, confocal micro-luminescence and micro-Raman spectroscopic studies were performed on the laser modified region shown in the inset in figure 5.6. These investigations are discussed in sections 5.4.1 and 5.4.2 respectively.

5.4.1 Micro-photoluminescence

Confocal micro-luminescence imaging of the pre-etched structures was performed in order to analyse the origin of the highly selective etching process observed. In doing so, the Nd^{3+} luminescence was optically excited using a 785 nm linearly polarised continuous wave laser beam focused into the selected region using 50× 0.75 NA Leica microscope objective, which was mounted on a Renishaw inVia Reflex Raman Leica microscope. The same objective was used to collect the back-scattered luminescence which, after passing through appropriate filters and confocal apertures was spectrally analysed using a high resolution spectrometer. Data processing was performed using the WiRE 3.2 Renishaw software. Figure 5.7 shows the selected region for micro-luminescence analysis of the laser written microstructure as indicated in figure 5.6. Figure 5.7(b) shows a map of the emission integrated area (EIA) of the ${}^4F_{\frac{3}{2}} \longrightarrow {}^4I_{\frac{9}{2}}$ emission line at $\approx$ 938 nm. This transition was selected as it is spectrally isolated from the other four sub-Stark transitions in the Nd^{3+} spectrum [245]. A decrease in EIA is suggestive of the a negative change in refractive index. Clearly, from figure 5.7(b), the EIA remains practically unchanged inside the modified regions. This effect is characteristic of positive index modification and differs from previous reports on DLW structures in Nd:YAG ceramics where refractive-index decrements were observed as a result of lattice amorphisation [135]. The absence of a relevant reduction in luminescence at the irradiated volume is a clear indication that severe lattice damage has not resulted from the DLW process. Figure 5.7(c) depicts a slight red-shift of the emission line in the laser-modified region in comparison with the bulk crystal. Red

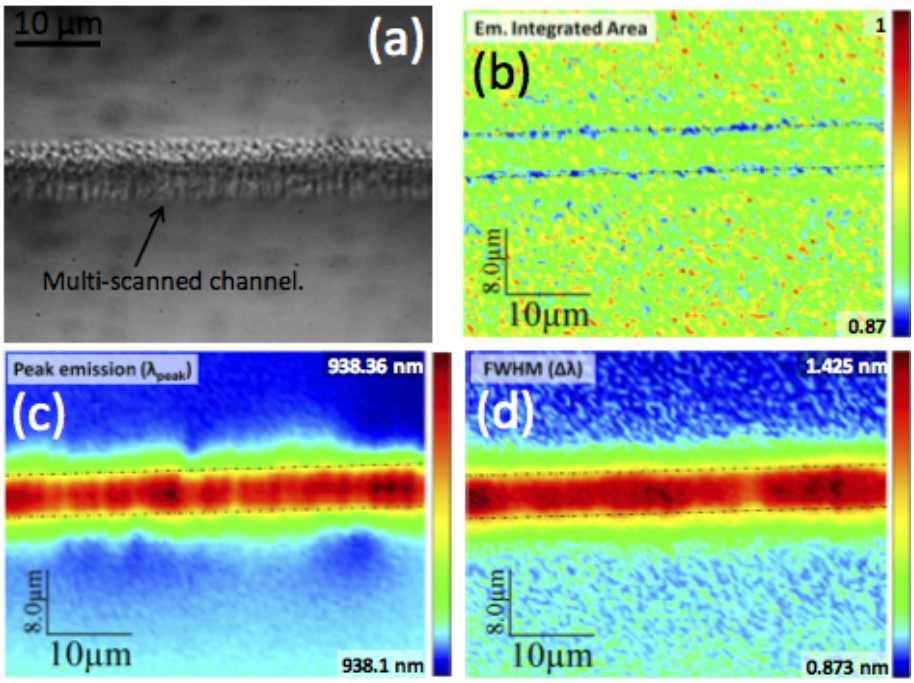

Figure 5.7: Confocal micro-luminescence imaging of DLW structure in Nd:YAG. (a) The selected region for micro-luminescence analysis of the laser written microstructure as indicated in figure 5.6. (b) Emission integrated area map (c) Peak emission map (d) Peak linewidth map.

shift in the emission line is typically attributed to a change in the energy splitting of both the ${}^4F_{\frac{3}{2}}$ and ${}^4I_{\frac{9}{2}}$ Stark states [246]. A measure of this energy split provides a quantification of the crystalline field in the vicinity of the Nd^{3+} ions. Thus the observed red shift indicates an alteration in the Nd^{3+} ions' crystalline environment. Within a first order approximation, this red shift is also indicative of presence of a local lattice compression [135]. Finally, figure 5.7(d) shows a marked broadening of the emission peak in the laser modified region, with an increase of 60 % in the full width at half maximum (FWHM). Such broadening of the emission line is suggestive of the presence of disorder arising from the presence of lattice defects and imperfections. In this case, it can be concluded that focused fs pulse irradiation has resulted in a remarkable increase in the local lattice disorder. Therefore, from the micro-luminescence imaging analysis of the irradiated areas included in figure 5.7, it can be concluded that fs irradiation has induced the Nd:YAG network into a 'pre-damaged' state, characterised by a bond distortion and a certain degree of disorder.

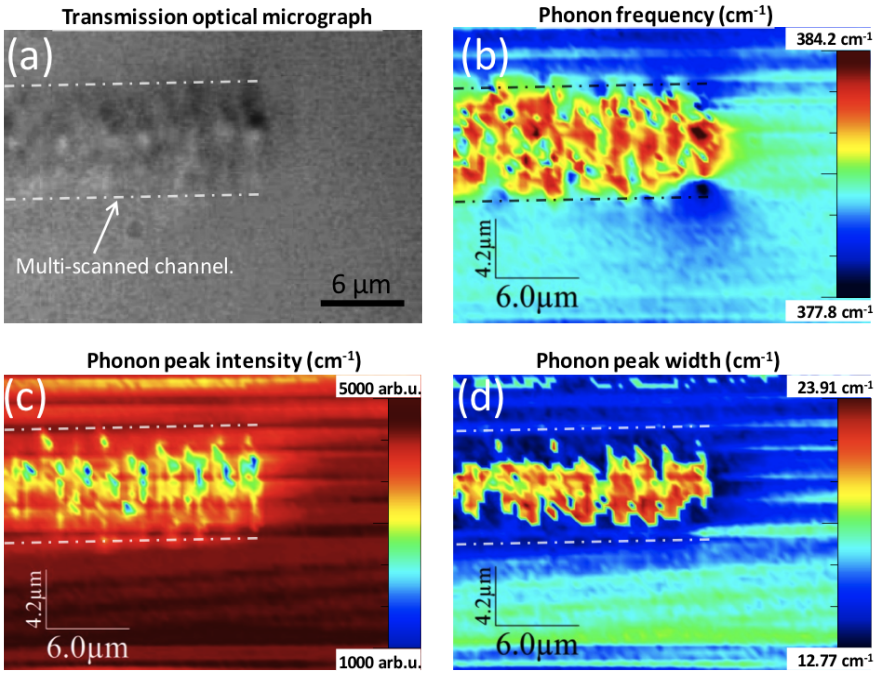

Figure 5.8: Confocal micro-Raman imaging of the DLW structure in Nd:YAG. (a) The selected region for micro-Raman analysis of the laser written multiscan microstructure. (b) Phonon frequency map (c) Phonon peak intensity map (d) Phonon peak width map.

5.4.2 Confocal Raman spectroscopy

The presence of a pre-damage state was further corroborated using micro-Raman spectroscopic measurements. These measurements involved the use of a 514 nm linearly polarised continuous wave laser beam for excitation. A 100 × 1.4 NA Nikon objective was used to achieve sub-micron spatial resolution for the experiments [135]. Figure 5.8(a) shows the multiscan region selected for performing the Raman analysis. Figure 5.8(b) shows spatial variation of the peak frequency over the selected region. The peak intensity and width of the $\sim 378\ cm^{-1}$ characteristic T2g(7) phonon Raman mode of the YAG network as obtained over the fs irradiated region are shown in figures 5.8(c) and 5.8(d) respectively.

As can be observed in the irradiated region, the Raman mode undergoes a blue shift and simultaneous broadening. These two observations indicate the presence of a local lattice distortion and partial disorder in the Nd:YAG network. Both observations were also concluded from the micro-luminescence data shown in figure 5.7. Furthermore, the

Raman peak intensity is observed to undergo a slight reduction, at localised volumes as can be seen in figure 5.8(c). This observation further supports the explanation of partial damage in the Nd:YAG network. Therefore, analysis of both micro-Raman and micro-luminescence data have led to the conclusion that the DLW irradiation conditions used in this work have driven the Nd:YAG network into a pre-damaged state. Based on this, it can be stated that the highly selective etching process observed in the DLW regions can be a direct consequence of bonds being reoriented in or close to the non-elastic range as a result of their interaction with the ultrashort pulses. These bonds are therefore easier to break and exhibit a higher reactivity to new species compared to the bulk material.

5.5 Conclusions and Future outlook

The work undertaken in this chapter demonstrated the DLW microfabrication of hollow, embedded, geometrical structures in Nd:YAG laser crystals. Highly selective wet etching of the DLW refractive-index increased 3D microstructures is reported. The experimental conditions pertaining to the laser writing and wet etching procedures leading to damage-free fabrication of micro-channels were determined. Structural images obtained by both micro-luminescence and micro-Raman studies of the fs laser irradiated volumes have been used to elucidate the possible origin of the etching selectivity. This work reveals the possibility to concurrently fabricate ultra high aspect-ratio fluidic channels within the volume of a laser crystal, a finding that can be instrumental in developing future biophotonic sensing technologies. This chapter presented the first demonstration of microfluidics in a laser gain medium. Within the context of optofluidic devices for biophotonic applications, Nd:YAG offers the choice of different operating wavelengths. However, careful optimisation is necessary in order to access other Nd:YAG emission lines by suppressing the strong 1064 nm emission. There is also scope to reduce the etching time further by using different combinations of concentrations and temperature of the etchant solution. Moreover, the surface roughness of the inner walls of the etched microchannels must be measured and appropriately minimised to reduce erroneous scattering of waveguide illumination from these walls. The highly selective etching also creates the opportunity for nanofluidic applications in optical gain media.

There is promising scope for future development of this work. The parameter space within which damage-free DLW occurs can be expanded by probing higher repetition rates and shorter pulses. The dependence of selective etching on the polarisation of the fs laser pulses need to be investigated. The indications of positive refractive index change from the micro-luminescence data in this work can be investigated in greater detail to obtain parameters to fabricate Type-I optical waveguides in the Nd:YAG material, in which only depressed cladding and double-line stress-induced have been demonstrated so far. Furthermore, the work can be extended to other rare-earth ion doped YAG crystals, such as Cr^{4+}, Ce^{3+} along with those listed in table 5.1. The ultra-high selectivity observed in this material can potentially be implemented in the manipulation of biological entities much smaller than mammalian cells using nanofluidic channels. This work underscores the potential to advance the DLW technology with respect to LoC device fabrication from its state-of-the-art to active optofluidic devices that exhibit higher levels of integration.

Relevant publications

1. D. Choudhury, A. Rodenas, L. Paterson, D. Jaque and A.K. Kar, "Three-dimensional micro-structuring of yttrium aluminum garnet crystals by direct laser writing and wet chemical etching," Applied Physics Letters (manuscript in preparation).
2. D. Choudhury, A. Rodenas, L. Paterson, D. Jaque and A.K. Kar, "3D μ-fabrication in YAG crystals by direct laser writing and chemical etching," submitted to CLEO Pacific Rim (2013).

Contributions

D. Choudhury performed the laser writing and selective etching experiments. A. Rodenas carried out the micro-luminescence and micro-Raman analysis.

Chapter 6

Conclusions and Future Prospects

6.1 Conclusions

The ability for the concurrent 3D fabrication of optical waveguides and selectively etched embedded microfluidic channels in transparent dielectric materials forms the principal asset of DLW with respect to optofluidic devices. The work embodied in this thesis presents illustrative DLW microsystems in which the unique fabrication capabilities of the technology have been unified to achieve maximal componential control over complex device geometries and functionalities. The work further demonstrates the potential of the technology in making important and unprecedented contributions to the development of LoC devices. A summary of the work presented in each chapter is provided as follows.

6.1.1 Deformability based cell sorting

Chapter 3 presented a deformability based cell separator device involving a network of selectively etched high aspect-ratio microchannels. Polarisation sensitive etching phenomenon of DLW strcutures in fused silica was optimised to produce microchannels with cross-section narrower than the average size of target cells. Devices featuring a single constriction and a 2D array of constrictions (see figure 3.8) were successfully fabricated and applied to evaluate the performance characteristics of mode of separation. The controlled etching procedures applied during the laser writing process ensured that the microchannels preserved their aspect-ratio after etching in dilute HF. HL60

cells with an average cell diameter of 11.7 μm $\pm$ 1.1 μm were used to examine the performance of the device with a maximum constriction width of 8μm. The device was capable of withstanding high throughputs with flow-rates $\leqslant$ 167 μL min^{-1} and exhibited $\gtrapprox$ 80 % viability in the output cell population.

6.1.2 Thermal imaging in DLW optofluidic devices

Chapter 4 applied DLW in the fabrication of an optofluidic device in fused silica to enable the remote measurement of temperature within the localised environments of microfluidic channels. For this purpose, the thermal dependence of spectral emission of semiconductor nanocrystals (CdTe-QD) were applied. The device comprised of a single microchannel with a cross-section of 100 μm $\times$ 100 μm and a length of 5 mm, illuminated using a monolithically integrated NIR waveguide with a cross-section of 8 μm $\times$ 8 μm that was orthogonally aligned to the microchannel (see figure 4.1). The spectral dependence of temperature within the microchannel filled with an aqueous suspension of the CdTe-QD was investigated by measuring the shift in peak emission at 980 nm and 1090 nm illumination wavelengths. Furthermore, the effects of incorporating CNT as efficient heat-absorbing nanoparticles within the aqueous environment of the microchannel were analysed. Using 980 nm illumination, temperature increment (ΔT) of 10 ^oC was observed which climbed to 20 ^oC in the presence of absorbing particles despite using 1090 nm illumination at which water absorption is comparatively lower. Temperatures achieved were well in excess of 45 ^oC, which is recognised as the threshold temperature for applications such as targeted cell hyperthermia. Spatio-thermal maps of the microchannel were produced, revealing thermal resolutions of $\approx$ 0.1 ^oC.

6.1.3 Selective etching in DLW microstructures in Nd:YAG

Chapter 5 introduced the well-known laser crystal Nd:YAG as a potential alternative material for LoC optofluidic applications. DLW of damage-free contour modified microstructures was achieved in Nd:YAG (see figure 5.4), which were subsequently etched using a aqueous solution of H_3PO_4 at 50 % dilution revealing exceptionally high selectivity in the etching performance. The unmodified Nd:YAG material was found to maintain high surface quality even after prolonged exposure to the etchant solution at an elevated temperature of 90 ^oC. The selectivity is significantly more pronounced

in comparison with analogous DLW structures etched using dilute HF in fused silica. The origin of the high etching selectivity observed in DLW microstructures in Nd:YAG was examined using micro-luminescence analysis of the ${}^4F_{\frac{3}{2}} \longrightarrow {}^4I_{\frac{9}{2}}$ emission line at $\approx 938\ nm$ in Nd^{3+} ions. This study revealed the formation of a 'pre-damage' state in the fs laser modified regions as the basis of etching selectivity. This inference was further corroborated by performing a micro-Raman spectroscopic analysis of the fs laser modified regions in Nd:YAG.

6.2 Future prospects

The work presented in this thesis highlights the advantages of DLW as a flexible technology that can be adapted to suit different applications. The work undertaken in each chapter underpins a strong scope for future development encompassing fundamental studies as well as practical applications. The future prospects relevant to each experimental chapter is discussed as follows.

6.2.1 Deformability based cell sorting

Design optimisation

The label-free cell separator can be optimised further based on the cross-linked channel design discussed in section 3.4. The design enables the parallel flow or contraflow scheme (see figure 3.15) between a heterogeneous cell population along one microchannel and growth media along a second microchannel. Optimised control over the pressure gradient along cross-linking constrictions can be achieved by performing theoretical simulations on both the flow-schemes and altering the design as required. There are two important factors that need optimisation in the current version of the device. These include the length of the constrictions and the average time that the cells remain in the deformed state. These factors are important to quantify as there may be applications that require that cells remain deformed for extended periods of time. Furthermore, the selective etching process can be optimised to ensure that the constrictions exhibit a uniform cross-section throughout their length. These optimisation steps can lead to a further increase in the number of viable cells in the device output.

Cytometric capability

The capability to count the number of cells at various stages of the sorting process is an important factor for any cell sorter device. This functionality can be added to *ver.3* of the device using DLW single-mode, NIR optical waveguides fabricated in a MZI arrangement at pre-determined positions of the device, ensuring a microchannel is aligned across the sensing arm of the interferometer. The movement of a cell across the sensing arm will result in a momentary change in refractive index causing a measurable shift in the interference pattern, thereby generating a fast and sensitive counter. The flow along the microchannels can be focused in the interferometer region using the characteristic tapering exhibited in the HF etching of fused silica. This optofluidic 'upgrade' will impart cytometric capability to the device with the potential for automation. Furthermore, the device can be rapidly prototyped taking advantage of the repeatable fabrication capability of DLW. Therefore, the feasibility to apply multiple devices in a cascaded arrangement can be evaluated with an aim to increase the efficiency of separation.

Applications

As discussed in section 3.4, the device design in *ver.3* can be optimised to meet the requirements for fractionating residual hPSC from differentiated populations, where the separation can be favourably influenced by the unique properties of the pluripotent cells. In addition to fractionating hPSC based on deformability, there are two important applications where the capabilities of DLW demonstrated in this work can be implemented. The device can be applied to enable the *in vitro* study of the mechanics of capillary transmigration of cancer cells [199], which is of particular interest in the cancer cell-biology studies. Selectively etched constrictions of appropriately sized cross-sections can be utilised to obtain insights into how cancer cells migrate from the primary site to new sites through the vascular system of the human body. Yet another application of the device can involve the evaluation of how healthy erythrocytes undergo a pronounced reduction in deformability as a result of malarial infection [247]. This creates the potential to separate diseased erythrocytes from uninfected cells. The healthy erythrocytes can also be sorted and subsequently processed for storage in a blood bank. The selective etching of DLW microstructures can be tailored to meet the smaller size requirements of deforming erythrocytes and enable the development of an

in vitro label-free method to potentially remove malarial cells from healthy cells.

6.2.2 Thermal imaging in DLW optofluidic devices

Design optimisation

The remote thermometry device presented in chapter 4 offers exciting scope for future development. The single waveguide device demonstrated in this work can be utilised to study the effects on thermal distribution in the case of non-zero flow-rates within the microchannel. The present version of the device can be multiplexed to incorporate a pre-determined number of appropriately spaced NIR waveguides to investigate the possibility of achieving uniformly distributed temperature along the length of the microchannel. The present design can also be extended to incorporate multiple optical waveguides wherein each waveguide is optimised for single-mode guiding of a distinct wavelength of light. The effects of simultaneous illumination of the aqueous microchannel environment using multiple wavelengths of light can be studied with an aim to achieve an 'on-demand' change of temperature with high spatial and thermal resolution. Furthermore, the compatibility of remote thermometry with appropriate convective or conductive heat exchanger mechanisms can also be investigated to achieve the regulation of temperature over long time-scales, *i.e.* $\sim$ several hours. These investigations can also be undertaken using relevant growth media to achieve more biologically representative results.

Applications

Temperature is an important factor that needs to be accurately controlled in the case of *in vitro* miniaturised cell-culture applications. These applications demand highly accurate control over physiological temperatures as well as the possibility to precisely control increments in temperature as and when required. The remote thermometry work can be developed with an aim for its implementation in such applications with particular emphasis on cells that are difficult to culture. Clearly this work needs to be developed in conjunction with methods to control other incubation conditions such as pH and partial pressures of CO_2. The controllable method of heat generation using the absorbing nanoparticles such as CNT or gold nanorods can also be applied to the study of targeted cell hyperthermia under *in vitro* settings. Yet another application of

the work involves the study of periodic heat-shock effects in pluripotent stem cells and the possibility to thermally induce their differentiation. There is evidence of enhanced osteogenesis as a result of temporary heat-shocks applied on human mesenchymal stem cells (hMSC) [248, 249]. However, this aspect of physically inducing stem cell differentiation has not been explored in depth and presents an exciting area to research using remote thermometry.

6.2.3 Selective etching in DLW microstructures in Nd:YAG

The work undertaken in chapter 5 offers excellent scope for further development. The phenomenon of selective etching in Nd:YAG can be investigated for possible dependencies on the polarisation of the writing pulses. In addition, the parameters applied for fabricating the multiscanned microchannels indicated a positive change in refractive index in comparison to the unmodified material. This fact highlights the potential of concurrently fabricating microchannels and *Type-I* DLW optical waveguides in Nd:YAG crystals using the same parameters. These parameters are different from *Type-I* waveguiding in the YAG matrix reported earlier [243], and present an interesting opportunity to compare and contrast waveguiding properties obtained using both parameter windows. The selective etching work can be expanded to examine the phenomenon in YAG matrices incorporating other rare-earth dopant ions. Various rare-earth dopants in the YAG matrix exhibit a range of emission wavelengths spanning the visible (Ce^{3+}) and NIR regions (*e.g.* Nd^{3+}, Er^{3+}, Yb^{3+}, Cr^{4+}) of the electromagnetic spectrum. Selective etching can be investigated in the presence of carefully selected dopants. Positive results obtained can potentially be combined with DLW optical waveguide fabrication in these materials thereby enabling an active optofluidic capability for a number of wavelengths significant for biological and chemical analytics. The extreme etching selectivity observed in Nd:YAG can also be implemented in the manipulation and isolation of biological cells or organisms much smaller than mammalian cells. In addition, the high etching selectivity in Nd:YAG structures can be exploited to enable the fabrication of ultra-high aspect ratio, nano-sized hollow structures using high numerical aperture focusing optics. This highlights the exciting potential to fabricate precisely oriented 2D or 3D arrays of periodic nano-structures with high refractive index contrast for photonic crystal applications.

DLW has evolved rapidly over the past 16 years from being a purely photonics oriented field into a multifaceted technology capable of making significant contributions to multidisciplinary fields. The future of DLW in developing next-generation optofluidic LoC applications is truly promising. The rapid development of optimised fabrication schemes for realising low-loss active and passive optical waveguides as well as fluidic features with increased selectivity in chemical etching will lead to the emergence of high-quality 2D and 3D optofluidic architectures. This is substantiated by the extremely encouraging results reported so far using this technology. Further development of DLW enabled LoC devices is envisaged to occur in synergy with advances in biological and chemical analytics. DLW will also be instrumental in achieving unprecedented levels of integration with the potential to incorporate optical, electrical fluidic and mechanical features in a single multifunctional device. The recently demonstrated ultrashort pulse laser welding of dissimilar dielectric materials is set to play a major role in driving the integration of composite materials [250]. There are challenges that need to be addressed in the progress of DLW, such as improving inter-component tolerances, reducing fabrication times, writing optofluidic components in composite materials and streamlining the fluidic interfacing with established sample delivery methods. Advances in optofluidic device performances in alleviating these challenges will underpin the commercialisation of DLW enabled LoC devices. However, the capability of the technology in developing versatile optofluidic devices has already been widely acknowledged. The progress of DLW as an enabling technology for interdisciplinary analytical research will be fascinating to follow in the years to come.

6.3 Feasibility studies

In addition to the work presented in chapter 3, chapter 4 and chapter 5 of this thesis, work was also undertaken to analyse the possibility of integrating electrodes in DLW optofluidic devices. Furthermore, the possibility to fabricate selectively etched microneedles in fused silica was also investigated. The results from these studies are presented in the following sections.

6.3.1 Integrating electrodes in DLW optofluidic devices

The incorporation of electrodes in LoC devices adds a key element to their overall functionality. Several biologically relevant applications such as cell lysis, electro-osmosis, dielectrophoresis and electrochemical reactions have been realised in miniaturised devices that exhibit the capability to controllably apply steady or time-varying electric fields within the sample environments [251]. In particular, the phenomenon of transient and reversible permeabilisation of the membrane of eukaryotic cells upon the application of an external electric field otherwise known as electroporation, is well-recognised as a powerful biological transfection technique [252]. Electroporation allows temporary access to the cellâĂŹs interior to deliver substances such as foreign DNA, proteins and even inorganic materials that are otherwise not permeable through the cell membrane. The controlled application of an external electric field on such cells can induce their transmembrane potential (TMP) to surpass the threshold for dielectric breakdown resulting in the formation of nano-sized pores. The degree of reversibility of such structural permeabilisation is governed by complex biochemical mechanisms that depend upon the intensity and duration of the applied electric field [252]. The change in TMP is known to vary linearly with the size of the cell as well as the angle (θ_e) between the external electric field ($\overrightarrow{E}_{ext}$) and the vector defining the position on the cell membrane where TMP is measured. In the particular case of spherical cells with size (r_{cell}), the change in TMP is given as shown in equation 6.1 [253, 254]

$$\delta TMP \propto \frac{3}{2} \overrightarrow{r}_{cell} \overrightarrow{E}_{ext} cos\theta_e \tag{6.1}$$

Considering $\overrightarrow{E}_{ext}$ to be uniform, the cosθ_e dependence of δTMP results in the polarised poration in spherical cells, where the density of pores is maximised at the sites in the cell membrane where $\theta_e \approx 0$ or π [255]. This presents an interesting area of investigation where a study of the temporal and spatial dynamics of poration can be undertaken in suspended cells whose orientation with respect to $\overrightarrow{E}_{ext}$ can be altered.

DLW offers an elegant functionality to enable this study, wherein optical waveguides and microfluidic channels can be integrated monolithically with pre-aligned electrodes forming a continuous flow system. The optical waveguides can be fabricated in a dual beam trap arrangement featuring a lateral offset to achieve the rotational motion of

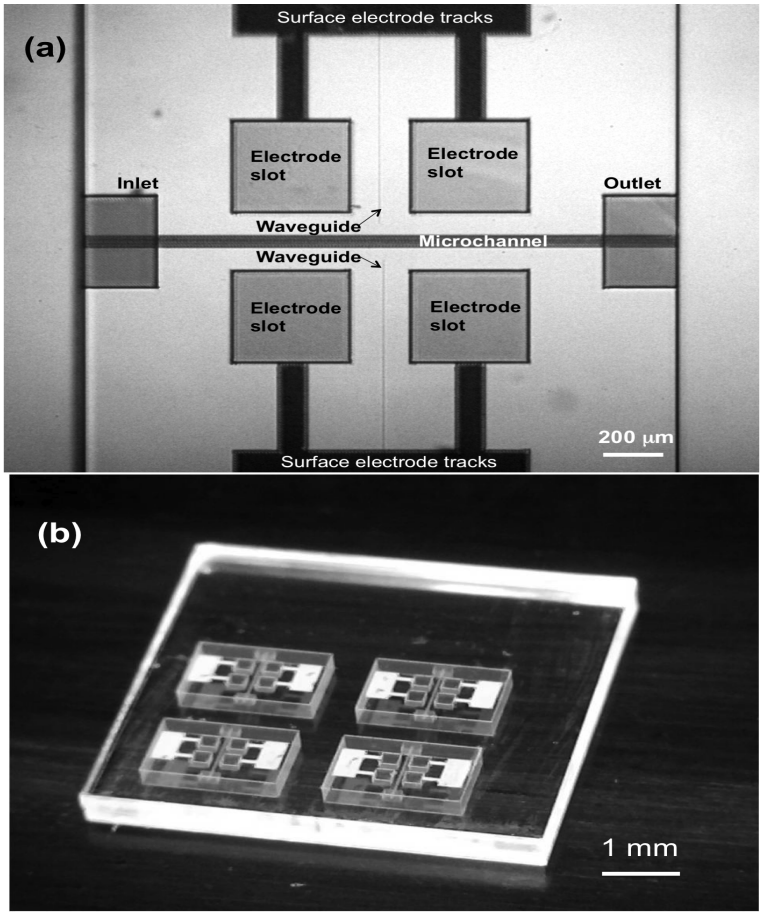

Figure 6.1: DLW integrated device for continuous flow electroporation. (a) Optical transmission microscope image showing the device with the electrode slots, waveguides and the microchannel. (b) A set of four identical devices after DLW prior to etching.

a trapped cell. The value of the offset can be optimised to ensure that a trapped cell, experiences a net non-zero torque that will enable its rotational motion. This feature will allow the orientation of poration sites in the membrane of an optically trapped cell to be altered with respect to $\overrightarrow{E}_{ext}$ during electroporation. Furthermore, a microsystem featuring such a capability can also potentially address the difficulty to achieve uniform dosage control commonly associated with continuous flow or adhered cell electroporation mechanisms [256]. With this aim, a DLW device was fabricated with the design shown in figure 6.1. The DLW optofluidic electroporation device shown in figure 6.1 was written in the transverse geometry using ≈ 390 fs pulses at 1047 nm, delivered at a repetition rate of 500 kHz from the commercial Yb-doped MOPA

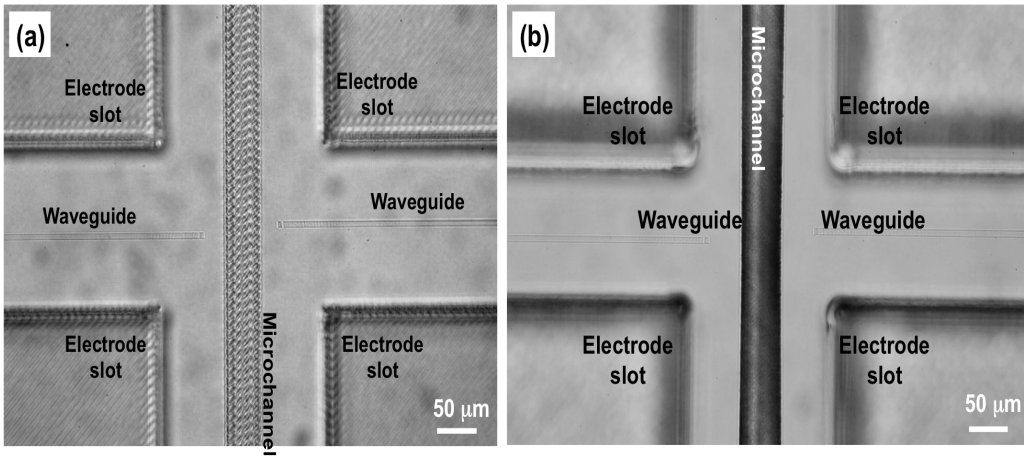

Figure 6.2: Top view of DLW optical waveguides featuring a core-to-core offset of 8 μm. (a) The laser written design before etching (b) The design after etching using 5 % aqueous solution of HF for 5 hours.

system (IMRA America FCPA Îij Jewel D400) described in section 2.5. The pulses were focused inside a 1 mm thick fused silica substrate (Corning 7980, UV Grade) using a 0.4 NA (x20) aspheric objective lens. The design features a 2 mm long microchannel with a cross-section of 50 μm × 50 μm written at a depth of 325 μm from the top surface of the substrate. Four cuboidal electrode slots with an edge length of 400 μm were symmetrically aligned with respect to the microchannel as shown in figure 6.1. The electrode slots are linked to bond pads for electrical connection using DLW surface tracks as shown in figure 6.1. In addition, two NIR optical waveguides were designed to be orthogonally aligned to the microchannel as shown in figure 6.2 with a core-to-core offset of 8μm. The microchannel shows almost taper-free etching. The electrode slots, the fluidic inlets and the microchannel were written using 650 nJ linearly polarised pulses at a translation speed of 4 $mm\ s^{-1}$. The NIR waveguides were written at a depth of 320 μm using 238 nJ circularly polarised pulses at 2 $mm\ s^{-1}$ by employing the multiscan technique with 20 scans at a scan separation of 0.4 μm. The waveguides were optimised for low loss single-mode guiding of 980 nm light. Polarisation sensitive etching was performed on the laser written design using HF at 5 % dilution in an ultrasonic bath for 5 hours. Figure 6.2 also shows the alignment of the optical waveguides with the electrode slots before and after etching. Using a thermal vacuum evaporation process, a $\approx$ 2 μm thin film of copper was coated onto

the electrode slots and surface tracks by masking the rest of the device using scotch-tape. Prior to copper coating, a base layer of nickel was initially deposited onto the fused silica device in order to maximise adherence. Inside the thermal evaporation chamber, the device was mounted on a rotating holder in order to ensure a uniform coating on all inner surfaces of the electrode slots. Figure 6.3(a) depicts a side-view of the device clearly showing the copper coated electrodes and their relative position with the microchannel. The photograph of the device is shown in figure 6.3(b)

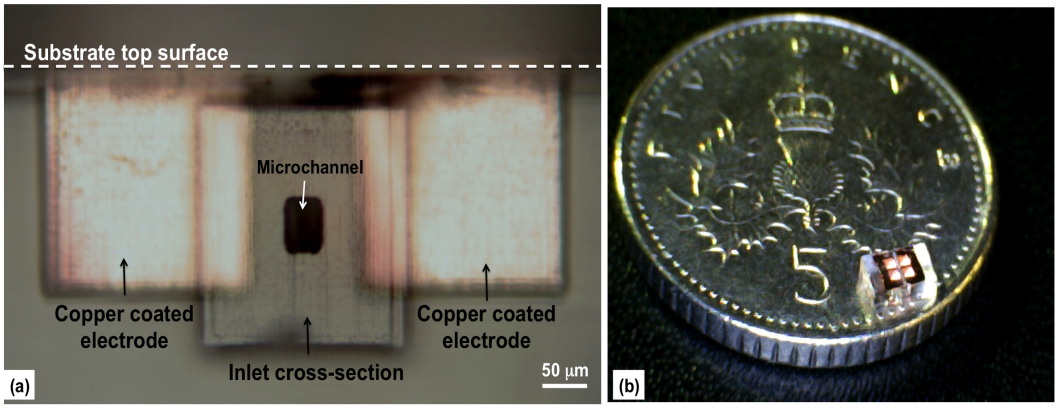

Figure 6.3: (a) Side-view of the device showing copper coated electrodes. (b) Photograph showing the optofluidic electroporation device

The key application of this device is envisaged to be the measurement of intracellular temperature change in cells when they undergo electroporation using the quantum dot nanothermometry described in chapter 4. The device can be used to apply DC as well as AC fields and the optimum conditions required to achieve reversible electroporation can be identified on optically trapped non-adherent mammalian cells. The uptake of surface functionalised quantum dots, that are otherwise impermeant to the cell membrane can be investigated using this optofluidic device by taking advantage of the cell rotation capability. Electroporation parameters can be optimised to enable the internalisation of the quantum dots. These nanomaterials can subsequently enable the accurate determination of intracellular temperature in localised regions within cells and examine its variation when the cells are subjected to externally applied deforming forces. The waveguide arrangement in the device can also be optimised for application in the controlled photoporation of non-adherent cells [257]. The device can be suitably optimised for application with both electroporation and photoporation schemes with

an aim to achieve quantifiable dosage of impermeant substances inside the cell.

Relevant publications

1. D. Choudhury, L. M. Maestro, W. T. Ramsay, L. Paterson, D. Jaque, and A. K. Kar, "Continuous flow single cell electroporation in an ultrafast laser inscribed optofluidic device," International Conference on Fibre Optics and Photonics (2012), paper T1A.4 (2012).

Contributions
D. Choudhury designed and fabricated the device. L.M. Maestro and W.T. Ramsay assisted D. Choudhury in optimising the fabrication.

6.3.2 The selective etching of microneedles using DLW

The development of new methods to fabricate microneedles have rapidly expanded since their initial demonstration in the 1970s [258]. The principal driving factor for the search for new fabrication techniques has primarily been the quantifiable, repeatable and safe transdermal delivery of drugs and vaccines. Microneedles also constitute a suitable method to deliver drugs inside single cells when combined with well-characterised non-intrusive methods of cell manipulation such as optical tweezers and traps. Optical tweezers have enabled methods to develop microinjectors for the delivery of substances inside a living cell [259]. The performance of such microinjectors is evidently dependent upon the quality and repeatability of the needles. Variabilities in needle diameter, thickness and length necessitate corrective re-alignment steps that are typically time consuming and result in unwanted error. To alleviate this issue, the potential of applying selective etching of DLW to fabricate cylindrical microneedles in fused silica has been investigated.

The DLW process was performed using the IMRA FCPA setup described in section 2.5, with an important adjustment as shown in figure 6.4. A variable beam expander (Special Optics, 56-30-2-8x-1047-1064 nm) was placed in the optical path of the fs laser beam in order to ensure that the beam filled the back aperture of an oil-immersion (Type F, RI = 1.518 at 23 ^oC) 1.4 NA focusing objective lens (Olympus

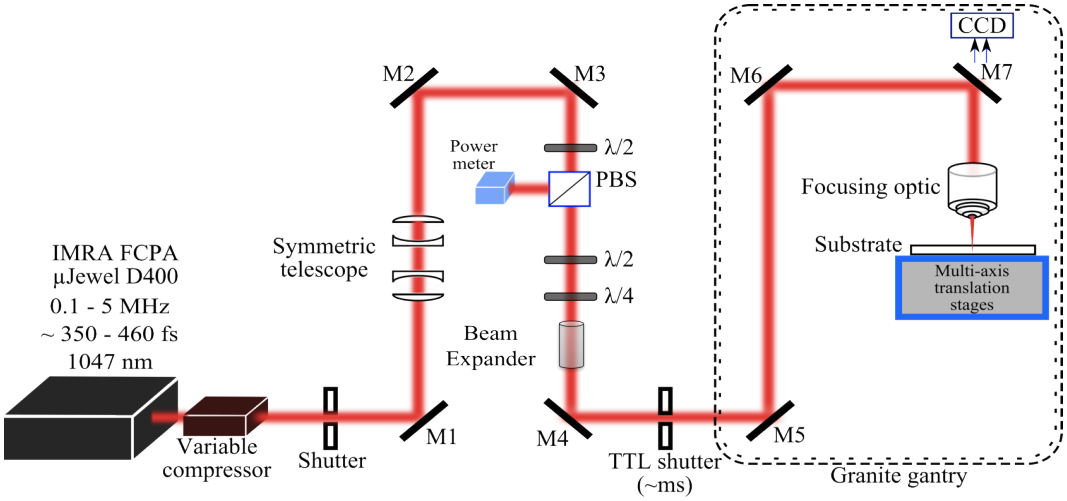

Figure 6.4: Schematic illustration of DLW setup for fabricating microneedles using a 1.4 NA focusing optic. The beam expander was placed between the $\lambda/4$ plate and the TTL shutter.

UPLSAPO($\times$100)) used for this work.

The transverse writing geometry was applied in this work wherein the microneedle design involved translation of the laser focus spot in two concentric cylindrical paths in the same method as illustrated in figure 3.6. The outer and inner diameters of the needle structures were designed to be 10 μm and 5 μm respectively. Setting the repetition rate at 500 kHz resulted in no modification of the material, regardless of the average power used for the writing pulses. Consequently, the repetition rate was reduced to 100 kHz to increase the interaction time of each pulse with the material, which resulted in material modification. A parameter scan was then implemented to identify the range of average powers and translation speeds suitable for the fabrication of microneedles. Circularly polarised pulses were applied for this parameter scan. Figure 6.5 shows optical transmission microscopy images of an array of microneedles written using the parameters specified. The accurate calibration of substrate tilt is crucial to ensure the correct writing of the structures. The maximum depth achievable using this scheme of writing was $\approx$ 25 μm. At 1047 nm, the 1.4 NA objective used in this work was measured to exhibit a throughput of $\approx$ 40 %. Therefore, the material modification threshold pulse energy corresponds to $\approx$ 152 nJ in this case, as shown in figure 6.5(d). As can be observed from figure 6.5, the concentric cross-section of the microneedles is

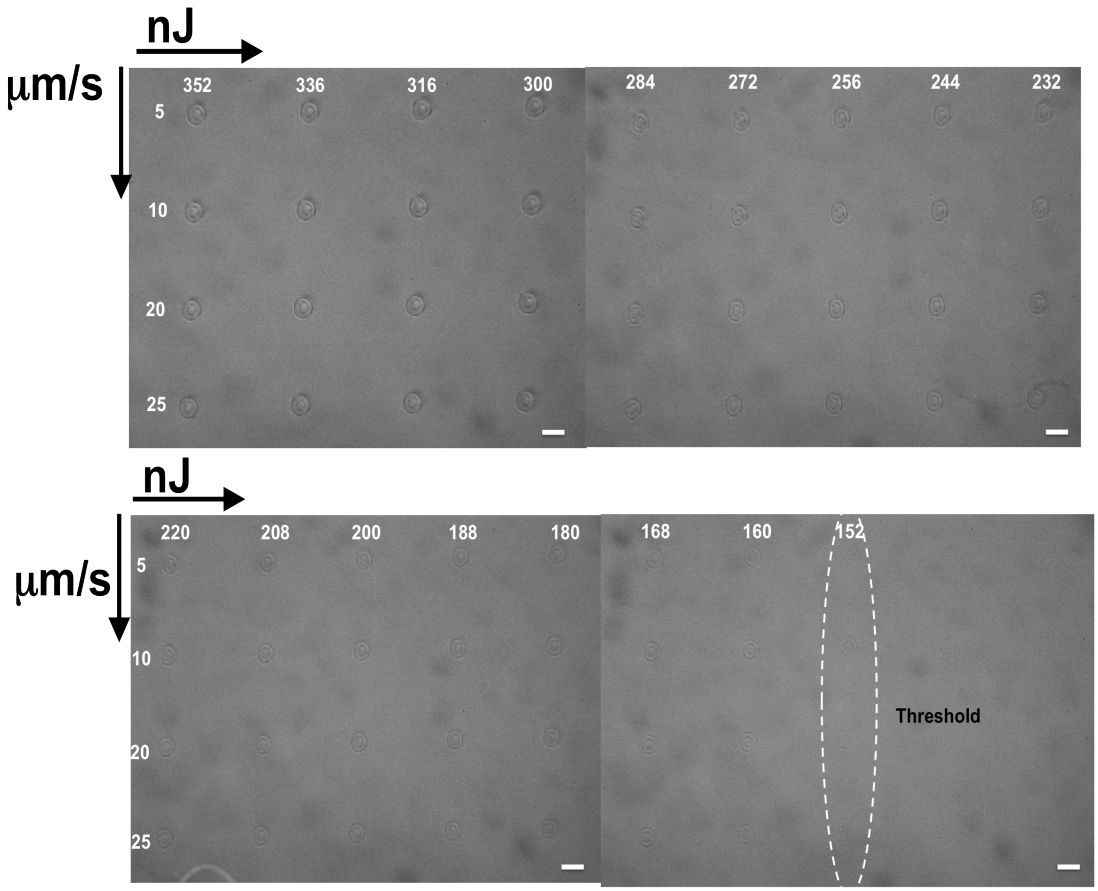

Figure 6.5: Parameter scan for microneedle fabrication at 100 kHz. The average powers indicated were measured before the objective. Material modification threshold was observed at an average power of 38 mW before the objective. The scale bars represent 10 μm

written without damage. The structures were subsequently etched using an aqueous solution of KOH at a concentration of 8.77 M and an elevated temperature of 80 ^oC for 3 hours. KOH was selected as an appropriate etchant for this work as its selectivity is higher compared to HF, although the etch rate is significantly slower. Figure 6.6 shows the top view of a partially etched microneedle, the writing and etching parameters are indicated in the figure. The selectivity of the etch profile can be clearly observed to follow the laser modified regions of the structure. The microneedle structures were completely etched after $\approx$ 3 hours leaving behind an array of hollow voids as shown in figure 6.7. The above study strongly indicated the possibility of applying DLW with

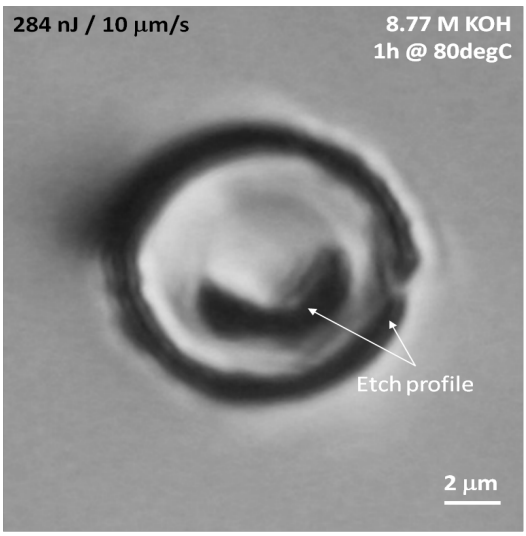

Figure 6.6: Optical transmission microscopy image showing the etch profile of a microneedle written using the parameters indicated. The selectivity can be clearly observed.

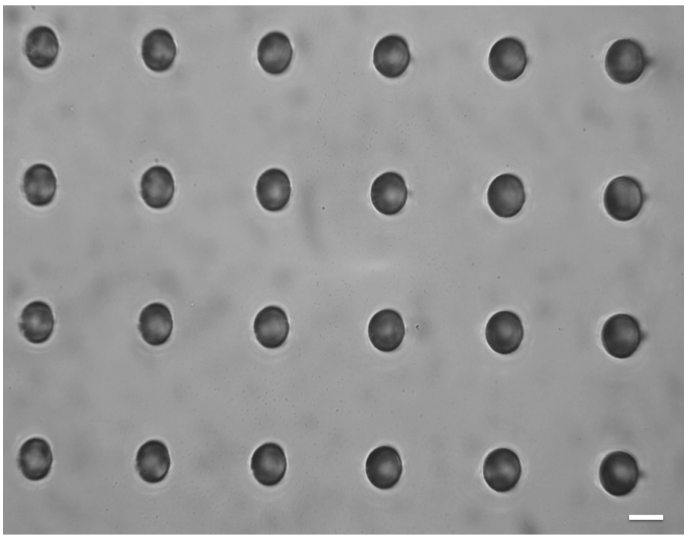

Figure 6.7: An array of empty microvoids after etching of needles. The scale bar represents 10 μm

KOH etching in the fabrication of microneedles. There is scope to use laser writing to make smaller diameter needles. However, an appropriate procedure to collect the etched microneedles is necessary to enable their close examination in order to correctly quantify the laser writing and etching tolerances for optimised fabrication.

Contributions

D. Choudhury performed the parameter analysis using DLW.

References

[1] David. Erickson, Changhuei. Yang, and Demetri Psaltis. Optofluidics emerges from the laboratory. *Photonics Spectra*, 42:74–78, 2008. 1

[2] Purnendu K. Dasgupta, Zhang Genfa, Simon K. Poruthoor, Steven Caldwell, Shen Dong, and Su-Yi Liu. High-sensitivity gas sensors based on gas-permeable liquid core waveguides and long-path absorbance detection. *Analytical Chemistry*, 70(22):4661–4669, 1998. 1

[3] Ermanno F Borra. The case for liquid mirrors in orbiting telescopes. *Astrophysical Journal*, 392:375–383, 1992. 1

[4] Christopher B. Gorman, Hans A. Biebuyck, and George M. Whitesides. Control of the shape of liquid lenses on a modified gold surface using an applied electrical potential across a self-assembled monolayer. *Langmuir*, 11(6):2242–2246, 1995. 1

[5] David. Erickson, David. Sinton, and Demetri Psaltis. Optofluidics for energy applications. *Nature Photonics*, 5(10):583–590, 2011. 1

[6] Yih-Fan Chen, Li Jiang, Matthew Mancuso, Aadhar Jain, Vlad Oncescu, and David Erickson. Optofluidic opportunities in global health, food, water and energy. *Nanoscale*, 4:4839–4857, 2012. 1

[7] Klaus B. Mogensen and JÃűrg P. Kutter. Optical detection in microfluidic systems. *ELECTROPHORESIS*, 30(S1):S92–S100, 2009. 2

[8] George M Whitesides. The origins and the future of microfluidics. *Nature*, 442:368–373, 2006. 2, 5, 14

[9] Todd M. Squires and Stephen R. Quake. Microfluidics: Fluid physics at the nanoliter scale. *Rev. Mod. Phys.*, 77:977–1026, 2005. 2

[10] Patrick Tabeling. *Introduction to microfluidics*. Oxford University Press, Oxford, 2005. 2, 3, 4, 5

[11] Mohamed Gad el Hak. The fluid mechanics of microdevices—the freeman scholar lecture. *Journal of Fluids Engineering*, 121(1):5–33, 1999. 3, 4

[12] Niels. Lion, FrÃČÂĬdÃČÂĬric. Reymond, Hubert H. Girault, and JoÃČÂńl S Rossier. Why the move to microfluidics for protein analysis? *Current Opinion in Biotechnology*, 15(1):31 – 37, 2004. 5

[13] Mathieu. Joanicot and Armand Ajdari. Droplet control for microfluidics. *Science*, 309(5736):887–888, 2005. 5

[14] Joshua S. Marcus, W. French Anderson, and Stephen R. Quake. Parallel picoliter rt-pcr assays using microfluidics. *Analytical Chemistry*, 78(3):956–958, 2006. 5

[15] Bharat BHushan, editor. *Handbook of Nanotechnology*. Springer, London, 2010. 5

[16] Henne van Heeren. Standards for connecting microfluidic devices? *Lab on a Chip*, 12:1022–1025, 2012. 5

[17] Xudong. Fan and Ian M White. Optofluidic microsystems for chemical and biological analysis. *Nature Photonics*, 5:591–597, 2011. 5, 6, 10

[18] Yunbo Guo, Hao Li, Karthik Reddy, Hrishikesh S Shelar, Vasuki R Nittoor, and Xudong Fan. Optofluidic Fabry–Pérot cavity biosensor with integrated flow-through micro-/nanochannels. *Applied Physics Letters*, 98(4):041104, 2011. 5

[19] KatharinaK. Strelau, Robert Kretschmer, Robert MÃűller, Wolfgang Fritzsche, and JÃijrgen Popp. Sers as tool for the analysis of dna-chips in a microfluidic platform. *Analytical and Bioanalytical Chemistry*, 396:1381–1384, 2010. 6, 9

[20] A. Chen, M. M. Eberle, E. J. Lunt, S. Liu, K. Leake, M. I. Rudenko, A. R. Hawkins, and H. Schmidt. Dual-color fluorescence cross-correlation spectroscopy on a planar optofluidic chip. *Lab on a Chip*, 11:1502–1506, 2011. 6, 10

[21] Igor L Medintz, H Tetsuo Uyeda, Ellen R Goldman, and Hedi Mattoussi. Quantum dot bioconjugates for imaging, labelling and sensing. *Nature Materials*, 4(6):435–446, June 2005. 6, 90

[22] Lin Pang, H. Matthew Chen, Lindsay M. Freeman, and Yeshaiahu Fainman. Optofluidic devices and applications in photonics, sensing and imaging. *Lab on a Chip*, 12:3543–3551, 2012. 6

[23] Ahmet A Yanik, Min Huang, Osami Kamohara, Alp Artar, Thomas W Geisbert, John H Connor, and Hatice Altug. An Optofluidic Nanoplasmonic Biosensor for Direct Detection of Live Viruses from Biological Media. *Nano Letters*, 10(12):4962–4969, 2010. 6

[24] H J. Ebbesen, H F. Lezec, T Thio. Ghaemi, and P A Wolff. Extraordinary optical transmission through sub-wavelength hole arrays. *Nature*, 391(6668):667–669, 1998. 6

[25] Lin. Pang, Grace M. Hwang, Boris. Slutsky, and Yeshaiahu Fainman. Spectral sensitivity of two-dimensional nanohole array surface plasmon polariton resonance sensor. *Applied Physics Letters*, 91(12):123112, 2007. 6

[26] Sajeev John. Strong localization of photons in certain disordered dielectric superlattices. *Phys. Rev. Lett.*, 58:2486–2489, 1987. 6

[27] Nina. Skivesen, Amélie. Têtu, Martin. Kristensen, Jørgen. Kjems, Lars H. Frandsen, and Peter I Borel. Photonic-crystal waveguide biosensor. *Optics Express*, 15(6):3169–3176, 2007. 7

[28] LeoL. Chan, SaujanyaL. Gosangari, KennethL. Watkin, and BrianT. Cunningham. A label-free photonic crystal biosensor imaging method for detection of cancer cell cytotoxicity and proliferation. *Apoptosis*, 12:1061–1068, 2007. 7

[29] David Erickson, Sudeep Mandal, AllenH.J. Yang, and Bernardo Cordovez. Nanobiosensors: optofluidic, electrical and mechanical approaches to biomolecular detection at the nanoscale. *Microfluidics and Nanofluidics*, 4:33–52, 2008. 7

[30] Lars. Rindorf, Jesper B. Jensen, Martin. Dufva, Lars Hagsholm. Pedersen, Poul Erik. Høiby, and Ole Bang. Photonic crystal fiber long-period gratings for biochemical sensing. *Optics Express*, 14(18):8224–8231, 2006. 7

[31] Aurel Ymeti, Jan Greve, Paul V. Lambeck, Thijs Wink, van HÃűvell, Beumer, Robert R. Wijn, Rene G. Heideman, Vinod. Subramaniam, and Johannes S. Kanger. Fast, ultrasensitive virus detection using a young interferometer sensor. *Nano Letters*, 7(2):394–397, 2007. 7

[32] Jie Xu, David Suarez, and DavidS. Gottfried. Detection of avian influenza virus using an interferometric biosensor. *Analytical and Bioanalytical Chemistry*, 389:1193–1199, 2007. 7

[33] Victor S.-Y. Lin, Kianoush Motesharei, Keiki-Pua S. Dancil, Michael J. Sailor, and M. Reza Ghadiri. A porous silicon-based optical interferometric biosensor. *Science*, 278(5339):840–843, 1997. 7

[34] S. Y. Wu, H. P. Ho, W. C. Law, Chinlon Lin, and S. K. Kong. Highly sensitive differential phase-sensitive surface plasmon resonancebiosensor based on the mach–zehnder configuration. *Optics Letters*, 29(20):2378–2380, 2004. 7

[35] Christian Hoffmann, Katrin Schmitt, Albrecht Brandenburg, and Steffen Hartmann. Rapid protein expression analysis with an interferometric biosensor for monitoring protein production. *Analytical and Bioanalytical Chemistry*, 387:1921–1932, 2007. 7

[36] Steve. Blair and Yan Chen. Resonant-enhanced evanescent-wave fluorescence biosensing with cylindrical optical cavities. *Applied Optics*, 40(4):570–582, 2001. 7, 8

[37] C. Monat, P. Domachuk, and B J Eggleton. Integrated optofluidics: A new river of light. *Nature Photonics*, 1:106–114, 2007. 7, 15, 18, 107

[38] Kerry J Vahala. Optical microcavities. *Nature*, 424:839–846, 2003. 7

[39] Robert W. Boyd and John E Heebner. Sensitive disk resonator photonic biosensor. *Applied Optics*, 40(31):5742–5747, 2001. 7

[40] D K. Armani, T J. Kippenberg, S M. Spillane, and K J Vahala. Ultra-high-q toroid microcavity on a chip. *Nature*, 421(6926):925–928, 2003. 8

[41] Andrea M. Armani and Kerry J. Vahala. Heavy water detection using ultra-high-q microcavities. *Optics Letters*, 31(12):1896–1898, 2006. 8

[42] E. Krioukov, J. Greve, and C Otto. Performance of integrated optical microcavities for refractive index and fluorescence sensing. *Sensors and Actuators B: Chemical*, 90(1ÃćâĆňâĂIJ3):58 – 67, 2003. 8

[43] Frank. Vollmer and Stephen Arnold. Whispering-gallery-mode biosensing: label-free detection down to single molecules. *Nature Methods*, 5(7):591–596, 2008. 8

[44] Muzammil Iqbal, Martin A Gleeson, Bradley Spaugh, Frank Tybor, William G Gunn, Michael Hochberg, Tom Baehr-Jones, Ryan C Bailey, and L Cary Gunn. Label-Free Biosensor Arrays Based on Silicon Ring Resonators and High-Speed Optical Scanning Instrumentation. *IEEE Journal of Selected Topics in Quantum Electronics*, 16(3):654–661, 2010. 8

[45] Alexandre Francois and Michael Himmelhaus. Whispering gallery mode biosensor operated in the stimulated emission regime. *Applied Physics Letters*, 94(3):031101, 2009. 8

[46] Sudeep Mandal, Julie M Goddard, and David Erickson. A multiplexed optofluidic biomolecular sensor for low mass detection. *Lab on a Chip*, 9(20):2924, 2009. 8

[47] Katrien De Vos, Irene Bartolozzi, Etienne Schacht, Peter Bienstman, and Roel Baets. Silicon-on-insulator microring resonator forsensitive and label-free biosensing. *Optics Express*, 15(12):7610–7615, 2007. 8

[48] Lei Jin, Mingyu Li, and Jian-Jun He. Highly-sensitive silicon-on-insulator sensor based on two cascaded micro-ring resonators with vernier effect. *Optics Communications*, 284(1):156 – 159, 2011. 8

[49] Derek A. Long. *The Raman Effect: A Unified Treatment of the Theory of Raman Scattering by Molecules*. John Wiley and Sons, Ltd., Chichester, 2002. 9

[50] Gang L. Liu and Luke P. Lee. Nanowell surface enhanced raman scattering arrays fabricated by soft-lithography for label-free biomolecular detections in integrated microfluidics. *Applied Physics Letters*, 87(7):074101, 2005. 9

[51] Katrin Kneipp, Yang Wang, Harald Kneipp, Lev T. Perelman, Irving Itzkan, Ramachandra R. Dasari, and Michael S. Feld. Single molecule detection using surface-enhanced raman scattering (sers). *Physical Review Letters*, 78:1667–1670, 1997. 9

[52] Shuming Nie and Steven R. Emory. Probing single molecules and single nanoparticles by surface-enhanced raman scattering. *Science*, 275(5303):1102–1106, 1997. 9

[53] Anne MÃďrz, Bettina MÃűnch, Petra RÃűsch, Michael Kiehntopf, Thomas Henkel, and JÃijrgen Popp. Detection of thiopurine methyltransferase activity in lysed red blood cells by means of lab-on-a-chip surface enhanced raman spectroscopy (loc-sers). *Analytical and Bioanalytical Chemistry*, 400:2755–2761, 2011. 9

[54] Angela Walter, Anne Marz, Wilm Schumacher, Petra Rosch, and Jurgen Popp. Towards a fast, high specific and reliable discrimination of bacteria on strain level by means of sers in a microfluidic device. *Lab on a Chip*, 11:1013–1021, 2011. 9

[55] Yun Suk Huh, Aram J. Chung, Bernardo Cordovez, and David Erickson. Enhanced on-chip sers based biomolecular detection using electrokinetically active microwells. *Lab on a Chip*, 9:433–439, 2009. 9

[56] Praveen C. Ashok, Gajendra P. Singh, Helen A. Rendall, Thomas F. Krauss, and Kishan Dholakia. Waveguide confined raman spectroscopy for microfluidic interrogation. *Lab on a Chip*, 11:1262–1270, 2011. 9

[57] Praveen C Ashok, Bavishna B Praveen, and Kishan Dholakia. Near infrared spectroscopic analysis of single malt scotch whisky on an optofluidic chip. *Optics Express*, 19(23):22982–22992, 2011. 9

[58] V. Korampally, S. Mukherjee, M. Hossain, R. Manor, Minseong Yun, K. Gangopadhyay, L. Polo-Parada, and S. Gangopadhyay. Development of a minia-

turized liquid core waveguide system with nanoporous dielectric cladding: A potential biosensing platform. *Sensors Journal, IEEE*, 9(12):1711 – 1718, 2009. 10

[59] Sung Hwan Cho, J. Godin, and Yu-Hwa Lo. Optofluidic waveguides in teflon af-coated pdms microfluidic channels. *Photonics Technology Letters, IEEE*, 21(15):1057 –1059, 2009. 10

[60] E. Coscelli, M. Sozzi, F. Poli, D. Passaro, A. Cucinotta, S. Selleri, R. Corradini, and R. Marchelli. Toward a highly specific dna biosensor: Pna-modified suspended-core photonic crystal fibers. *Selected Topics in Quantum Electronics, IEEE Journal of*, 16(4):967 –972, 2010. 10

[61] S SURESH. Biomechanics and biophysics of cancer cells. *Acta Materialia*, 55(12):3989–4014, 2007. 10

[62] G Bao and S SURESH. Cell and molecular mechanics of biological materials. *Nature Materials*, 2(11):715–725, 2003. 11

[63] Hermann Schillers, Mike Wälte, Katarina Urbanova, and Hans Oberleithner. Real-time monitoring of cell elasticity reveals oscillating myosin activity. *Biophysical Journal*, 99(11):3639–3646, 2010. 11

[64] J Guck, R Ananthakrishnan, H Mahmood, TJ Moon, CC Cunnningham, and J Kas. The Optical Stretcher: A Novel Laser Tool to Micromanipulate Cells. *Biophysical Journal*, 81(2):767–784, August 2001. 11, 51, 61

[65] Jochen Guck, Stefan Schinkinger, Bryan Lincoln, Falk Wottawah, Susanne Ebert, Maren Romeyke, Dominik Lenz, Harold M Erickson, Revathi Ananthakrishnan, Daniel Mitchell, Josef Käs, Sydney Ulvick, and Curt Bilby. Optical deformability as an inherent cell marker for testing malignant transformation and metastatic competence. *Biophysical Journal*, 88(5):3689–3698, May 2005. 11

[66] N Bellini, KC Vishnubhatla, F Bragheri, L Ferrara, P Minzioni, R Ramponi, I Christiani, and R Osellame. Femtosecond laser fabricated monolithic chip for optical trapping and stretching of single cells. *Optics Express*, 18(5):4679–4688, February 2010. 11, 51, 52, 61, 65

[67] Farhan Chowdhury, Sungsoo Na, Dong Li, Yeh-Chuin Poh, Tetsuya S Tanaka, Fei Wang, and Ning Wang. Material properties of the cell dictate stress-induced spreading and differentiation in embryonic stem cells. *Nature Materials*, 9(1):82–88, 2009. 11

[68] Igor Titushkin and Michael Cho. Modulation of cellular mechanics during osteogenic differentiation of human mesenchymal stem cells. *Biophysical Journal*, 93(10):3693–3702, 2007. 11

[69] Carlos D S Brites, Patricia P Lima, Nuno J O Silva, Angel Millán, Vitor S Amaral, Fernando Palacio, and Luís D Carlos. A luminescent molecular thermometer for long-term absolute temperature measurements at the nanoscale. *Advanced Materials*, 22(40):4499–4504, 2010. 12

[70] Carlos D S Brites, Patricia P Lima, Nuno J O Silva, Angel Millán, Vitor S Amaral, Fernando Palacio, and Luís D Carlos. Lanthanide-based luminescent molecular thermometers. *New Journal of Chemistry*, 35(6):1177, 2011. 12

[71] Susanne Ebert, Kort Travis, Bryan Lincoln, and Jochen Guck. Fluorescence ratio thermometry in a microfluidic dual-beam laser trap. *Optics Express*, 15(23):15493–15499, 2007. 12, 13

[72] Mathieu A Bennet, Patricia R Richardson, Jochen Arlt, Aongus McCarthy, Gerald S Buller, and Anita C Jones. Optically trapped microsensors for microfluidic temperature measurement by fluorescence lifetime imaging microscopy. *Lab Chip*, 11(22):3821–3828, 2011. 13

[73] Guilhem Velve Casquillas, Chuanhai Fu, Mael Le Berre, Jeremy Cramer, Sebastien Meance, Adrien Plecis, Damien Baigl, Jean-Jacques Greffet, Yong Chen, Matthieu Piel, and Phong T Tran. Fast microfluidic temperature control for high resolution live cell imaging. *Lab on a Chip*, 11(3):484–489, 2011. 13, 87

[74] Kwanghun Chung, Jae Kyu Cho, Edward S Park, Victor Breedveld, and Hang Lu. Three-Dimensional in Situ Temperature Measurement in Microsystems Using Brownian Motion of Nanoparticles. *Analytical Chemistry*, 81(3):991–999, 2009. 13

[75] Emmelyn M Graham, Kaoru Iwai, Seiichi Uchiyama, A Prasanna de Silva, Steven W Magennis, and Anita C Jones. Quantitative mapping of aqueous microfluidic temperature with sub-degree resolution using fluorescence lifetime imaging microscopy. *Lab on a Chip*, 10(10):1267, 2010. 13

[76] G Baffou, M P Kreuzer, F Kulzer, and R Quidant. Temperature mapping near plasmonic nanostructures using fluorescence polarization anisotropy. *Optics Express*, 17(5):3291, 2009. 13, 14

[77] Younan Xia and George M. Whitesides. Soft lithography. *Annual Review of Materials Science*, 28(1):153–184, 1998. 15

[78] Demetri Psaltis, Stephen R. Quake, and Changhuei Yang. Developing optofluidic technology through the fusion of microfluidics and optics. *Nature*, 442(7101):381–386, 2006. 15

[79] Dong Qin, Younan Xia, and George M Whitesides. Soft lithography for micro- and nanoscale patterning. *Nature Protocols*, 5:491âĂŞ502, 2010. 15

[80] Todd Thorsen, Sebastian J. Maerkl, and Stephen R. Quake. Microfluidic large-scale integration. *Science*, 298(5593):580–584, 2002. 15

[81] Daiying Zhang, Liqiu Men, and Qiying Chen. Microfabrication and applications of opto-microfluidic sensors. *Sensors*, 11(5):5360–5382, 2011. 15

[82] Keith E Harold and Avraham Rasooly, editors. *Lab-on-a-Chip Technology: Fabrication and Microfluidics*. Caister Academic Press, Norfolk, 2009. 15

[83] K. M Davis, K Miura, N Sugimoto, and K Hirao. Writing waveguides in glass with a femtosecond laser. *Optics Letters*, 21(21):1729–1731, 1996. 15, 26, 27, 37, 44

[84] Andrius Marcinkevičius, Saulius Juodkazis, Mitsuru Watanabe, Masafumi Miwa, Shigeki Matsuo, Hiroaki Misawa, and Junji Nishii. Femtosecond laser-assisted three-dimensional microfabrication in silica. *Optics Letters*, 26(5):277–279, 2001. 16, 37, 45, 46

[85] Kun Zhao, Qi Zhang, Michael Chini, Yi Wu, Xiaowei Wang, and Zenghu Chang. Tailoring a 67 attosecond pulse through advantageous phase-mismatch. *Optics Letters*, 37(18):3891–3893, 2012. 21

[86] X. Liu, D. Du, and G. Mourou. Laser ablation and micromachining with ultrashort laser pulses. *Quantum Electronics, IEEE Journal of*, 33(10):1706 –1716, 1997. 21

[87] Rafael R. Gattass and Eric Mazur. Femtosecond laser micromachining in transparent materials. *Nature Photonics*, 2:219–225, 2008. 22, 23, 24, 25

[88] Chris B. Schaffer, AndrÃľ Brodeur, and Eric Mazur. Laser-induced breakdown and damage in bulk transparent materials induced by tightly focused femtosecond laser pulses. *Measurement Science and Technology*, 12(11):1784–1794, 2001. 22, 23, 24, 26

[89] I.V. Keldysh. Ionization in the field of a strong electromagnetic wave. *Soviet Physics JETP*, 20(5):1307–1314, 1965. 22

[90] D. Rayner, A. Naumov, and P. Corkum. Ultrashort pulse non-linear optical absorption in transparent media. *Optics Express*, 13(9):3208–3217, 2005. 24

[91] B. C. Stuart, M. D. Feit, S. Herman, A. M. Rubenchik, B. W. Shore, and M. D. Perry. Nanosecond-to-femtosecond laser-induced breakdown in dielectrics. *Physical Review B*, 53:1749–1761, 1996. 25

[92] Masaaki Sakakura and Masahide Terazima. Initial temporal and spatial changes of the refractive index induced by focused femtosecond pulsed laser irradiation inside a glass. *Physical Review B*, 71:024113, 2005. 25

[93] M. Sakakura, M. Terazima, Y. Shimotsuma, K. Miura, and K. Hirao. Observation of pressure wave generated by focusing a femtosecond laser pulse inside a glass. *Optics Express*, 15(9):5674–5686, 2007. 25

[94] B. C. Stuart, M. D. Feit, S. Herman, A. M. Rubenchik, B. W. Shore, and M. D. Perry. Optical ablation by high-power short-pulse lasers. *Journal of Optical Society of America B*, 13(2):459–468, 1996. 25

[95] D. Du, X. Liu, G. Korn, J. Squier, and G. Mourou. Laser-induced breakdown by impact ionization in sio[sub 2] with pulse widths from 7 ns to 150 fs. *Applied Physics Letters*, 64(23):3071–3073, 1994. 26

[96] R. Taylor, C. Hnatovsky, and E. Simova. Applications of femtosecond laser induced self-organized planar nanocracks inside fused silica glass. *Laser and Photonics Reviews*, 2(1-2):26–46, 2008. 26, 27, 28, 29

[97] Alexander M. Streltsov and Nicholas F. Borrelli. Study of femtosecond-laser-written waveguides in glasses. *Journal of Optical Society of America B*, 19(10):2496–2504, 2002. 26

[98] C. Hnatovsky, R. S. Taylor, P. P. Rajeev, E. Simova, V. R. Bhardwaj, D. M. Rayner, and P. B. Corkum. Pulse duration dependence of femtosecond-laser-fabricated nanogratings in fused silica. *Applied Physics Letters*, 87(1):014104, 2005. 26, 29

[99] Yasuhiko Shimotsuma, Peter G. Kazansky, Jiarong Qiu, and Kazuoki Hirao. Self-organized nanogratings in glass irradiated by ultrashort light pulses. *Physical Review Letters*, 91:247405, 2003. 26, 29

[100] S. Juodkazis, K. Nishimura, S. Tanaka, H. Misawa, E. G. Gamaly, B. Luther-Davies, L. Hallo, P. Nicolai, and V. T. Tikhonchuk. Laser-induced microexplosion confined in the bulk of a sapphire crystal: Evidence of multimegabar pressures. *Physical Review Letters*, 96:166101, 2006. 26

[101] C. Hnatovsky, R.S. Taylor, E. Simova, P.P. Rajeev, D.M. Rayner, V.R. Bhardwaj, and P.B. Corkum. Fabrication of microchannels in glass using focused femtosecond laser radiation and selective chemical etching. *Applied Physics A*, 84:47–61, 2006. 27, 28, 29

[102] J. W. Chan, T. Huser, S. Risbud, and D. M. Krol. Structural changes in fused silica after exposure to focused femtosecond laser pulses. *Optics Letters*, 26(21):1726–1728, 2001. 28

[103] P. Dekker, M. Ams, G. D. Marshall, D. J. Little, and M. J. Withford. Annealing dynamics of waveguide bragg gratings: evidence of femtosecond laser induced colour centres. *Optics Express*, 18(4):3274–3283, 2010. 28

[104] V. R. Bhardwaj, E. Simova, P. B. Corkum, D. M. Rayner, C. Hnatovsky, R. S. Taylor, B. Schreder, M. Kluge, and J. Zimmer. Femtosecond laser-induced refractive index modification in multicomponent glasses. *Journal of Applied Physics*, 97(8):083102, 2005. 28

[105] S. Eaton, G. Cerullo, and R. Osellame. *Fundamentals of Femtosecond Laser Modification of Bulk Dielectrics*. Springer, Berlin Heidelberg, 2012. 28, 35, 113

[106] Thomas Allsop, Mykhaylo Dubov, Vladimir Mezentsev, and Ian Bennion. Inscription and characterization of waveguides written into borosilicate glass by a high-repetition-rate femtosecond laser at 800 nm. *Applied Optics*, 49(10):1938–1950, 2010. 28

[107] Robert R. Thomson, Nicholas D. Psaila, Henry T. Bookey, Derryck T. Reid, and Ajoy K. Kar. Controlling the cross-section of ultrafast laser inscribed optical waveguides. In Roberto Osellame, Giulio Cerullo, and Roberta Ramponi, editors, *Femtosecond Laser Micromachining*, volume 123 of *Topics in Applied Physics*, pages 93–125. Springer Berlin Heidelberg, 2012. 28, 34, 35, 44

[108] L Sudrie, M Franco, B Prade, and A Mysyrowicz. Writing of permanent birefringent microlayers in bulk fused silica with femtosecond laser pulses. *Optics Communications*, 171(4-6):279–284, 1999. 28

[109] V. R. Bhardwaj, E. Simova, P. P. Rajeev, C. Hnatovsky, R. S. Taylor, D. M. Rayner, and P. B. Corkum. Optically produced arrays of planar nanostructures inside fused silica. *Physical Review Letters*, 96:057404, 2006. 29

[110] S. Richter, M. Heinrich, S. DÃűring, A. TÃijnnermann, and S. Nolte. Formation of femtosecond laser-induced nanogratings at high repetition rates. *Applied Physics A*, 104:503–507, 2011. 29

[111] SÃűren Richter, Matthias Heinrich, Sven DoÌĹring, Andreas TÃijnnermann, Stefan Nolte, , and Ulf Peschel. Nanogratings in fused silica: Formation, control, and applications. *Journal of Laser Applications*, 24:042008, 2012. 29

[112] Martynas Beresna, Mindaugas Gecevičius, and Peter G. Kazansky. Polarization sensitive elements fabricated by femtosecond laser nanostructuring of glass. *Optical Materials Express*, 1(4):783–795, 2011. 29

[113] Qiming Zhang, Han Lin, Baohua Jia, Lei Xu, and Min Gu. Nanogratings and nanoholes fabricated by direct femtosecond laser writing in chalcogenide glasses. *Optics Express*, 18(7):6885–6890, 2010. 29

[114] S Juodkazis, S Matsuo, H Misawa, V Mizeikis, A Marcinkevicius, H.-B Sun, Y Tokuda, M Takahashi, T Yoko, and J Nishii. Application of femtosecond laser pulses for microfabrication of transparent media. *Applied Surface Science*, 197-198:705 – 709, 2002. 30

[115] Andreas Ostendorf, Boris N Chichkov, and Laser Zentrum Hannover eV. Two-Photon Polymerization: A New Approach to Micromachining. *Photonics Spectra*, October, October 2006. 30

[116] Lorenzo Amato, Yu Gu, Nicola Bellini, Shane M Eaton, Giulio Cerullo, and Roberto Osellame. Integrated three-dimensional filter separates nanoscale from microscale elements in a microfluidic chip. *Lab on a Chip*, 12(6):1135–1142, 2012. 30

[117] Tommaso Baldacchini, Scott Snider, and Ruben Zadoyan. Two-photon polymerization with variable repetition rate bursts of femtosecond laser pulses. *Optics Express*, 20(28):29890, 2012. 31

[118] Mangirdas Malinauskas, Albertas Žukauskas, Gabija Bičkauskaitė, Roaldas Gadonas, and Saulius Juodkazis. Mechanisms of three-dimensional structuring of photo-polymers by tightly focussed femtosecond laser pulses. *Optics Express*, 18(10):10209–10221, 2010. 31

[119] Mangirdas Malinauskas, Paulius Danilevičius, and Saulius Juodkazis. Three-dimensional micro-/nano-structuring via direct write polymerization with picosecond laser pulses. *Optics Express*, 19(6):5602–5610, 2011. 31

[120] Shaun D Gittard, Alexander Nguyen, Kotaro Obata, Anastasia Koroleva, Roger J Narayan, and Boris N Chichkov. Fabrication of microscale medical devices by two-photon polymerization with multiple foci via a spatial light modulator. *Biomedical Optics Express*, 2(11):3167–3178, 2011. 31

[121] J. R. Macdonald, R. R. Thomson, S. J. Beecher, N. D. Psaila, H. T. Bookey, and A. K. Kar. Ultrafast laser inscription of near-infrared waveguides in polycrystalline znse. *Optics Letters*, 35(23):4036–4038, 2010. 33, 45

[122] Shane M. Eaton, Haibin Zhang, Mi Li Ng, Jianzhao Li, Wei-Jen Chen, Stephen Ho, and Peter R. Herman. Transition from thermal diffusion to heat accumulation in high repetition rate femtosecond laser writing of buried optical waveguides. *Optics Express*, 16(13):9443–9458, 2008. 33

[123] Douglas J. Little, Martin Ams, Peter Dekker, Graham D. Marshall, Judith M. Dawes, and Michael J. Withford. Femtosecond laser modification of fused silica: the effect of writing polarization on si-o ring structure. *Optics Express*, 16(24):20029–20037, 2008. 33

[124] M. Ams, G. D. Marshall, and M. J. Withford. Study of the influence of femtosecondlaser polarisation on direct writing of waveguides. *Optics Express*, 14(26):13158–13163, 2006. 34

[125] Lawrence Shah, Alan Arai, Shane Eaton, and Peter Herman. Waveguide writing in fused silica with a femtosecond fiber laser at 522 nm and 1 mhz repetition rate. *Optics Express*, 13(6):1999–2006, 2005. 34

[126] Yusuke Nasu, Masaki Kohtoku, and Yoshinori Hibino. Low-loss waveguides written with a femtosecond laser for flexible interconnection in a planar light-wave circuit. *Optics Letters*, 30(7):723–725, 2005. 35

[127] R. R. Thomson, S. Campbell, I. J. Blewett, A. K. Kar, and D. T. Reid. Optical waveguide fabrication in z-cut lithium niobate (linbo[sub 3]) using femtosecond

pulses in the low repetition rate regime. *Applied Physics Letters*, 88(11):111109, 2006. 35, 37

[128] Shane Eaton, Haibin Zhang, Peter Herman, Fumiyo Yoshino, Lawrence Shah, James Bovatsek, and Alan Arai. Heat accumulation effects in femtosecond laser-written waveguides with variable repetition rate. *Optics Express*, 13(12):4708–4716, 2005. 35

[129] Weijia Yang, Peter G. Kazansky, Yasuhiko Shimotsuma, Masaaki Sakakura, Kiyotaka Miura, and Kazuyuki Hirao. Ultrashort-pulse laser calligraphy. *Applied Physics Letters*, 93(17):171109, 2008. 35

[130] A. MarcinkeviÄĐius, V. Mizeikis, S. Juodkazis, S. Matsuo, and H. Misawa. Effect of refractive index-mismatch on laser microfabrication in silica glass. *Applied Physics A*, 76:257–260, 2003. 36

[131] Jonas Burghoff, Christian Grebing, Stefan Nolte, and Andreas Tünnermann. Efficient frequency doubling in femtosecond laser-written waveguides in lithium niobate. *Applied Physics Letters*, 89(8):081108, 2006. 37, 45

[132] DeniseM. Krol. Spectroscopic characterization of waveguides. In Roberto Osellame, Giulio Cerullo, and Roberta Ramponi, editors, *Femtosecond Laser Micromachining*, volume 123 of *Topics in Applied Physics*, pages 43–65. Springer Berlin Heidelberg, 2012. 38

[133] S. Juodkazis, M. Watanabe, H.-B. Sun, S. Matsuo, J. Nishii, and H. Misawa. Optically induced defects in vitreous silica. *Applied Surface Science*, 154:696 – 700, 2000. 38

[134] Airan Rodenas, Amir H Nejadmalayeri, Daniel Jaque, and Peter Herman. Confocal Raman imaging of optical waveguides in LiNbO3 fabricated by ultrafast high-repetition rate laser-writing. *Optics Express*, 16(18):13979–13989, 2008. 38

[135] A. RÃşdenas, G.A. Torchia, G. Lifante, E. Cantelar, J. Lamela, F. Jaque, L. Roso, and D. Jaque. Refractive index change mechanisms in femtosecond laser written ceramic nd:yag waveguides: micro-spectroscopy experiments and

beam propagation calculations. *Applied Physics B*, 95:85–96, 2009. 38, 45, 112, 117, 118, 119

[136] Roberto Osellame, Stefano Taccheo, Marco Marangoni, Roberta Ramponi, Paolo Laporta, Dario Polli, Sandro De Silvestri, and Giulio Cerullo. Femtosecond writing of active optical waveguides with astigmatically shaped beams. *Journal of the Optical Society of America B*, 20(7):1559–1567, 2003. 39, 40

[137] G Cerullo, R Osellame, S Taccheo, M Marangoni, D Polli, R Ramponi, P Laporta, and S De Silvestri. Femtosecond micromachining of symmetric waveguides at 1.5 Âţm by astigmatic beam focusing. *Optics Letters*, 27(21):1938, 2002. 39

[138] Ya Cheng, Koji Sugioka, Katsumi Midorikawa, Masashi Masuda, Koichi Toyoda, Masako Kawachi, and Kazuhiko Shihoyama. Control of the cross-sectional shape of a hollow microchannel embedded in photostructurable glass by use of a femtosecond laser. *Optics Letters*, 28(1):55–57, 2003. 40

[139] Martin Ams, G D Marshall, D J Spence, and M J Withford. Slit beam shaping method for femtosecond laser direct-write fabrication of symmetric waveguides in bulk glasses. *Opt Express*, 13(15):5676–5681, 2005. 40, 41

[140] R. R. Thomson, A S Bockelt, E Ramsay, S. Beecher, A H Greenaway, A.K. Kar, and D T Reid. Shaping ultrafast laser inscribed optical waveguides using a deformable mirror. *Optics Express*, 16(17):12786–12793, August 2008. 41

[141] A Ruiz de la Cruz, A Ferrer, W Gawelda, D Puerto, M Galván Sosa, J Siegel, and J Solis. Independent control of beam astigmatism and ellipticity using a SLM for fs-laser waveguide writing. *Optics Express*, 17(23):20853–20859, 2009. 41

[142] P S Salter, A Jesacher, J B Spring, B J Metcalf, N Thomas-Peter, R D Simmonds, N K Langford, I A Walmsley, and M J Booth. Adaptive slit beam shaping for direct laser written waveguides. *Optics Letters*, 37(4):470, 2012. 41, 42

[143] Yusuke Nasu, Masaki Kohtoku, and Yoshinori Hibino. Low-loss waveguides written with a femtosecond laser for flexible interconnection in a planar light-wave circuit. *Optics Letters*, 30(7):723, 2005. 43, 44

[144] Graeme Brown, Robert R Thomson, Ajoy K Kar, Nicholas D Psaila, and Henry T Bookey. Ultrafast laser inscription of Bragg-grating waveguides using the multi-scan technique. *Optics Letters*, 37(4):491, 2012. 44, 45

[145] K Miura, Jianrong Qiu, H Inouye, T Mitsuyu, and K Hirao. Photowritten optical waveguides in various glasses with ultrashort pulse laser. *Applied Physics Letters*, 71(23):3329, 1997. 44

[146] N.D. Psaila, R. R. Thomson, H T Bookey, N Chiodo, S Shen, R Osellame, G Cerullo, A Jha, and A.K. Kar. Er:Yb-Doped Oxyfluoride Silicate Glass Waveguide Laser Fabricated Using Ultrafast Laser Inscription. *IEEE Photonics Technology Letters*, 20(2):126–128, 2008. 44, 110

[147] G Della Valle, S Taccheo, R Osellame, A Festa, G Cerullo, and P Laporta. 1.5 Îijm single longitudinal mode waveguide laser fabricated by femtosecond laser writing. *Optics Express*, 15(6):3190–3194, 2007. 44

[148] S J Beecher, R. R. Thomson, N.D. Psaila, Z Sun, T Hasan, A G Rozhin, A C Ferrari, and A.K. Kar. 320 fs pulse generation from an ultrafast laser inscribed waveguide laser mode-locked by a nanotube saturable absorber. *Applied Physics Letters*, 97(11):111114, September 2010. 45, 110

[149] R Mary, S J Beecher, G. Brown, R. R. Thomson, D Jaque, S Ohara, and A.K. Kar. Compact, highly efficient ytterbium doped bismuthate glass waveguide laser. *Optics Letters*, 37(10):1691–1693, 2012. 45, 110

[150] John R Macdonald, Patrick A Berry, Kenneth L Schelper, and Ajoy Kar. Directly Written Mid-Infrared Waveguides in Zinc Selenide. In *Lasers, Sources, and Related Photonic Devices (2012), paper IF1A.3*. Optical Society of America, February 2012. 45

[151] J Siebenmorgen, T Calmano, K Petermann, and G Huber. Highly efficient Yb: YAG channel waveguide laser written with a femtosecond-laser. *Optics Express*, 18(15):16035–16041, July 2010. 45

[152] Ik-Bu Sohn, Man-Seop Lee, and Jeong-Yong Chung. Fabrication of optical splitter and passive alignment technique with a femtosecond laser. *Photonics Technology Letters, IEEE*, 17(11):2349–2351, 2005. 45

[153] Kaoru Minoshima, Andrew Kowalevicz, Erich Ippen, and James Fujimoto. Fabrication of coupled mode photonic devices in glass by nonlinear femtosecond laser materials processing. *Optics Express*, 10(15):645–652, 2002. 45

[154] Shane M Eaton, W Chen, L Zhang, H Zhang, R Iyer, J S Aitchison, and P R Herman. Telecom-band directional coupler written with femtosecond fiber laser. *Photonics Technology Letters, IEEE*, 18(20):2174–2176, 2006. 45

[155] Kenya Suzuki, Vikas Sharma, James G Fujimoto, Erich P Ippen, and Yusuke Nasu. Characterization of symmetric [3 x 3] directional couplers fabricated by direct writing with a femtosecond laser oscillator. *Optics Express*, 14(6):2335–2343, 2006. 45

[156] R. R. Thomson, R J Harris, T A Birks, G. Brown, J Allington-Smith, and J Bland-Hawthorn. Ultrafast laser inscription of a 121-waveguide fan-out for astrophotonics. *Optics Letters*, 37(12):2331–2333, 2012. 45

[157] R. R. Thomson, T A Birks, S G Leon-Saval, A.K. Kar, and J Bland-Hawthorn. Ultrafast laser inscription of an integrated photonic lantern. *Optics Express*, 19(6):5698–5705, 2011. 45

[158] Stephen J Beecher, Robert R Thomson, Bishnu P Pal, and Ajoy K Kar. Single Stage Ultrafast Laser Inscription of a Side-Polished Fiber-Like Waveguide Sensor. *IEEE Sensors Journal*, 12(5):1263–1266, 2012. 45

[159] Graham D Marshall, Alberto Politi, Jonathan C F Matthews, Peter Dekker, Martin Ams, Michael J Withford, and Jeremy L O'Brien. Laser written waveguide photonic quantum circuits. *Optics Express*, 17(15):12546, 2009. 45

[160] Jayashree A Dharmadhikari, Rodney Bernard, Anuj K Bhatnagar, Deepak Mathur, and Aditya K Dharmadhikari. Axicon-based writing of waveguides in BK7 glass. *Optics Letters*, 38(2):172, 2013. 45

[161] Y Bellouard, A Said, M Dugan, and P Bado. Fabrication of high-aspect ratio, micro-fluidic channels and tunnels using femtosecond laser pulses and chemical etching. *Optics Express*, 2004. 46, 47

[162] Rod Taylor, C Hnatovsky, E Simova, D Rayner, M Mehandale, V Bhardwaj, and P Corkum. Ultra-high resolution index of refraction profiles of femtosecond laser modified silica structures. *Optics Express*, 11(7):775–781, 2003. 47

[163] C Hnatovsky, R S Taylor, E Simova, V R Bhardwaj, D M Rayner, and P B Corkum. Polarization-selective etching in femtosecond laser-assisted microfluidic channel fabrication in fused silica. *Optics Letters*, 30(14):1867–1869, 2005. 48, 49

[164] Francesco Venturini, Walter Navarrini, Giuseppe Resnati, Pierangelo Metrangolo, Rebeca Martinez Vazquez, Roberto Osellame, and Giulio Cerullo. Selective Iterative Etching of Fused Silica with Gaseous Hydrofluoric Acid. *The Journal of Physical Chemistry C*, 114(43):18712–18716, November 2010. 49

[165] KC Vishnubhatla, N Bellini, R Ramponi, G Cerullo, and R Osellame. Shape control of microchannels fabricated in fused silica by femtosecond laser irradiation and chemical etching. *Optics Express*, 17(10):8685–8695, May 2009. 50

[166] Shigeki Matsuo, Haruki Sumi, Satoshi Kiyama, Takuro Tomita, and Shuichi Hashimoto. Femtosecond laser-assisted etching of Pyrex glass with aqueous solution of KOH. *Applied Surface Science*, 255(24):9758–9760, September 2009. 50

[167] Satoshi Kiyama, Shigeki Matsuo, Shuichi Hashimoto, and Yasushi Morihira. Examination of Etching Agent and Etching Mechanism on Femotosecond Laser Microfabrication of Channels Inside Vitreous Silica Substrates âĂă. *The Journal of Physical Chemistry C*, 113(27):11560–11566, July 2009. 50

[168] Moosung Kim, David J Hwang, Hojeong Jeon, Kuniaki Hiromatsu, and Costas P Grigoropoulos. Single cell detection using a glass-based optofluidic device fabricated by femtosecond laser pulses. *Lab on a Chip*, 9(2):311–318, 2009. 52, 53, 65

[169] F Bragheri, P Minzioni, R Martinez Vazquez, N Bellini, P Paiè, C Mondello, R Ramponi, I Cristiani, and R Osellame. Optofluidic integrated cell sorter fabricated by femtosecond lasers. *Lab on a Chip*, 12(19):3779, 2012. 54, 55

[170] Andrea Crespi, Yu Gu, Bongkot Ngamsom, Hugo J W M Hoekstra, Chaitanya Dongre, Markus Pollnau, Roberta Ramponi, Hans H van den Vlekkert, Paul Watts, Giulio Cerullo, and Roberto Osellame. Three-dimensional Mach-Zehnder interferometer in a microfluidic chip for spatially-resolved label-free detection. *Lab on a Chip*, 10(9):1167–1173, 2010. 54

[171] Steven J Altschuler and Lani F Wu. Cellular heterogeneity: Do differences make a difference? *Cell*, 141(4):559–563, 2010. 57

[172] Maureen A Walling and Jason R E Shepard. Cellular heterogeneity and live cell arrays. *Lab on a Chip*, 40(7):4049–4076, 2011. 57, 58

[173] Theresa B Taylor, Prashant R Nambiar, Rajiv Raja, Evelyn Cheung, Daniel W Rosenberg, and Birgit Anderegg. Microgenomics: Identification of new expression profiles via small and single-cell sample analyses. *Cytometry*, 59A(2):254–261, 2004. 57

[174] Mark Shackleton, Elsa Quintana, Eric R Fearon, and Sean J Morrison. Heterogeneity in cancer: Cancer stem cells versus clonal evolution. *Cell*, 138(5):822–829, September 2009. 57

[175] M Cristofanilli. Circulating tumor cells: A novel prognostic factor for newly diagnosed metastatic breast cancer. *Journal of Clinical Oncology*, 23(7):1420–1430, 2005. 57

[176] Bjorn T Adalsteinsson, Haukur Gudnason, Thor Aspelund, Tamara B Harris, Lenore J Launer, Gudny Eiriksdottir, Albert V Smith, and Vilmundur Gudnason. Heterogeneity in white blood cells has potential to confound dna methylation measurements. *PLoS ONE*, 7(10):e46705, 2012. 57

[177] Maurice A Canham, Alexei A Sharov, Minoru S H Ko, and Joshua M Brickman. Functional heterogeneity of embryonic stem cells revealed through translational

amplification of an early endodermal transcript. *PLOS Biology*, 8(5):e1000379, 2010. 57

[178] Jamil El-Ali, Peter K Sorger, and Klavs F Jensen. Cells on chips. *Nature*, 442(7101):403–411, 2006. 58

[179] Xuanhong Cheng, Daniel Irimia, Meredith Dixon, Kazuhiko Sekine, Utkan Demirci, Lee Zamir, Ronald G Tompkins, William Rodriguez, and Mehmet Toner. A microfluidic device for practical label-free cd4+ t cell counting of hiv-infected subjects. *Lab on a Chip*, 7(2):170–178, 2007. 58

[180] Peter Gascoyne, Chulabhorn Mahidol, Mathuros Ruchirawat, Jutamaad Satayavivad, Piyajit Watcharasit, and Frederick F Becker. Microsample preparation by dielectrophoresis: isolation of malaria. *Lab on a Chip*, 2(2):70–75, 2002. 58

[181] Joanna A Korecka, Joost Verhaagen, and Elly M Hol. Cell-replacement and gene-therapy strategies for parkinson's and alzheimer's disease. *Regenerative Medicine*, 2(4):425–446, 2007. 58

[182] M J Tomlinson, S Tomlinson, X B Yang, and J Kirkham. Cell separation: Terminology and practical considerations. *Journal of Tissue Engineering*, 4(0), 2013. 58

[183] Daniel R Gossett, Westbrook M Weaver, Albert J Mach, Soojung Claire Hur, Henry Tat Kwong Tse, Wonhee Lee, Hamed Amini, and Dino Di Carlo. Label-free cell separation and sorting in microfluidic systems. *Analytical and Bioanalytical Chemistry*, 397(8):3249–3267, 2010. 59, 60, 61, 62, 63

[184] Stefan Miltenyi, Werner Müller, Walter Weichel, and Andreas Radbruch. High gradient magnetic cell separation with macs. *Cytometry*, 11(2):231–238, 1990. 59

[185] Hong Miao Ji, Victor Samper, Yu Chen, Chew Kiat Heng, Tit Meng Lim, and Levent Yobas. Silicon-based microfilters for whole blood cell separation. *Biomedical microdevices*, 10(2):251–257, October 2007. 60

[186] H Mohamed, L D McCurdy, D H Szarowski, S Duva, J N Turner, and M Caggana. Development of a rare cell fractionation device: Application for cancer detection. *IEEE Sensors Journal*, 3(4):251–256, December 2004. 60

[187] Sarah Vankrunkelsven, David Clicq, Kris Pappaert, Willy Ranson, Cathleen De Tandt, Heidi Ottevaere, Hugo Thienpont, Gino V Baron, and Gert Desmet. A novel microstep device for the size separation of cells. *ELECTROPHORESIS*, 25(1011):1714–1722, June 2004. 60

[188] Yuushi Sai, Masumi Yamada, Masahiro Yasuda, and Minoru Seki. Continuous separation of particles using a microfluidic device equipped with flow rate control valves. *Journal of Chromatography A*, 1127(1-2):214–220, September 2006. 60

[189] L R Huang. Continuous particle separation through deterministic lateral displacement. *Science (New York, N.Y.)*, 304(5673):987–990, May 2004. 60

[190] Hideaki Tsutsui and Chih-Ming Ho. Cell separation by non-inertial force fields in microfluidic systems. *Mechanics Research Communications*, 36(1):92–103, January 2009. 60, 61

[191] Kishan Dholakia, Peter Reece, and Min Gu. Optical micromanipulation. *Chemical Society Reviews*, 37(1):42–55, 2007. 61

[192] Praveen C Ashok and Kishan Dholakia. Optical trapping for analytical biotechnology. *Current Opinion in Biotechnology*, 23(1):16–21, February 2012. 61

[193] L. Paterson, E Papagiakoumou, G Milne, V Garcés-Chávez, S A Tatarkova, W Sibbett, F J Gunn-Moore, P E Bryant, A C Riches, and K Dholakia. Light-induced cell separation in a tailored optical landscape. *Applied Physics Letters*, 87(12):123901, 2005. 61

[194] P C Ashok, R F Marchington, P Mthunzi, T F Krauss, and K Dholakia. Optical chromatography using a photonic crystal fiber with on-chip fluorescence excitation. *Optics Express*, 18(6):6396–6407, 2010. 61

[195] Julien Autebert, Benoit Coudert, François-Clément Bidard, Jean-Yves Pierga, Stéphanie Descroix, Laurent Malaquin, and Jean-Louis Viovy. Microfluidic: An innovative tool for efficient cell sorting. *Methods*, 57(3):297–307, 2012. 62

[196] S L Neale, M Mazilu, J I B Wilson, K Dholakia, and T F Krauss. The resolution of optical traps created by Light Induced Dielectrophoresis (LIDEP). *Optics Express*, 15(20):12619–12626, 2007. 62

[197] Tatyana G Kuznetsova, Maria N Starodubtseva, Nicolai I Yegorenkov, Sergey A Chizhik, and Renat I Zhdanov. Atomic force microscopy probing of cell elasticity. *Micron*, 38(8):824–833, 2007. 73

[198] Robert Kiss, Henry Bock, Steve Pells, Elisabetta Canetta, Ashok K Adya, Andrew J Moore, Paul De Sousa, and Nicholas A Willoughby. Elasticity of human embryonic stem cells as determined by atomic force microscopy. *Journal of Biomechanical Engineering*, 133(10):101009, 2011. 83

[199] Yi Fu, Lip Ket Chin, Tarik Bourouina, Ai Qin Liu, and Antonius M J VanDongen. Nuclear deformation during breast cancer cell transmigration. *Lab on a Chip*, 12(19):3774–3778, 2012. 85, 110, 125

[200] RI Morimoto. Cells in stress: transcriptional activation of heat shock genes. *Science (New York, N.Y.)*, 259:1409–1410, 1993. 87

[201] Tsung-Min Hsieh, Ching-Hsing Luo, Jung-Hao Wang, Jr-Lung Lin, Kang-Yi Lien, and Gwo-Bin Lee. A two-dimensional, self-compensated, microthermal cycler for one-step reverse transcription polymerase chain reaction applications. *Microfluidics and Nanofluidics*, 6(6):797–809, October 2008. 87

[202] Thomas M Pearce, J Adam Wilson, S George Oakes, Shing-Yan Chiu, and Justin C Williams. Integrated microelectrode array and microfluidics for temperature clamp of sensory neurons in culture. *Lab Chip*, 5(1):97–101, 2004. 87

[203] Roy M Daniel and Michael J Danson. A new understanding of how temperature affects the catalytic activity of enzymes. *Trends in Biochemical Sciences*, 35(10):584–591, October 2010. 87

[204] Terry B Huff, Ling Tong, Yan Zhao, Matthew N Hansen, Ji-Xin Cheng, and Alexander Wei. Hyperthermic effects of gold nanorods on tumor cells. *Nanomedicine*, 2(1):125–132, 2007. 87, 88

[205] Cornel Iancu and Lucian Mocan. Advances in cancer therapy through the use of carbon nanotube-mediated targeted hyperthermia. *International Journal of Nanomedicine*, 6:1675–1684, 2011. 88, 90

[206] Eric J Stewart. Growing unculturable bacteria. *Journal of Bacteriology*, 194(16):4151–4160, 2012. 88

[207] T Z Esikova, Yu V Temirov, S L Sokolov, and Yu B Alakhov. Secondary antimicrobial metabolites produced by thermophilic bacillus spp. strains vk2 and vk21. *Microfluidics and Nanofluidics*, 38(3):226–231, 2002. 88

[208] Yasuaki Masumoto and Koji Sonobe. Size-dependent energy levels of cdte quantum dots. *Physical Review B*, 56(15):9734–9737, 1997. 89

[209] Laura Martinez Maestro, Carlos Jacinto, Uéslen Rocha, M Carmen Iglesias-de la Cruz, Francisco Sanz-Rodríguez, Angeles Juarranz, José García Solé, and Daniel Jaque. Optimum quantum dot size for highly efficient fluorescence bioimaging. *Journal of Applied Physics*, 111(2):023513, 2012. 89, 93

[210] Chris Xu, Warren Zipfel, Jason B Shear, Rebecca M Williams, and Watt W Webb. Multiphoton fluorescence excitation: new spectral windows for biological nonlinear microscopy. *Proceedings of the National Academy of Sciences of the United States of America*, 93(20):10763–10768, 1996. 89

[211] X Michalet. Quantum Dots for Live Cells, in Vivo Imaging, and Diagnostics. *Science (New York, N.Y.)*, 307(5709):538–544, 2005. 89, 105

[212] LM Maestro, C Jacinto, UR Silva, F Vetrone, JM Capobianco, D Jaque, and J Garcia Sole. Cdte quantum dots as nanothermometers: Towards highly sensitive thermal imaging. *Small*, 7(13):1774–1778, 2011. 89

[213] Ute Resch-Genger, Markus Grabolle, Sara Cavaliere-Jaricot, Roland Nitschke, and Thomas Nann. Quantum dots versus organic dyes as fluorescent labels. *Nature Methods*, 5(9):763–775, 2008. 89, 105

[214] Timothy Jamieson, Raheleh Bakhshi, Daniela Petrova, Rachael Pocock, Mo Imani, and Alexander M Seifalian. Biological applications of quantum dots. *Biomaterials*, 28(31):4717–4732, 2007. 90

[215] Jeffrey L Bahr and James M Tour. Covalent chemistry of single-wall carbon nanotubes. *Journal of Materials Chemistry*, 12(7):1952–1958, 2002. 90

[216] Feifan Zhou, Da Xing, Zhongmin Ou, Baoyan Wu, Daniel E Resasco, and Wei R Chen. Cancer photothermal therapy in the near-infrared region by using single-walled carbon nanotubes. *Journal of Biomedical Optics*, 14(2):021009, 2009. 90

[217] K Kostarelos, A Bianco, and M Prato. Promises, facts and challenges for carbon nanotubes in imaging and therapeutics. *Nature Nanotechnology*, 4(10):627–633, 2009. 90

[218] Hongbao Xin, Xingmin Li, and Baojun Li. Massive photothermal trapping and migration of particles by a tapered optical fiber. *Optics Express*, 19(18):17065–17074, 2011. 90

[219] H Mao, JR Arias-Gonzalez, SB Smith, Ignatio Tinococ Jr, and C Bustamante. Temperature control methods in a laser tweezers system. *Biophysical Journal*, 89:1308–1316, 2005. 91, 96, 98

[220] Richard W Cole, Tushare Jinadasa, and Claire M Brown. Measuring and interpreting point spread functions to determine confocal microscope resolution and ensure quality control. *Nature Protocols*, 6(12):1929–1941, 2011. 94

[221] E Peterman, F Gittes, and C Schmidt. Laser-induced heating in optical traps. *Biophysical Journal*, 84(2):1308–1316, 2003. 96

[222] Jon R Whitney, Saugata Sarkar, Jianfei Zhang, Thao Do, Taylor Young, Mary Kyle Manson, Thomas A Campbell, Alex A Puretzky, Christopher M Rouleau, Karen L More, David B Geohegan, Christopher G Rylander, Harry C Dorn, and Marissa Nichole Rylander. Single walled carbon nanohorns as photothermal cancer agents. *Lasers in Surgery and Medicine*, 43(1):43–51, 2011. 100

[223] Prashant K Jain, Kyeong Seok Lee, Ivan H El-Sayed, and Mostafa A El-Sayed. Calculated absorption and scattering properties of gold nanoparticles of different size, shape, and composition: applications in biological imaging and biomedicine. *The Journal of Physical Chemistry B*, 110(14):7238–7248, 2011. 102

[224] Po-Cheng Chen, Ya-Na Chen, Pin-Che Hsu, Chung-Chien Shih, and Huan-Tsung Chang. Photoluminescent organosilane-functionalized carbon dots as temperature probes. *Chemical Communications*, 49(16):1639, 2013. 105

[225] Q Kou, I Yesilyurt, and Y Chen. Collinear dual-color laser emission from a microfluidic dye laser. *Applied Physics Letters*, 88(9):091101–091101–3, 2006. 107, 108

[226] M Gersborg-Hansen, S Balslev, N A Mortensen, and A Kristensen. A coupled cavity micro-fluidic dye ring laser. *Microelectronic Engineering*, 78-79:185–189, 2005. 107

[227] Xin Tu, Xiang Wu, Ming Li, Liying Liu, and Lei Xu. Ultraviolet single-frequency coupled optofluidic ring resonator dye laser. *Optics Express*, 20(18):19996–20001, 2012. 107

[228] Ya Cheng, Koji Sugioka, and Katsumi Midorikawa. Microfluidic laser embedded in glass by three-dimensional femtosecond laser microprocessing. *Optics Letters*, 29(17):2007–2009, 2004. 108

[229] Giuseppe Della Valle and Roberto Osellame. Active photonic devices. In *Femtosecond Laser Micromachining*, pages 265–292. Springer Berlin Heidelberg, Berlin, Heidelberg, 2011. 109, 111

[230] Rudiger Paschotta. *Encyclopedia of Laser Physics and Technology*, volume XII. Wiley-VCH, Berlin, october 2008 edition, 2008. 109

[231] Y Sikorski, A A Said, P Bado, R Maynard, C Florea, and K A Winick. Optical waveguide amplifier in nd-doped glass written with near-ir femtosecond laser pulses. *Electronics Letters*, 36(3):226–227, 2000. 109

[232] G Della Valle, R Osellame, N Chiodo, S Taccheo, G Cerullo, P Laporta, A Killi, U Morgner, M Lederer, and D Kopf. C-band waveguide amplifier produced by femtosecond laser writing. *Optics Express*, 13(16):5976–5982, 2005. 110

[233] N.D. Psaila, R. R. Thomson, H T Bookey, A.K. Kar, N Chiodo, R Osellame, G Cerullo, A Jha, and S Shen. Er:yb-doped oxyfluoride silicate glass waveguide

amplifier fabricated using femtosecond laser inscription. *Applied Physics Letters*, 90(13):131102–131102, 2007. 110

[234] S Taccheo, G Della Valle, R Osellame, G Cerullo, N Chiodo, P Laporta, O Svelto, Alexander Killi, Uwe Morgner, and Max Lederer. Er: Yb-doped waveguide laser fabricated by femtosecond laser pulses. *Optics Letters*, 29(22):2626–2628, 2004. 110

[235] G A Torchia, A Ródenas, A Benayas, E Cantelar, L Roso, and D Jaque. Highly efficient laser action in femtosecond-written nd:yttrium aluminum garnet ceramic waveguides. *Applied Physics Letters*, 92(11):111103–111103–3, 2008.

[236] Martin Ams, Peter Dekker, Graham D Marshall, and Michael J Withford. Monolithic 100 mw yb waveguide laser fabricated using the femtosecond-laser direct-write technique. *Optics Letters*, 34(3):247–249, 2009. 110

[237] Orazio Svelto. *Principles of Lasers*. Springer Science, New York, 5 edition, 2010. 111

[238] A G Okhrimchuk, A V Shestakov, I Khrushchev, and J Mitchell. Depressed cladding, buried waveguide laser formed in a yag:nd3+ crystal by femtosecond laser writing. *Optics Letters*, 30(17):2248, 2005. 111

[239] J Siebenmorgen, K Petermann, G Huber, K Rademaker, S Nolte, and A Tünnermann. Femtosecond laser written stress-induced nd:y3al5o12 (nd:yag) channel waveguide laser. *Applied Physics B: ...*, 97(2):251–255, 2009. 111

[240] Shigeki Matsuo, Y Tabuchi, Tatsuya Okada, Saulius Juodkazis, and Hiroaki Misawa. Femtosecond laser assisted etching of quartz: microstructuring from inside. *Applied Physics A: Materials Science & Processing*, 84(1):99–102, 2006. 112

[241] S Juodkazis, K Nishimura, H Misawa, T Ebisui, R Waki, S Matsuo, and T Okada. Control over the crystalline state of sapphire. *Advanced Materials*, 18(11):1361–1364, 2006. 112

[242] Airan Rodenas, Guangyong Zhou, Daniel Jaque, and Min Gu. Rare-earth spontaneous emission control in three-dimensional lithium niobate photonic crystals. *Advanced Materials*, 21(34):3526–3530, September 2009. 112

[243] A Ródenas, A Benayas, J R Macdonald, J Zhang, D Y Tang, D Jaque, and A.K. Kar. Direct laser writing of near-IR step-index buried channel waveguides in rare earth doped YAG. *Optics Letters*, 36(17):3395, 2011. 113, 127

[244] Airan Rodenas, Guangyong Zhou, Daniel Jaque, and Min Gu. Direct laser writing of three-dimensional photonic structures in nd: yttrium aluminum garnet laser ceramics. *Applied Physics Letters*, 93(15):151104–151104–3, 2008. 113

[245] A A Kaminskii. Laser crystals and ceramics: recent advances. *Laser & Photonics Review*, 1(2):93–177, 2007. 117

[246] S Kobyakov, A Kamińska, A Suchocki, D Galanciak, and M Malinowski. Nd[sup 3+]-doped yttrium aluminum garnet crystal as a near-infrared pressure sensor for diamond anvil cells. *Applied Physics Letters*, 88(23):234102–234102–2, 2006. 118

[247] K Chotivanich P Charunwatthana F Omodeo-Salè D Taramelli N P Day N J White A M Dondorp F Nuchsongsin. Effects of malaria heme products on red blood cell deformability. *American journal of tropical medicine and hygiene*, 77(4):617–622, 2007. 125

[248] Jing Chen, Zhong-Dong Shi, Xinying Ji, Jorge Morales, Jingwei Zhang, Navneet Kaur, and Sihong Wang. Enhanced Osteogenesis of Human Mesenchymal Stem Cells by Periodic Heat Shock in Self-Assembling Peptide Hydrogel. *Tissue Engineering Part A*, 19(5-6):716–728, 2013. 127

[249] Rune Norgaard, Moustapha Kassem, and Suren I S Rattan. Heat Shock-Induced Enhancement of Osteoblastic Differentiation of hTERT-Immortalized Mesenchymal Stem Cells. *Annals of the New York Academy of Sciences*, 1067(1):443–447, May 2006. 127

[250] Huan Huang, Lih-Mei Yang, and Jian Liu. Ultrashort pulsed fiber laser welding and sealing of transparent materials. *Applied Optics*, 51(15):2979, 2012. 128

[251] Shunbo Li, Ming Li, Yu Sanna Hui, Wenbin Cao, Weihua Li, and Weijia Wen. A novel method to construct 3D electrodes at the sidewall of microfluidic channel. *Microfluidics and Nanofluidics*, 14(3-4):499–508, 2012. 129

[252] James C Weaver and Yu A Chizmadzhev. Theory of electroporation: A review. *Bioelectrochemistry and Bioenergetics*, 41(2):135–160, 1996. 129

[253] Saeid Movahed and Dongqing Li. Microfluidics cell electroporation. *Microfluidics and Nanofluidics*, 10(4):703–734, 2010. 129

[254] Constantino Grosse and Herman P Schwan. Cellular membrane potentials induced by alternating fields. *Biophysical Journal*, 63(6):1632–1642, 1992. 129

[255] Sadhana Talele, Paul Gaynor, Michael J Cree, and Jethro van Ekeran. Modelling single cell electroporation with bipolar pulse parameters and dynamic pore radii. *Journal of Electrostatics*, 68(3):261–274, 2010. 129

[256] Shengnian Wang and L James Lee. Micro-/nanofluidics based cell electroporation. *Biomicrofluidics*, 7(1):011301–011301–14, 2013. 130

[257] Robert F Marchington, Yoshihiko Arita, Xanthi Tsampoula, Frank J Gunn-Moore, and Kishan Dholakia. Optical injection of mammalian cells using a microfluidic platform. *Biomedical Optics Express*, 1(2):527–536, 2010. 132

[258] Yeu-Chun Kim, Jung-Hwan Park, and Mark R Prausnitz. Microneedles for drug and vaccine delivery. *Advanced Drug Delivery Reviews*, 64(14):1547–1568, 2012. 133

[259] William T Ramsay, Muriel Bechu, Vladimir A Bolanos Quinones, Yongfeng Mei, Oliver G Schmidt, and Lynn Paterson. Triple beam optical trap for microsyringe construction. In *SPIE NanoScience + Engineering*, pages 809708–809708–9. SPIE, 2012. 133